

**COUPLED MOVEMENT OF LIQUID WATER, WATER  
VAPOR, AND HEAT IN DEEP VADOSE ZONES**

**Dissertation  
zur Erlangung des  
Doktorgrades der Naturwissenschaften (Dr. rer. nat.)**

der

Naturwissenschaftlichen Fakultät III  
Agrar- und Ernährungswissenschaften,  
Geowissenschaften und Informatik

der Martin-Luther-Universität Halle-Wittenberg

vorgelegt von  
Frau «**Madi, Raneem**»  
Geb. am «09.11.1985» in «Latakia/Syrien»

**Datum der Verteidigung: 21.08.2018**

**Gutachter:**

**Prof. Dr. Ralf Merz: (Martin Luther University Halle-Wittenberg Department für Geowissenschaften und Leiter des (Catchment Hydrology) Departments im Helmholtz Zentrum für Umweltforschung, UFZ- Halle).**

**Prof. Dr. Christoph Hinz: (Brandenburgische technische Universität Cottbus-Senftenberg Lehrstuhl Hydrologie und Wasserressourcenbewirtschaftung).**

# SUMMARY

Arid and semi-arid regions are expanding noticeably and currently represent about 30% of the global terrestrial surface area. The effects of water scarcity in semi-arid and arid regions on human lives are felt with increasing severity by local populations. Groundwater recharge is very important in these regions as groundwater is often the only source to meet the increasing urban, industrial, and agricultural water requirements, therefore continuous efforts are exerted to improve quantifying the replenishment of aquifers in arid and semi-arid regions. The accurate quantification of the unsaturated zone water fluxes is essential to the estimation of groundwater recharge. This thesis aims to improve our ability to model these fluxes, and in order to do so, addresses the following issues: (i) Testing the physical-mathematical properties of many of the available parameterizations of the soil water retention curve and improving them where necessary to find parameterizations capable of covering the full water content range, including the dry end; (ii) Testing experimentally those soil hydraulic parameterizations that were found to be physically sound in the physical-mathematical tests on their ability to model the interplay between liquid water flow and water vapor flow in a simple porous medium under dry conditions; (iii) Carrying out a simulation study of coupled liquid water, water vapor, and heat flows in a 100 m bare soil profile under arid/hyper-arid conditions to clarify the role of wet and dry years on the dynamics of ground water recharge, the potential role of water vapor flow and the way the atmospheric input signal travels downward through the vadose zone for two soil hydraulic parameterizations suitable for dry conditions.

The major findings of this thesis are: (i) The choice of parameterization has a very large effect on simulated groundwater recharge; (ii) A reduction in the mean annual rainfall resulted in a much stronger reduction of the groundwater recharge; (iii) The effect of including vapor flow and/or the effect of the geothermal gradient was noticeable but inconsequential in comparison to the choice of parameterization; (iv) The deep unsaturated zone strongly damped and delayed the atmospheric signal. This study points to the importance of carefully considering the soil hydraulic parameterization to be used for long-term water balance studies that aim to determine or predict the variation of seasonal water availability to plants or long-term groundwater recharge to assess the sustainability of extractions from an underlying aquifer. Currently, this approach can only be carried out for 1-dimensional soil columns. Further studies would be required to develop a methodology to aggregate a set of one-dimensional studies to estimate the groundwater recharge of extensive aquifers, which often support indigenous populations, and to extend this work to sparse (and possibly grazed) vegetation, which then can be coupled to the deep-soil simulations carried out here to create more realistic simulation scenarios, in order to improve the accuracy of the groundwater recharge estimates.

# ZUSAMMENFASSUNG

Aride und semi-aride Gebiete breiten sich zunehmend aus und repräsentieren aktuell ca. 30% der terrestrischen Erdoberfläche. Die Auswirkungen der Wasserknappheit in semi-ariden und ariden Gebieten auf die lokale Bevölkerung werden mit steigender Schärfe wahrgenommen. Grundwasserneubildung ist in diesen Regionen von hoher Bedeutung, da Grundwasser meist die einzige Frischwasserquelle für den steigenden urbanen, industriellen und landwirtschaftlichen Wasserbedarf darstellt. Aus diesem Grund werden kontinuierlich Anstrengungen unternommen, um die Grundwasserneubildung in ariden und semi-ariden Gebieten zu quantifizieren. Eine präzise Quantifizierung der Wasserflüsse in der ungesättigten Zone ist für eine Abschätzung der Grundwasserneubildung essentiell. Das Ziel dieser Arbeit ist die Verbesserung unserer Fähigkeiten zur Modellierung dieser Flüsse und wird dabei folgende Aspekte thematisieren: (i) die Prüfung physikalisch-mathematischer Eigenschaften der verfügbaren Parametrisierungen der Boden-Wasser-Retentionskurve und diese bei Notwendigkeit so zu verbessern, dass der gesamte Bereich von Wassergehalten abgedeckt wird, inklusive des trockenen Endes der Kurve; (ii) experimentelle Überprüfung der bodenhydraulischen Parametrisierungen, die durch die physikalisch-mathematischen Tests als physikalisch fundiert eingestuft wurden, auf ihre Fähigkeit die Wechselwirkungen zwischen Wasserfluss und Wasserdampftransport in einem einfachen porösem Medium unter trockenen Bedingungen zu modellieren; (iii) die Durchführung einer Simulationsstudie über den gekoppelten Fluss von Wasser, Wasserdampf und Wärme in einem 100 m tiefen Bodenprofil unter ariden und hyper-ariden Bedingungen. Hierbei sollen die potentielle Bedeutung von Wasserdampftransport, der Einfluss von feuchten und trockenen Jahren auf die Dynamiken der Grundwasserneubildung und der Verlauf des atmosphärischen Eingabesignals durch die ungesättigte Zone für zwei hydraulische Parametrisierungen bestimmt werden.

Die wesentlichen Ergebnisse dieser Arbeit sind: (i) die Wahl der Parametrisierung hat einen sehr großen Einfluss auf die simulierte Grundwasserneubildung; (ii) ein Rückgang der mittleren jährlichen Niederschlagsmenge resultiert in einem wesentlich stärkeren Rückgang der Grundwasserneubildung; (iii) ein Effekt durch die Berücksichtigung des Wasserdampftransportes und/oder des thermalen Gradienten ist erkennbar, aber im Vergleich zur Auswahl der Parametrisierung unerheblich; (iv) das atmosphärische Signal wird durch die ungesättigte Zone stark abgeschwächt und verzögert. Diese Arbeit zeigt, dass eine sorgfältige Prüfung der bodenhydraulischen Parametrisierung für Langzeitwasserbilanzstudien von größter Bedeutung ist. Dies gilt unter anderem für Studien die Schwankungen der saisonalen Wasserverfügbarkeit für Pflanzen prognostizieren oder zur Modellierung langzeitiger Grundwasserneubildung für eine nachhaltige Wasserförderung aus dem unterliegenden Grundwasserleiter. Aktuell kann dieser Ansatz nur auf 1-dimensionalen Bodensäulen angewandt werden. Weitere Studien wären notwendig, um eine Methode zur Zusammenführung mehrerer 1-dimensionaler Studien zu entwickeln, die es ermöglicht die Grundwasserneubildung in extensiven Grundwasserleitern abzuschätzen und um den Einfluss spärlicher und möglicherweise beweideter Vegetation zu erweitern. Dies könnte mit dem hier durchgeführten Tiefenbodensimulationen gekoppelt werden, um so realistischere Simulationsszenarien zu schaffen und die Genauigkeit der ermittelten Grundwasserneubildung zu verbessern.

## **ACKNOWLEDGEMENTS**

Thanks to the Helmholtz Center for Environmental Research - UFZ for the financial support and offering the best research infrastructure and the excellent courses through its HIGRADE School. Hundreds of thanks are due to my supervisor Dr. Gerrit de Rooij of the Soil System Science department at UFZ-Halle. The door to his office was always open whenever I ran into a trouble spot or had a question about my research or writing, he always steered me in the right direction whenever he thought I needed it.

I would like to express my deepest gratitude to Prof. Ralf Merz of the Catchment Hydrology department at UFZ-Halle for his support and understanding. I also thank all colleagues at the Soil System Science department of UFZ-Halle for their constructive feedback and discussions and special thanks to the head of the department, Prof. Hans-Jörg Vogel, for his continuous support and to Dr. John Maximilian Köhne for his technical support and insightful remarks.

Many thanks to my friends in Syria and Germany who believed in me and were always sure that I will reach my goal at the end. Finally, I must express my very profound gratitude to my family in Syria and to my husband for providing me with unfailing support and continuous encouragement throughout my years of study and through the process of researching and writing this thesis. This accomplishment would not have been possible without them. Thank you.

Raneem Madi

## Terminology

AS	Unsaturated soil hydraulic conductivity model according to Alexander and Skaggs (1986)
B	Unsaturated soil hydraulic conductivity model according to Burdine (1953)
BCO	Soil water retention model according to Brooks and Corey (1964)
EE060	Relative humidity sensor
EC-5	Soil water sensor
FAO	Food and Agriculture Organization
FSB	Soil water retention model according to Fayer and Simmons (1995)
HYPROP <sup>®</sup>	Apparatus to measure soil water retention and hydraulic conductivity data
M	Unsaturated soil hydraulic conductivity model according to Mualem (1976)
NOAA	National Oceanic and Atmospheric Administration
PT-100	Platinum Resistance Sensor (Temperature Sensor)
RIA	Soil water retention model developed in this thesis
RMSE	Root Mean Square Error
RNA	Soil water retention model according to Rossi and Nimmo (1994)
SCE	Shuffled Complex Evolution
TBLG	Truncated modified Bartlett-Lewis rainfall model with Gamma-distribution
UNDP	United Nations Development Program
VGA	Modified soil water retention model of van Genuchten (1980) according to Ippisch (2006)
VGN	Soil water retention model according to van Genuchten (1980)
WSI	Water-Stress Indicator
WWAP	World Water Assessment Programme

# List of Contents

ACKNOWLEDGEMENTS .....	iii
Terminology .....	iv
List of Figures.....	vii
List of Tables .....	xi
1. General Introduction .....	1
1.1. Background and Motivation.....	1
1.2. Objectives and hypothesis of the thesis .....	4
2. Parametric soil water retention models: a critical evaluation of expressions for the full moisture range .....	5
Abstract:.....	5
2.1. Introduction.....	5
2.2. Theory .....	8
2.2.1. Hydraulic conductivity models and their behavior near saturation .....	8
2.2.2. Critical evaluation of parametric functions of the soil water retention curve .....	10
2.3. Materials and methods .....	28
2.3.1. Soil water retention and hydraulic conductivity data .....	28
2.3.2. Parameter fitting.....	29
2.3.2.1. Selected parameterizations .....	29
2.3.2.2. The objective function and its weighting factors .....	29
2.3.2.3. Parameter optimization by Shuffled Complex Evolution .....	31
2.3.3. Scenario study by numerical simulations .....	32
2.4. Results and discussion.....	33
2.4.1. Fitted parameters and quality of the fits.....	33
2.4.2. Simulation results.....	36
2.4.2.1. Silt .....	36
2.4.2.2. Sand .....	40
2.4.2.3. Silt loam and clay .....	46
2.4.3. General ramifications .....	49
3. Liquid water and vapor flow in dry sand: column experiments and numerical tests of different retention curve parameterizations.....	51
Abstract:.....	51
3.1. Introduction.....	51
3.2. Materials and Methods .....	53
3.2.1. Experimental set-up.....	53
3.3. Numerical modeling .....	55
3.3.1. Governing equations and their numerical implementation .....	55
3.3.2. Selected Parameterizations .....	56

3.4.	<i>Results and Discussion</i> .....	57
3.4.1.	Experimental results .....	57
3.4.2.	Fitted parameters .....	61
3.4.3.	Simulation results .....	62
3.4.3.1.	Liquid water and vapor fluxes.....	62
3.4.3.2.	Simulated and calculated pF values .....	64
3.4.3.3.	Simulated and measured salt profiles.....	66
3.5.	<i>Summary and Conclusions</i> .....	67
4.	Water, heat, and vapor flow in a deep vadose zone under arid and hyper-arid conditions: a numerical study...68	
	<i>Abstract</i> :.....	68
4.1.	<i>Introduction</i> .....	68
4.2.	<i>Materials and Methods</i> .....	70
4.2.1.	Rainfall data .....	70
4.2.2.	Temperature data.....	71
4.2.3.	Numerical modelling.....	72
4.2.3.1.	Initial and boundary conditions of the numerical model.....	72
4.2.4.	Soil water retention and hydraulic conductivity curves.....	73
4.2.5.	The relationship between rainfall and recharge .....	73
4.3.	<i>Results and Discussion</i> .....	74
4.3.1.	Fitted parameters .....	74
4.3.2.	Simulation results .....	75
4.3.2.1.	Wetter scenario (1) .....	75
4.3.2.1.1.	Signal propagation in the unsaturated zone .....	75
4.3.2.1.2.	The effect of vapor flow.....	81
4.3.2.1.3.	Vertical profiles of temperature, pressure head, water content, and liquid and vapor flux densities.....	83
4.3.2.2.	Drier scenario (2).....	83
4.3.2.2.1.	Signal propagation in the unsaturated zone .....	83
4.3.2.2.2.	The effect of vapor flow .....	85
4.3.2.2.3.	Vertical profiles of temperature, pressure head, water content, and liquid and vapor flux densities.....	86
4.4.	<i>Summary and Conclusions</i> .....	88
5.	Final conclusions and outlook.....	89
	Bibliography .....	91
	Appendix A. The variables used in Chapter 2 .....	101
	Appendix B. Simulations of coupled water and vapor flow in sand columns: fitted parameters and selected flux density profiles in Chapter 3.....	103
	Appendix C. Profiles at selected times of various variables generated during long-term simulations Chapter 4.....	112
	Curriculum Vitae .....	116
	Eidesstattliche Erklärung / Declaration under Oath.....	119



# List of Figures

**Figure 1.1:** Water stress in major basins around the world. Sources: P. Rekacewicz, 2006  
<http://www.grida.no/resources/5586> (accessed on June 15, 2017), WWAP (2012), p. 125. ....1

**Figure 1.2:** Available freshwater per capita per year by country. Source: P. Rekacewicz, 2006,  
<http://www.grida.no/resources/5596> (accessed June 15, 2017), based on data from Aquastat (FAO, 2016) .....2

**Figure 2.1:** The record of daily rainfall sums from Riyadh city that was used in the numerical scenario study. Three rainfall clusters are visible. The largest daily rainfall amount (5.4 cm) fell on day 656. The observation period starts at June 4, 1993, and ends at February 27, 1996.....33

**Figure 2.2:** Observed and fitted retention curves for the different soil textures. ....35

**Figure 2.3:** The observed and fitted hydraulic conductivity curve according to Burdine (1953), Mualem (1976) and Alexander and Skaggs (1986) using the fitted parameters of the Fayer and Simmons soil water retention curve (1995) for (a) sand, (b) silt, and (c) silt loam. ....36

**Figure 2.4:** The cumulative bottom fluxes leaving a silt soil column for the different combinations of soil water retention curve and hydraulic conductivity parameterizations. Panels a through e present the results for the indicated retention parameterizations (see Table 2.1). Panels f and g organize the results according to the conductivity function: either Mualem (1976) (f) or Alexander and Skaggs (1986) (g). ....38

**Figure 2.5:** Cumulative evaporation from a silt soil column for the different combinations of soil water retention and hydraulic conductivity parameterizations. Panels a through e present the results for the indicated retention parameterizations (see Table 2.1). Panels f and g organize the results according to the conductivity function: either Mualem (1976) (f) or Burdine (1953) (g). ....39

**Figure 2.6:** Cumulative infiltration in a silt profile for the VGA parameterization (see Table 2.1) with conductivity functions according to Mualem (1976) and Alexander and Skaggs (1986) (a) and four different parameterizations for the retention curve (see Table 2.1) with the Alexander and Skaggs conductivity function (b).....40

**Figure 2.7:** As Fig. 2.4, but for a sandy soil column. Unlike Fig. 2.4, the results of Burdine’s (1953) conductivity curve are shown (panel f).....42

**Figure 2.8:** Cumulative evaporation from a sandy profile for the different combinations of retention curve parameterizations (see Table 2.1) and hydraulic conductivity functions: Burdine (1953) (a), Mualem (1976) (b) or Alexander and Skaggs (1986) (c). ....43

**Figure 2.9:** Pressure head  $h_{Bot}$  and flux density  $v_{Bot}$  at the bottom of the sand column for the FSB parameterization (see Table 2.1) and the conductivity functions of Mualem (1976) (a), Burdine (1953) (b) and Alexander and Skaggs (1986) (c).....44

**Figure 2.10:** As Figure 2.9, but for the RNA parameterization (see Table 2.1).....45

**Figure 2.11:** As Figure 2.9, but for the BCO parameterization (see Table 2.1).....46

<b>Figure 2.12:</b> Cumulative bottom fluxes from a silt loam profile for all combinations of parameterizations (see Table 2.1) and Mualem’s (1976) (a) and Alexander and Skaggs’ (1986) conductivity functions (b), and for the RNA parameterization with all three conductivity functions (c).....	47
<b>Figure 2.13:</b> Cumulative evaporation from a silt loam profile for all parameterizations (see Table 2.1) with Mualem’s (1976) conductivity function (a) and the VGA parameterization with conductivity functions according to Mualem (1976) and Alexander and Skaggs (1986) (b). .....	47
<b>Figure 2.14:</b> Cumulative infiltration from a silt loam profile for four parameterizations (see Table 2.1) with the Alexander and Skaggs (1986) conductivity function (a) and for the VGA parameterizations with conductivity functions according to Mualem (1976) and Alexander and Skaggs (1986) (b). .....	48
<b>Figure 2.15:</b> As Fig. 2.12, for clay.....	48
<b>Figure 2.16:</b> As Fig. 2.13, for clay.....	49
<b>Figure 2.17:</b> As Fig. 2.14, for clay.....	49
<b>Figure 3.1:</b> Schematic drawing of the top and front view of an experimental column with the location of the slots (denoted by numbers) for the sensors. The relative humidity sensors are denoted EE060, the water content sensors EC-5, and the temperature sensor PT-100. The top view shows how deep the sensors penetrated the soil. The water content probes were installed with the two leads vertically aligned.....	54
<b>Figure 3.2:</b> The measured water retention curve of the sand used in the experiment. The fitted water retention curves according to Brooks and Corey (1964), van Genuchten (1980), Rossi and Nimmo (1994) (junction model without parabolic correction at the wet range), Fayer and Simmons (1995), and Ippisch et al. (2006) are shown as well.....	54
<b>Figure 3.3:</b> The different column packing steps: (a) packing the first saturated sand layer, (b) inserting the first sensor, (c) packing the added sand layers, (d) sealing the installation ports, (e) covering the column’s upper surface with plastic until the start of the experiment. ....	55
<b>Figure 3.4:</b> Measured evaporative fluxes for the columns containing salt with initial volumetric water contents in the top 23.5 cm of: 0.00 (a, b), 0.02 (c, d), 0.05 (e, f), and 0.08 (g, h). The left column presents the data for the soils without salt added to the water in the bottom 1 cm, the right column for the soils with added salt. ....	59
<b>Figure 3.5:</b> The measured amount of NaCl in mg per volume of sand layer in cm <sup>3</sup> after the completion of the experiment. ....	60
<b>Figure 3.6:</b> The measured amount of NaCl in mg per volume of sand layer in cm <sup>3</sup> for the columns with the indicated initial water contents without added salt to the water in the bottom 1 cm. All salt originates from the tap water added to the sand and the sand itself. ....	61
<b>Figure 3.7:</b> Observed and simulated evaporation for columns with initial water contents in the top 23.5 cm of 0.00 (a), 0.02 (b), 0.05 (c), and 0.08 (d). The observations are from the columns with a 10 mmol l <sup>-1</sup> NaCl solution initially saturating the bottom 1 cm of the column. ....	62
<b>Figure 3.8:</b> Simulated and calculated pF values for the FSB parameterization at three depths for columns with an initial water content of 0.00 (a), 0.02 (b), 0.05 (c), and 0.08 (d). The vertical drop-off in the observed pF values (labeled cal...) reflect a relative humidity of 1 observed at the times preceding the drop-off. When converted to pF this results in a value of -∞, causing a steep rise towards the first observation of a relative humidity < 1. The labels’s’ and ‘ns’ refer to columns with and without added salt in the bottom 1 cm. ....	65

<b>Figure 3.9:</b> As Figure 3.8 but for the RNA parameterization. ....	66
<b>Figure 3.10:</b> The distribution of NaCl in the various columns at the end of the experiment as to the observed (a) and according to the model runs using FSB (b) and RNA (c). ....	67
<b>Figure 4.1:</b> Daily rainfall data for a 3-year sample from the 120-year record. Panels (a) and (b) show the wetter scenario (1) and the drier scenario (2), respectively. ....	70
<b>Figure 4.2:</b> Retention data and fitted parameterization according to Fayer and Simmons 1995 (Eq. 2.16a) and RIA (Eq. (4.2))......	75
<b>Figure 4.3:</b> Annual rainfall amounts (top panel), the flux densities (positive downward) at selected depths (central panel) and the flux density map of the depth-time domain for the FSB parameterization (bottom panel, in which upward fluxes are positive, consistent with the vertical coordinate). The flux densities are comprised of liquid water and water vapor flux densities (the latter converted to its liquid water-equivalent) for scenario 1. The dashed verticals refer to soil profiles at 50 and 70 years (see Figures C.1 and C.3). The years plotted are hydrological years, starting at the beginning of the wet season (day 273 of non-leap years). ....	76
<b>Figure 4.4:</b> The same as Figure 4.3, but for the RIA parameterization. See Figures C.2 and C.4 for the profiles indicated by the dashed lines. ....	77
<b>Figure 4.5:</b> The ( $n$ , $k$ and $r^2$ ) relation for FSB (a) RIA (b) for the wettest rainfall scenario at 10 m depth.....	78
<b>Figure 4.6:</b> The filtered annual rainfall and the correlated annual recharge at 10 m depth for the wettest scenario with (FSB) (a) or (RIA) (b) parameterizations, where each filtered rainfall event is characterized by a lag time $n$ and window width $2k+1$ . ....	79
<b>Figure 4.7:</b> As Figure 5 at 20 m depth. ....	79
<b>Figure 4.8:</b> As Figure 6 at 20 m depth. ....	80
<b>Figure 4.9:</b> As Figure 5 at 60 m depth. ....	80
<b>Figure 4.10:</b> As Figure 6 at 60 m depth. ....	81
<b>Figure 4.11:</b> As Figure 5 only for (FSB) at 100 m depth. ....	81
<b>Figure 4.12:</b> Annual rainfall amounts (top panel), the flux densities (positive downward) at selected depths (central panel) and the flux density map of the depth-time domain for the FSB parameterization (bottom panel, in which upward fluxes are positive, consistent with the vertical coordinate). The flux densities are comprised of liquid water and water vapor flux densities (the latter converted to its liquid water-equivalent) for scenario 2. The dashed vertical refers to soil profiles at 103 years (see Figure 4.18). The years plotted are hydrological years, starting at the beginning of the wet season (day 273 of non-leap years). ....	84
<b>Figure 4.13:</b> As Figure 4.12 but for the RIA parameterization. The profiles for the dashed vertical in year 103 are in Figure 4.19. ....	85
<b>Figure 4.14:</b> Profiles of various variables at midnight of the 37898 <sup>th</sup> day in the 103 <sup>th</sup> hydrological year for FSB under the drier scenario. The circle indicates the region where the liquid water flux approximates zero.....	87
<b>Figure 4.15:</b> As Figure 4.14, for the RIA parameterization. ....	88

<b>Figure B.1:</b> Water vapor and liquid water fluxes along the column depth for an initial water content of 0.00 using the FSB parameterization at the indicated dimensionless times (TS) scaled by the time the liquid water flux became zero throughout the column. ....	104
<b>Figure B.2:</b> As Figure B.1, for an initial water content of 0.02. ....	105
<b>Figure B.3:</b> As Figure B.1, for an initial water content of 0.05. ....	106
<b>Figure B.4:</b> As Figure B.1, for an initial water content of 0.08. ....	107
<b>Figure B.5:</b> Water vapor and liquid water fluxes along the column depth for an initial water content of 0.00 using the RNA parameterization at the indicated dimensionless times (TS) scaled by the time the liquid water flux became zero throughout the column. ....	108
<b>Figure B.6:</b> As Figure B.5 for an initial water content of 0.02. ....	109
<b>Figure B.7:</b> As Figure B.5 for an initial water content of 0.05. ....	110
<b>Figure B.8:</b> As Figure B.5 for an initial water content of 0.08. ....	111
<b>Figure C.1:</b> Profiles of key variables at midnight at the end of the 50 <sup>th</sup> hydrological year for FSB under the wetter scenario (Figure 4.3). ....	112
<b>Figure C.2:</b> As Figure C.1, for RIA under the wetter scenario (Figure 4.4). ....	113
<b>Figure C.3:</b> Profiles of key variables at midnight at the end of the 70 <sup>th</sup> hydrological year for FSB under the wetter scenario (Figure 4.3). The black circles point to the dynamics of fluxes and the related soil properties at about 20 m depth, which are discussed in the main text ....	114
<b>Figure C.4:</b> As Figure C.3, for RIA under the wetter scenario (Figure 4.4) ....	115

## List of Tables

<b>Table 2.1:</b> The fitting parameters for five parameterizations, their physically permitted ranges, and their fitted values for four textures. The three-character parameterization label is explained in the main text. The equations to which these labels refer are given in the first column. ....	34
<b>Table 2.2:</b> Root mean square of errors (RMSE) for the different parameterizations. ....	34
<b>Table 2.3:</b> Cumulative bottom and evaporative fluxes (positive upwards) for silt from day 281 (the start of the first rainfall) onwards for Burdine and Mualem conductivity functions with the different parameterizations. The hydraulic conductivity at $h = -300$ cm (the initial condition at the bottom is also given). ....	37
<b>Table 3.1:</b> The initial conditions in volumetric water contents and in pressure heads for the various initial water contents and soil hydraulic parameterizations: BCO: Brooks and Corey (1964); FSB: Fayer and Simmons (1995); RNA: Rossi and Nimmo (1994); VGA: Ippisch et al. (2006); VGN: van Genuchten (1980). ....	57
<b>Table 3.2:</b> The time (d) at which the simulated liquid flux became zero throughout the columns for different initial water contents and soil hydraulic parameterizations. ....	63
<b>Table 4.1:</b> The parameters values of the the rainfall model with their units for each period. The periods are indicated by their starting times in the final column. For parameter $\lambda$ the first value refers to the wetter scenario (1), and the second to the drier scenario (2). ....	71
<b>Table 4.2:</b> Summary of parameter values of the temperature Eq. (4.1). ....	72
<b>Table 4.3:</b> The fitted parameters with their units and physical range for FSB and RIA. The parameters are given in equations (2.16a) and (4.2) in the main text. ....	75
<b>Table 4.4:</b> The total recharge (cm) at different depths of the soil profiles for scenario (1) with (FSB) and (RIA) and with and without considering vapor flow. ....	82
<b>Table 4.5:</b> The total recharge (cm) at different depths of the soil profiles for scenario (2) with (FSB) and (RIA) and with and without considering the vapor transport. ....	86
<b>Table A.1:</b> List of variables of Chapter 2. ....	101
<b>Table B.1:</b> The fitted parameters with their units and physical range for FSB, RNA, VGA, VGN and BCO (see Table 3.1 for an explanation of the acronyms). The parameters are given in equations (3.3) – (3.7) in the main text. ....	103

*I dedicate this thesis to my bleeding soul Syria  
and to my hope in life Joseph and Josha*

# Chapter 1

## 1. General Introduction

### 1.1. Background and Motivation

The vadose zone or the unsaturated zone is the soil layer between the land surface and the groundwater table. It is a crucial component of the terrestrial hydrological cycle because it is the layer that partitions precipitation into infiltration and surface runoff, and subsequently infiltration into evaporation, transpiration, and groundwater recharge. Because of the joint presence of oxygen, water, and a wide variety of life it is also a bio-geochemically active zone in which nutrients are recycled and reactive compounds in general are transported, adsorbed, converted, broken down and/or taken up by soil flora, fauna, microbial life, and fungi. The shallower reaches of the unsaturated zone experience daily and annual temperature cycles.

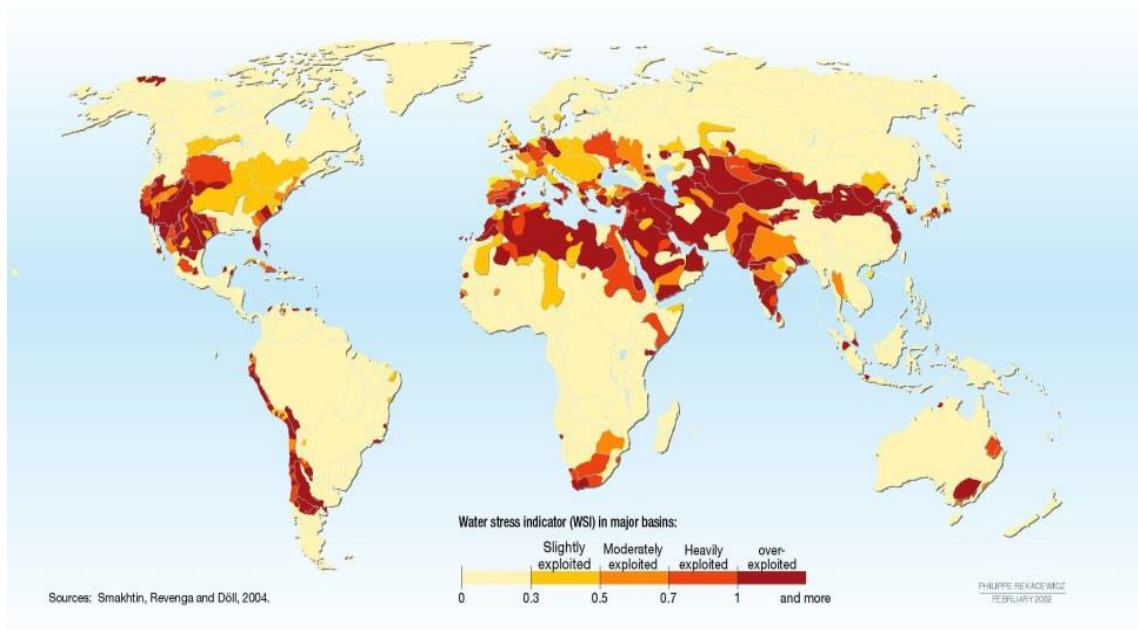


Figure 1.1: Water stress in major basins around the world. Sources: P. Rekacewicz, 2006 <http://www.grida.no/resources/5586> (accessed on June 15, 2017), WWAP (2012), p. 125.

In semi-arid regions, groundwater tables are generally many meters to hundreds of meters deep and rainfall is infrequent. Increased population density, droughts, and armed conflict have caused hardship to many inhabitants of such areas, who rely on groundwater as the only source of drinking water for humans and cattle when the rivers and wadis are dry. The United Nations (UN) foresees an increased potential for conflicts arising from scarce water resources (e.g., United Nations, 2016; WWAP, 2012,

throughout the report). It states (WWAP, 2012, p. 219) that ‘Although there may have not been an outright war over water, it has still, historically, caused sufficient violence and conflict within and among states to warrant attention (Postel and Wolf, 2001). Where water is scarce, it can be viewed and interpreted as a security threat (Gleick, 1993)’ (Barr et al., 2012). The UN expects water scarcity to increase in the next few years to the degree that ‘over 40% of countries could experience severe freshwater scarcity by 2020’, ‘mostly in low-income countries or regions in sub-Saharan Africa and Asia.’ (Cosgrove et al., 2012, WWAP, 2012, p. 265)

Physical water scarcity (caused by limited availability of water relative to demand, not by lack of access to a sufficient supply of water) is mainly concentrated in northern Africa, the Arab world, India, southern states of the Asian area of the former Soviet Union, the southwestern United States, and Mexico. Figure 1.1 gives a map of the ratio of the annual withdrawals from rivers over the difference between the long-term average annual flows through these rivers and the environmental annual water requirement. This is considered a water-stress indicator (WSI) (Smakhtin et al., 2004).

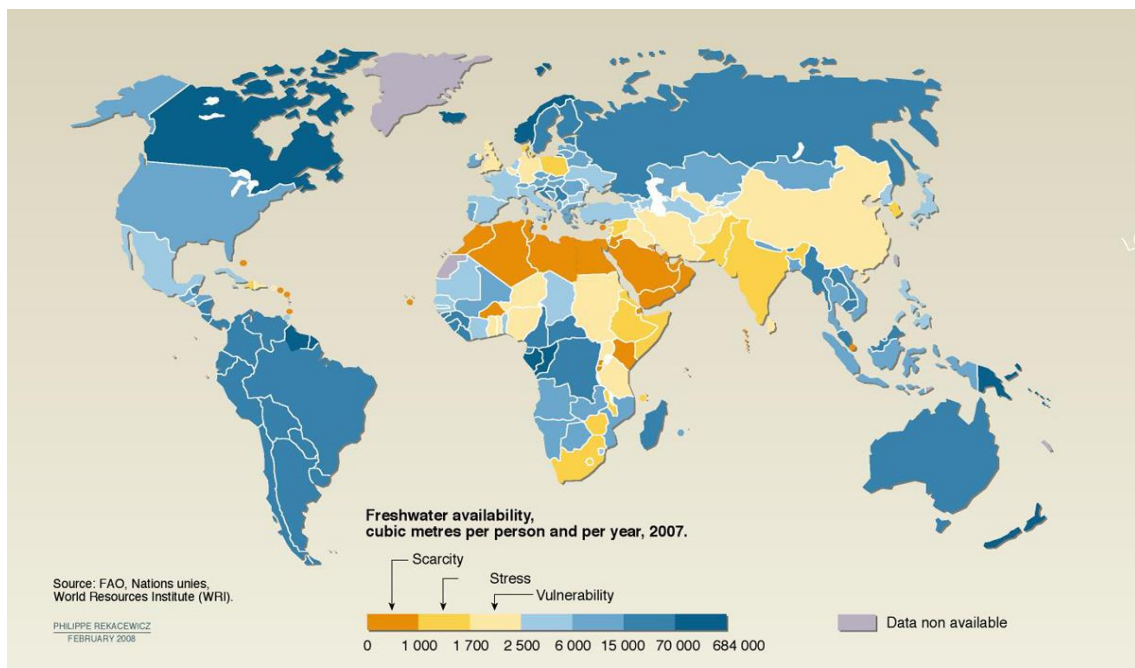


Figure 1.2: Available freshwater per capita per year by country. Source: P. Rekacewicz, 2006, <http://www.grida.no/resources/5596> (accessed June 15, 2017), based on data from Aquastat (FAO, 2016)

At the national level, freshwater availability per capita is affected by hydro-climatic conditions as well as population density. Very poor countries in dry climates are often sparsely populated and paradoxically have more water available per capita per year than moderately poor or rich nations that have the infrastructure in place to store water for the dry season, or even desalinate sea water. Still, northern Africa and the Arabian Peninsula stand out for having very limited freshwater resources. By and large, in current times, limited freshwater availability is an African and Asian problem (Fig. 1.2).

Given the pressing nature of problems related to water scarcity, there is a need to understand all aspects of the hydrological cycle in such areas. This includes but is not limited to the rainfall patterns (and how these are affected by a changing climate) and the way in which deep vadose zones convert infiltration at the soil surface to groundwater recharge. The interplay between hydrology, natural



vegetation and crops, grazers (cattle herds), rain-fed and irrigated agriculture, and the size and technological sophistication of local populations will affect the pressure on aquifers and surface waters in such regions.

A single PhD project can only cover a fraction of the issues. In this thesis, the main interest is the role deep vadose zones play in the generation of groundwater recharge in dry climates. This choice is motivated to a considerable extent by the obvious importance of groundwater as a long-term source of freshwater in regions where rivers often are ephemeral or entirely absent (Scanlon et al. 2006). Populations in these regions can thrive only when this resource is secure: excessive withdrawal will eventually lead to the decline of the communities depending upon them. This explains the advance of studies trying to quantify the replenishment of aquifers in semi-arid regions (e.g., Gee and Hillel, 1988; Osterkamp and Lane, 2003; Wang et al., 2008; Ng et al., 2010; Scanlon et al., 2010; Durbin, 2012; Flint et al., 2012; Green et al., 2012) since the 1980s. What is apparent from these studies is that they strive to estimate the magnitude of groundwater recharge in the past year, decade, century or even longer periods of time. The estimation methods largely rely on measurements of properties of the water in the aquifers themselves: ionic composition, various isotopic tracers, variations in hydraulic heads, etc. Among the most applied methods is to estimate the fraction of rainfall that reaches the aquifer from the ratio of the chloride concentration in the rainwater and in the aquifer (e.g. Scanlon et al., 2010). Sometimes, fluxes are estimated.

The methods developed lend themselves poorly to prediction and extrapolation: future groundwater recharge under changing climatic and land use conditions has been largely tackled by numerical modelling (Döll and Flörke, 2005; Toews and Allen, 2009; Chenini and Ben Mammou, 2010). Although some of these approaches could in principle be validated by now-casting the current situation based on historic data, such tests are rare. Furthermore, the models often focus on modelling the flow in the aquifer and calculate the unsaturated flows that feed the aquifer by simplified models, the validity of which is uncertain when conditions change.

In the quest for a predictive model for groundwater recharge, we should not focus on the aquifer itself, but on the pathways the water takes to reach the aquifer: through infiltration into the soil, subsequently escaping uptake by plant roots or direct evaporation, and instead percolating downward until below the root zone. There, water can still evaporate and travel upwards in the vapor phase. If that route too is avoided, the percolated water will eventually move further downwards and, possibly after decades or longer, reach the phreatic aquifer. De Vries and Simmers (2002) and Scanlon et al. (2010) consider all water that arrives below the root zone in liquid form future recharge and thus ignore evaporation below the root zone. In contrast, Barnes and Turner (1998) report considerable mass transport in the unsaturated zone in the vapor phase driven by thermal gradients in a deep (>10 m) sand dune soil, and de Vries and Simmers (2002) review work that reports significant effects of vapor fluxes on recharge. The many routes back to the atmosphere make it plausible that groundwater recharge is mainly driven by unusually heavy showers that exceed the capacity of the root system to capture soil water (see also de Vries and Simmers, 2002) and generate a significant downward flow at considerable depth. For deep vadose zones, an infiltration front driven by a single event may dissipate before reaching the groundwater. Hence, even individual heavy showers may require additional infiltration caused by relatively wet years shortly before or after them to have enough soil moisture present over longer periods to ensure that some of the water travels all the way down to the groundwater.

This thesis is concerned with the percolation of water from the soil surface to the phreatic aquifer through a thick unsaturated zone. The processes of interest are the flow of liquid water and water vapor

and their interaction, and the effect of temperature on these flows. All of these are heavily influenced by the architecture of the pore space, since this architecture determines how much water is retained by the soil at a certain potential energy (and thus, how much pore space is occupied by the two mobile phases: the liquid and the gas phase), and how well the soil conducts water and air at a given water content. The presence of liquid water and air in the pore space is quantified through the soil water retention curve. The spatial distribution of both mobile phases determines the conductivity to water and air. For the first, the soil hydraulic conductivity curve can be used. For gas this is less usual because significant air pressure gradients that drive air flow arise only on rare occasions (for instance during rapid infiltration, when the infiltrating water rapidly displaces a large portion of the gas phase). Most of the time, gas movement is by diffusion, and a relationship between the gas diffusion constant and the soil water content is needed.

The thesis presents a critical review of existing parameterizations of the soil water retention curve and their effect on parametric forms of the soil hydraulic conductivity curve, and offers improvements of some of them based on theoretical considerations. It examines experimentally the interplay between liquid water flow and water vapor flow in a simple porous medium under dry conditions. Through numerical simulations, the effect of different parameterizations on water and vapor fluxes in the unsaturated zone is explored.

## **1.2. Objectives and hypothesis of the thesis**

The main objectives of this thesis are to:

- i) Test and where necessary improve the capability of soil hydraulic parameterizations to adequately describe liquid water flow in dry soils
- ii) Explore the role of vapor flow in deep vadose zones through numerical simulations taking into account heat flow and the geothermal gradient.
- iii) Examine the effect of rainfall patterns and soil hydraulic properties on groundwater recharge under arid conditions through long-term numerical simulations.

The hypotheses to be verified or falsified are:

- i) Using different soil hydraulic parameterizations leads to different modelled water fluxes and consequently to a significant difference in the estimations of ground water recharge.
- ii) Vapor fluxes have a significant effect on the deep water fluxes, and thus on ground water recharge.
- iii) The groundwater recharge through a thick vadose zone is dominated by long clusters of rainfall events.

## Chapter 2

### 2. Parametric soil water retention models: a critical evaluation of expressions for the full moisture range

#### Abstract:

Of the many parametric expressions for the soil water retention curve, only a few are suitable for the dry range. Furthermore, expressions for the soil hydraulic conductivity curves associated with these retention functions can exhibit non-physical behavior near saturation. We developed a general criterion that needs to be met by soil water retention parameterizations to ensure physically plausible hydraulic conductivity curves. Only three of the 18 tested parameterizations did not impose any restrictions on the parameters of the most popular conductivity curve parameterization, which includes three functions as special cases. One other retention function required one conductivity parameter to be fixed.

We employed the Shuffled Complex Evolution parameter estimation method with the objective function tailored to various observation methods normally used to obtain retention curve data. We fitted the four parameterizations with physically plausible conductivities as well as the most widely used parameterization. We then compared the performance of the resulting 12 combinations of retention curve and conductivity curve in a numerical study with 751 days of semi-arid atmospheric forcing applied to unvegetated, uniform, 1-m freely draining columns for four textures.

Choosing different parameterizations had a minor effect on evaporation, but cumulative bottom fluxes varied by up to an order of magnitude between them. This highlights the need for a careful selection procedure for the parameterization of the soil hydraulic properties that ideally does not only rely on goodness-of-fit to static soil water retention data but also on observations of the hydraulic conductivity curve made during dynamic flow conditions.

#### 2.1. Introduction

Numerical solvers of Richards' equation for water flow in unsaturated soils require the soil water retention curve and soil hydraulic curve as descriptors of the soil in which the movement of water should be calculated. Many parametric expressions for the retention curve and fewer for the hydraulic conductivity have been developed for that purpose (see section 2.2, Leij et al. (1997), Cornelis et al., (2005), Durner and Flühler (2005), and Khlosi et al. (2008)).

A brief overview of retention curve parameterizations is given in the following while the references to the parameterizations in question are given in section 2.2, where their equations are presented. The earliest developed parameterizations focused primarily on the wet end of the curve since this is the most relevant section for agricultural production. Numerical models were struggling with the discontinuity of the first derivative at the air-entry value. Observations with methods relying on hydrostatic equilibrium (Klute, 1986, p. 644-647) typically gave a more smooth shape around the matric

potential where the soil started to desaturate as an artefact of the sample height, as was later demonstrated by Liu and Dane (1995). This led to the introduction of parameterizations that yielded a continuously differentiable curve.

The interest in the dry end of the retention curve was triggered by an increased interest in water scarcity issues (e.g. Scanlon et al., 2006; UN-Water, FAO, 2007; UNDP, 2006; see also Chapter 1 section 1.1). For groundwater recharge under deep vadose zones, the dry end of the soil water retention curve affects both slow liquid water movement in film and corner flow (Tuller and Or, 2001; Lebeau and Konrad, 2010) and vapor phase transport (Barnes and Turner, 1998; de Vries and Simmers, 2002). The earlier parameterizations had an asymptote at a small (or zero) water content. This often gave poor fits in the dry end, and several parameterizations emerged in which the dry branch was represented by a logarithmic function that reached zero water content at some point.

A non-parametric approach was advocated by Iden and Durner (2008). They estimated nodal values of volumetric water content from evaporation experiments and derived a smooth retention curve by cubic Hermite interpolation. They extrapolated the retention function to the dry range and compute a coupled conductivity function based on the Mualem model.

Liu and Dane (1995) were the first to point out that the smoothness of observed curves around the air-entry value could be an artefact related to experimental conditions. Furthermore, it became apparent that a particular parameterization that gave a differentiable curve led to unrealistically large increases of the soil hydraulic conductivity near saturation (Durner, 1994; Vogel et al., 2001). This was eventually linked to the non-zero slope at saturation (Ippisch et al., 2006), implying the existence of unphysically large pores with air-entry values up to zero. This led to the re-introduction of a discrete air-entry value.

Most of the parameterizations are empirical, curve-fitting equations (Kosugi et al., 2002). One exception is the very dry range, where measurement techniques are often not so reliable (e.g., Campbell and Shiozawa, 1992) and were not always employed. The proportionality of the water content in this range to the logarithm of the absolute value of the matric potential that has frequently been invoked conforms to the adsorption theory of Bradley (1936), which considers adsorbed water molecules to build up in a film consisting of layers, with the net force of electrical attraction diminishing with every layer (Rossi and Nimmo, 1994).

The power-law relationship between water content and matric potential introduced by Brooks and Corey (1964) was given a theoretical foundation by Tyler and Wheatcraft (1990), who showed that the exponent was related to the fractal dimension of the Sierpinski carpet used to model the hierarchy of pore sizes occurring in the soil. The sigmoid shape of the Kosugi's (1996, 1999) retention curve was derived rigorously from an assumed lognormal distribution of effective pore sizes, making this the only parameterization discussed in this paper developed from a theoretical analysis.

Some soils have different types of pore spaces: one type appears between individual grains. Its architecture is determined by soil texture, and by the geometry of the packing of the individual grains. The second type appears at a large scale: the soil may consist of aggregates (e.g., Coppola, 2000, and references therein), and the pore space between these aggregates is very different from those between the grains. Biopores formed by roots that have since decayed, soil fauna, etc. also can create a separate type of pore space. In shrinking soils, a network of cracks may form. The volume and architecture of these pore spaces are essentially independent of the soil texture (Durner, 1994), even though a certain texture may be required for these pores to form. In soils with such distinct pore spaces, the derivative of the soil water retention curve may have more than a single peak, and for this reason multimodal retention curves have been proposed, e.g., by Durner (1994) and Coppola (2000). Most of the parametric expressions for

the soil water retention curve are unimodal though. Durner (1994) circumvented this by constructing a multimodal retention curve by summing up several curves of the same type but with different parameter values. He presented excellent fits of bimodal retention functions at the price of adding three or four parameters depending on the chosen parameterization. Coppola (2000) used a single-parameter expression for the intra-aggregate pore system superimposed on a 5-parameter expression for the inter-aggregate pores, thereby reducing the number of fitting parameters and the degree of correlation among these.

The wealth of parameterizations for the soil water retention curve calls for a robust fitting method applicable to various parameterizations and capable of handling data with different data errors. These errors arise from the various measurement techniques used to acquire data over the full water content range. Parameter fitting codes are available (e.g., Schindler et al., 2015), but they do not fit the parameterizations focusing on the dry end. The first objective of this chapter is to introduce a parameter fitting procedure that involves an objective function that accounts for varying errors, embedded in a shell that allows a wide spectrum of retention function parameterizations to be fitted.

The analysis by Ippisch et al. (2006) of the effect of the shape of the soil water retention curve on the hydraulic conductivity near saturation considered van Genuchten's (1980) parameterization in combination with Mualem's (1976) conductivity model only. Iden et al. (2015) approached the same problem but only examined the conductivity curve. They too focused on the van Genuchten-Mualem configuration only. The analysis of Ippisch et al. (2016) could well have ramifications for other parameterizations. A second objective of this chapter therefore is the development of a more general analysis based on Ippisch et al. (2006) and its application to other parameterizations of the retention and conductivity curves.

Several hydraulic conductivity parameterizations that relied only on observations of soil water retention data have been developed (see the review by Mualem, 1992). Many of these consider the soil layer or sample for which the conductivity is sought as a slab of which the pore architecture is represented by a bundle of cylindrical tubes with a given probability density function (pdf) of their radii. This slab connects to another slab with a different pore radius pdf. By making different assumptions regarding the nature of the tubes and their connectivity, different expressions for the unsaturated hydraulic conductivity can be found (Mualem and Dagan, 1978). Raats (1992) distinguished five steps in this process: 1) Specify the effective areas occupied by connected pairs of pores of different radii that reflect the nature of the correlation between the connected pore sizes; 2) Account for tortuosity in one of various ways; 3) Define the effective pore radius as a function of both radii of the connected pairs of pores; 4) Convert the pore radius to a matric potential at which the pore fills or empties; 5) Use the soil water retention curve to convert from a dependence upon the matric potential to a dependence upon the water content. Only step 5 constitutes a direct effect of the choice of the retention curve parameterization on the conductivity curve. Choices made in steps 1-3 result in different conductivity curves associated with any particular retention curve parameterization.

The functions that have found widespread application in numerical models can be captured by Kosugi's (1999) generalized model. In this chapter, we limit ourselves to three parameterizations as special cases of Kosugi's general model, and discuss them in more detail in section 2.2. In doing so, we add to the existing body of comparative studies of parametric retention curves by explicitly including the associated hydraulic conductivity curves according to these conductivity models. Papers introducing new parameterizations of the soil water retention curve as well as reviews of such parameterizations typically show the quality of the fit to soil water retention data (e.g., van Genuchten, 1980; Rossi and Nimmo,

1994; Cornelis et al., 2005; Khlosi et al., 2008). The role of these parameterizations is to be used in solutions of Richards' equation, usually in the form of a numerical model. Their performance can therefore be assessed through the water content and water fluxes in the soil calculated by a numerical Richards' solver. This is not often done, one exception being the field-scale study by Coppola et al. (2009) comparing unimodal and bimodal retention curves and the associated conductivity curves in a stochastic framework on the field scale, for a 10-day, wet period. A third objective therefore is to carry out a numerical modeling exercise to examine the differences in soil water fluxes calculated on the basis of various parameterizations by the same model for the same scenario. Here, the inclusion of the conductivity curves in the comparison is taken to its logical conclusion by carrying out simulations for all possible combinations of retention and conductivity models.

Should the differences in the fluxes be small, the choice of the parameterizations can be based on convenience. If they are significant, even if the fits to the data are fairly similar, this points to a need of a more thorough selection process to determine the most suitable parameterization.

## 2.2. Theory

### 2.2.1. Hydraulic conductivity models and their behavior near saturation

The pore architecture of the soil influences its hydraulic behavior, typically described by two curves: the relationship between the amount of water present in the soil pores and the matric potential (termed soil water characteristic or soil water retention curve), and the relationship between the hydraulic conductivity and either matric potential or water content (the soil hydraulic conductivity curve).

Numerous functions have been proposed to describe the soil water retention curve, several of them reviewed below. Fewer functions exist to describe the soil hydraulic conductivity curve. When these rely on the retention parameters, one can use the retention curve to predict the conductivity curve. However, when both retention and conductivity data exist, a single set of parameters does not always fit both curves well, even if both sets of data are used in the fitting process. It may therefore be prudent to attempt to find a retention-conductivity pair of curves that share a number of parameters that could be fitted on retention data only and has additional parameters that only occur in the expression for the hydraulic conductivity.

Various theoretical models exist to determine the unsaturated hydraulic conductivity  $K$  [ $LT^{-1}$ ] as a function of matric potential  $h$ [L] or volumetric water content  $\theta$  from the soil water retention curve, (see Appendix A for a list of the variables used in this chapter). Hoffmann-Riem et al. (1999) and Kosugi (1999) identified a generalized model that captured the two most widely used hydraulic conductivity models and several others. The formulation according to Kosugi (1999) is:

$$K(S_e) = K_s S_e^\tau \left( \frac{\int_0^{S_e} |h|^{-\kappa}(x) dx}{\int_0^1 |h|^{-\kappa}(x) dx} \right)^\gamma \quad (2.1)$$

where the subscript  $s$  denotes the value at saturation,  $x$  is an integration variable, and  $\gamma$ ,  $\kappa$ , and  $\tau$  are dimensionless shape parameters. The degree of saturation  $S_e$  is defined as:

$$S_e(h) = \frac{\theta(h) - \theta_r}{\theta_s - \theta_r} \quad (2.2)$$

where the subscript  $r$  denotes the irreducible value ( $\geq 0$ ). After a change of variables this gives (Ippisch et al. 2006)

$$K(h) = K(h(S_e)) = \begin{cases} K_s S_e^\tau \left( \frac{\int_{-\infty}^{h(S_e)} |h|^{-\kappa} \frac{dS}{dh} dh}{\int_{-\infty}^{h_{ae}} |h|^{-\kappa} \frac{dS}{dh} dh} \right)^\gamma, & h \leq h_{ae} \\ K_s, & h \geq h_{ae} \end{cases} \quad (2.3)$$

where  $h_{ae}[\text{L}]$  is the air-entry value of the soil and  $S$  denotes the degree of saturation moving between 0 and the actual value  $S_e$ . Note that the value of  $S(h)$  and  $dS/dh$  are directly related to the soil water retention curve  $\theta(h)$  through Eq. (2.2). Specific models can be found by fixing the parameters: Burdine's (1953) model is obtained with  $\gamma = 1$ ,  $\kappa = 2$ , and  $\tau = 2$ , the popular model of Mualem (1976) results with  $\gamma = 2$ ,  $\kappa = 1$  and  $\tau = 0.5$ , and the model of Alexander and Skaggs (1986) requires  $\gamma = \kappa = \tau = 1$ . When any of these models are used, the soil water retention parameters can be used to predict the conductivity curve if no conductivity data are available and the saturated hydraulic conductivity can be estimated independently (see Jarvis et al., 2002, and references therein). Note that positive values of  $\kappa$  ensure that large pores (emptying at smaller values of  $|h|$ ) contribute more to the overall hydraulic conductivity than small pores, which is physically sound. Parameter  $\gamma$  should be positive as well. Negative values would lead to a switch of the numerator and denominator (which scales the numerator by its maximum value) in Eq. (2.1), which is illogical. Peters (2014) required that the conductivity curve monotonically decreases as the soil dries out and derived a minimal value of -2 for  $\tau$  from that requirement. Indeed, negative values of this parameter have been reported (e.g. Schaap and Leij, 2000), even though the three predictive models mentioned above all have positive values of  $\tau$ .

Driven by the occasionally unrealistic shape of Mualem's (1976) hydraulic conductivity curve near saturation, Ippisch et al. (2006) rigorously analyzed the version of Eq. (2.3) specific to Mualem's (1976) model. They concluded that the integrand must approach zero near saturation in order to prevent unrealistically large virtual pores dominating the hydraulic conductivity of very wet soils, a point raised earlier by Durner (1994). We generalize their criterion for prohibiting excessively larger pores from dominating the conductivity near saturation for arbitrary parameter values (after converting  $dS/dh$  to  $d\theta/dh$ ) by

$$\lim_{h \rightarrow 0} \left( |h|^{-\kappa} \frac{d\theta}{dh} \right) = 0 \quad (2.4)$$

This condition is automatically met by retention curves with non-zero air-entry values, but restricts the permissible value of  $\kappa$  if the retention curve has non-zero derivatives at saturation, and couples it to this derivative.

Iden et al. (2015) argued that limiting the maximum pore size of the pore-bundle models that gave rise to models of the type of Eq. (2.1) eliminated the large pores that caused the excessively rapid rise of the hydraulic conductivity near saturation. By only modifying the conductivity function without changing the water retention function, a discrepancy emerges between the retention curve (which reflects the presence of unphysically large pores) and the conductivity curve (which does not). Retention curves with a distinct air-entry value maintain the desired consistency, at the price of having non-continuous derivatives, which may create problems for numerical solvers of Richards' equation.

### 2.2.2. Critical evaluation of parametric functions of the soil water retention curve

This section summarizes the most popular parameterizations of the soil water retention curve and several lesser-known others that were developed to improve the fit in the dry range or at least eliminate the need for the physically poorly defined residual water content. At this time, we consider unimodal functions only. The physical plausibility in terms of the rate of change near saturation of the corresponding conductivity models is verified, thereby maintaining the consistency between the retention and the conductivity curves that would have been lost in Iden et al.'s (2015) approach. In all cases but one, this physical plausibility is checked for the first time. The plausibility check requires that the derivative of each retention curve is determined and the criterion in Eq. (2.4) is used to define the permissible range for  $\kappa$ . If this range does not include any of the values  $\{1, 2\}$  used by the conductivity models described above, or if the permitted values are non-physical ( $< 0$ ), the retention model does not have a conductivity model associated with it, which limits its practical value. As above,  $h$  denotes the matric potential, which is negative in unsaturated soils. Many of the cited papers adopt this notation for its reciprocal, the suction.

The water retention function of Brooks and Corey (1964) is:

$$\theta(h) = \begin{cases} \theta_r + (\theta_s - \theta_r) \left( \frac{h}{h_{ae}} \right)^{-\lambda}, & h \leq h_{ae} \\ \theta_s, & h > h_{ae} \end{cases} \quad (2.5a)$$

This equation is referred to as BCO below. The derivative is:

$$\frac{d\theta}{dh} = \begin{cases} -\frac{\lambda(\theta_s - \theta_r)}{h_{ae}} \left( \frac{h}{h_{ae}} \right)^{-\lambda-1}, & h \leq h_{ae} \\ 0, & h > h_{ae} \end{cases} \quad (2.5b)$$

where  $\lambda$  is a dimensionless fitting parameter. If  $\theta_r$  is set to zero, Campbell's (1974) equation is obtained.

The analytical expression for the generalized  $K(h)$  function (Eq. 2.3) for the water retention function of Brooks and Corey (1964) is



$$K(h) = \begin{cases} K_s \left( \frac{h(S_e)}{h_{ae}} \right)^{-\lambda\tau} \left\{ \frac{\left[ \frac{\lambda(\theta_s - \theta_r)h_{ae}^\lambda}{\kappa + \lambda + 2} |h|^{-\kappa - \lambda} \right]^{h_{ae}}}{\left[ \frac{\lambda(\theta_s - \theta_r)h_{ae}^\lambda}{\kappa + \lambda + 2} |h|^{-\kappa - \lambda} \right]^{-\infty}} \right\}^\gamma & h \leq h_{ae} \\ K_s, & h > h_{ae} \end{cases} = K_s \left( \frac{h_{ae}}{h} \right)^{\lambda(\gamma + \tau) + \gamma\kappa}, \quad (2.5c)$$

Note that the Brooks-Corey retention curve allows all three parameters of the associated conductivity model to be fitted.

The derivative of the Brooks-Corey function is discontinuous at  $h_{ae}$ . Hutson and Cass (1987) added a parabolic approximation at the wet end to make the first derivative continuous. For  $\theta_r = 0$ , they proposed

$$\theta(h) = \begin{cases} \theta_s \left( \frac{h}{h_{ae}} \right)^{-\lambda}, & h \leq h_i \\ \theta_s \left[ 1 - \left( \frac{h}{h_{ae}} \right)^2 \frac{\left( 1 - \frac{2}{\lambda + 2} \right)}{\left( \frac{2}{\lambda + 2} \right)^{\frac{2}{\lambda}}} \right], & 0 \geq h > h_i \end{cases} \quad (2.6a)$$

where  $h_i$  [L] is the matric potential at the inflection point, given by:

$$h_i = h_{ae} \left( \frac{2}{2 - \lambda} \right)^{\frac{1}{\lambda}}. \quad (2.6b)$$

The derivative is

$$\frac{d\theta}{dh} = \begin{cases} -\frac{\lambda\theta_s}{h_{ae}} \left( \frac{h}{h_{ae}} \right)^{-\lambda-1}, & h \leq h_i \\ \frac{2\theta_s}{h_{ae}} \frac{\left( \frac{2}{\lambda + 2} - 1 \right)}{\left( \frac{2}{\lambda + 2} \right)^{\frac{2}{\lambda}}} \left( \frac{h}{h_{ae}} \right), & 0 \geq h > h_i \end{cases}. \quad (2.6c)$$

The parameter  $h_{ae}$  no longer is an air-entry value and should be considered a pure fitting parameter. It should be noted that the smooth transition to saturation that this function and several others mimic may at

least in part be caused by the non-zero height of the soil cores used in experiments to determine soil water retention curves. At hydrostatic equilibrium, the matric potential along the vertical varies in the soil core, resulting in a differentiable shape of the apparent soil water retention curve, even if the soil in the core has a uniform air-entry value that leads to a locally non-differentiable curve (Liu and Dane, 1995).

The parabolic approximation of Hutson and Cass (1987) leads to the following expression for the term in Eq. (2.4)

$$\lim_{h \rightarrow 0} A_1 |h|^{1-\kappa} = 0 \quad (2.7)$$

where  $A_1$  is a constant. This leads to the requirement that  $\kappa < 1$ , ruling out the usual models. Although the parabolic approximation in itself does not preclude the existence of a closed-form expression for  $K$ , the restriction on  $\kappa$  is quite severe, so we do not pursue this further.

Van Genuchten's (1980) formulation is also continuously differentiable:

$$\theta(h) = \theta_r + (\theta_s - \theta_r) \left(1 + |\alpha h|^n\right)^{-m}, \quad h \leq 0 \quad (2.8a)$$

where  $\alpha$  [ $L^{-1}$ ],  $n$ , and  $m$  are shape parameters. This equation is denoted by VGN below. It has the derivative

$$\frac{d\theta}{dh} = \alpha m n (\theta_s - \theta_r) |\alpha h|^{n-1} \left(1 + |\alpha h|^n\right)^{-m-1}, \quad h \leq 0 \quad (2.8b)$$

where often  $m$  is set equal to  $1 - 1/n$ .

The limit of the derivative of van Genuchten's (1980) retention curve near saturation is

$$\left. \frac{d\theta}{dh} \right|_{h=0} = \alpha^n m n (\theta_s - \theta_r) |h|^{n-1} \quad (2.9)$$

leading to the requirement that  $\kappa < n-1$ . For many fine and/or poorly sorted soil textures,  $n$  ranges between 1 and 2. Therefore, this restriction can be even more severe than the one required for a parabolic wet end, even excluding Mualem's (1976) conductivity model when  $n < 2$ . For this reason we refrain from formulating analytical conductivity equations, even though van Genuchten (1980) presented such expressions for Burdine's (1953) and Mualem's (1976) models.

Vogel et al. (2001) presented a modification to improve the description of the hydraulic conductivity near saturation without being aware of the physical explanation of the poor behavior presented later by Ippisch et al. (2006). Their retention function reads

$$\theta(h) = \begin{cases} \theta_r + (\theta_m - \theta_r) \left(1 + |\alpha h|^n\right)^{-m}, & h < h_s \\ \theta_s, & h \geq h_s \end{cases} \quad (2.10a)$$

where  $h_s$  [L] is a fitting parameter close to zero with which  $\theta_m$  can be defined as

$$\theta_m = \theta_r + (\theta_s - \theta_r) \left(1 + |\alpha h_s|^n\right)^{-m} \quad (2.10b)$$

The derivative is

$$\frac{d\theta}{dh} = \begin{cases} \alpha m n (\theta_m - \theta_r) |\alpha h|^{n-1} \left(1 + |\alpha h|^n\right)^{-m-1}, & h < h_s \\ 0, & h \geq h_s \end{cases} \quad (2.10c)$$

Schaap and van Genuchten (2006) reported a value of  $h_s$  of  $-4$  cm to work best for a wide range of soils to improve the description of the near-saturated hydraulic conductivity. The parameter  $h_s$  should therefore not be viewed as an air-entry value.

Although an expression can be derived for  $K(h)$  if  $\kappa$  is set to 1 and  $m = 1 - 1/n$ , we prefer to adopt the formulation by Ippisch et al. (2006), given its solid physical footing. They proposed to introduce an air-entry value and scale the unsaturated portion of the retention curve by its value at the water-entry value:

$$\theta(h) = \begin{cases} \theta_r + (\theta_s - \theta_r) \left( \frac{1 + |\alpha h|^n}{1 + |\alpha h_{ae}|^n} \right)^{-m}, & h < h_{ae} \\ \theta_s, & h \geq h_{ae} \end{cases} \quad (2.11a)$$

with derivative

$$\frac{d\theta}{dh} = \begin{cases} \alpha m n (\theta_s - \theta_r) |\alpha h|^{n-1} \left(1 + |\alpha h_{ae}|^n\right)^m \left(1 + |\alpha h|^n\right)^{-m-1}, & h < h_{ae} \\ 0, & h \geq h_{ae} \end{cases} \quad (2.11b)$$

With the common restriction of  $m = 1 - 1/n$ , an expression can be found for  $\kappa=1$  that is slightly more general than Eq. (11) in Ippisch et al. (2006):

$$K(h) = \begin{cases} K_s \left( \frac{\theta - \theta_r}{\theta_s - \theta_r} \right)^\tau \left[ \frac{1 - \left( 1 - \frac{1}{B(h)} \right)^{\frac{n}{n-1}}}{1 - \left( 1 - \frac{1}{C} \right)^{\frac{n}{n-1}}} \right]^\gamma \\ = K_s \left( \frac{B(h)}{C} \right)^{\tau \left( \frac{1}{n} - 1 \right)} \left[ \frac{1 - \left( 1 - \frac{1}{B(h)} \right)^{\frac{n}{n-1}}}{1 - \left( 1 - \frac{1}{C} \right)^{\frac{n}{n-1}}} \right]^\gamma, & h < h_{ae} \\ K_s, & h \geq h_{ae} \end{cases} \quad (2.11c)$$

where

$$B(h) = 1 + |\alpha h|^n \quad (2.11d)$$

$$C = 1 + |\alpha h_{ae}|^n \quad (2.11e)$$

This equation can be used to define conductivity models according to Mualem (1976) and Alexander and Skaggs (1986), which both require that  $\kappa=1$ .

None of the retention models discussed so far performs very well in the dry range. Campbell and Shiozawa (1992) introduced a logarithmic section in the dry end to improve the fit in the dry range:

$$\theta(h) = \theta_a \left( 1 - \frac{\ln|h|}{\ln|h_d|} \right) + A_2 \left( \frac{1}{1 + |\alpha h|^4} \right)^m \quad (2.12a)$$

with derivative

$$\frac{d\theta}{dh} = \frac{\theta_a}{\ln|h_d|} \frac{1}{h} + 4\alpha m A_2 |\alpha h|^3 \left( 1 + |\alpha h|^4 \right)^{-m-1} \quad (2.12b)$$

where  $\theta_a$  represents the maximum amount of adsorbed water,  $A_2$  is a constant and  $h_d$  is the matric potential at oven-dryness, below which the water content is assumed to be zero. The first term in the derivative leads to the requirement that  $\kappa < -1$ , and therefore no conductivity model can be derived from Eq. (2.12a).

Rossi and Nimmo (1994) also preferred a logarithmic function over the Brooks-Corey power law at the dry end to better represent the adsorption processes that dominates water retention in dry soils, as opposed to capillary processes in wetter soils. They also implemented a parabolic shape at the wet end as proposed by Hutson and Cass (1987). Rossi and Nimmo (1994) presented two retention models, but only

one (the junction model) permitted an analytical expression of the unsaturated hydraulic conductivity. Here, the junction model is presented with and without the parabolic expression for the wet end of the retention curve. With the discontinuous derivative at the air-entry value, the expression reads

$$\theta(h) = \begin{cases} 0, & h \leq h_d \\ \theta_s \beta \ln\left(\frac{h_d}{h}\right), & h_d < h \leq h_j \\ \theta_s \left(\frac{h_{ae}}{h}\right)^\lambda, & h_j < h \leq h_{ae} \\ \theta_s, & h > h_{ae} \end{cases} \quad (2.13a)$$

which is denoted RNA below. The derivative is

$$\frac{d\theta}{dh} = \begin{cases} 0, & h \leq h_d \\ \frac{\theta_s \beta}{-h}, & h_d < h \leq h_j \\ \lambda \theta_s \left|\frac{h_{ae}}{h}\right|^\lambda |h|^{-\lambda-1}, & h_j < h \leq h_{ae} \\ 0, & h > h_{ae} \end{cases} \quad (2.13b)$$

Rossi and Nimmo (1994) required the power law and logarithmic branches as well as their first derivatives to be equal at the junction point  $(\theta_j, h_j)$ . With  $h_d$  fixed (Rossi and Nimmo found a value of  $-10^5$  m for six out of seven soils and  $-5 \cdot 10^5$  m for the seventh), these constraints allow two of the five remaining free parameters to be expressed in terms of the other three. Some manipulation leads to the expressions:

$$\lambda = \frac{1}{\ln|h_d| - \ln|h_j|} \quad (2.13c)$$

$$\beta = \lambda \left(\frac{h_{ae}}{h_j}\right)^\lambda \quad (2.13d)$$

but other choices are possible. This choice leads to fitting parameters  $h_{ae}$ ,  $h_j$ , and  $\theta_s$ . The associated conductivity model is

$$K(h) = \begin{cases} 0, & h \leq h_d \\ K_s S_e^\tau \left\{ \frac{\left[ -\frac{\theta_s \beta}{\kappa} |h|^{-\kappa} \right]_{h_d}^h}{\left[ -\frac{\theta_s \beta}{\kappa} |h|^{-\kappa} \right]_{h_d}^{h_j} - \left[ \frac{\theta_s \lambda}{\lambda + \kappa} |h_{ae}|^\lambda |h|^{-(\lambda + \kappa)} \right]_{h_j}^{h_{ae}}} \right\}^\gamma, & h_d < h \leq h_j \\ = K_s \left[ \beta \ln \left( \frac{h_d}{h} \right) \right]^\tau \left[ \frac{E(h)}{E(h_j) + F \left( |h_j|^{-\lambda - \kappa} - |h_{ae}|^{-\lambda - \kappa} \right)} \right]^\gamma, & h_d < h \leq h_j \\ K_s S_e^\tau \left\{ \frac{\left[ -\frac{\theta_s \beta}{\kappa} |h|^{-\kappa} \right]_{h_d}^{h_j} - \left[ \frac{\theta_s \lambda}{\lambda + \kappa} |h_{ae}|^\lambda |h|^{-(\lambda + \kappa)} \right]_{h_j}^h}{\left[ -\frac{\theta_s \beta}{\kappa} |h|^{-\kappa} \right]_{h_d}^{h_j} - \left[ \frac{\theta_s \lambda}{\lambda + \kappa} |h_{ae}|^\lambda |h|^{-(\lambda + \kappa)} \right]_{h_j}^{h_{ae}}} \right\}^\gamma, & h_j < h \leq h_{ae} \\ = K_s \left( \frac{h_{ae}}{h} \right)^{\lambda \tau} \left[ \frac{E(h_j) + F \left( |h_j|^{-\lambda - \kappa} - |h|^{-\lambda - \kappa} \right)}{E(h_j) + F \left( |h_j|^{-\lambda - \kappa} - |h_{ae}|^{-\lambda - \kappa} \right)} \right]^\gamma, & h_j < h \leq h_{ae} \\ K_s, & h > h_{ae} \end{cases} \quad (2.13e)$$

where

$$E(h) = \frac{\beta}{\kappa} \left( |h_d|^{-\kappa} - |h|^{-\kappa} \right) \quad (2.13f)$$

$$F = \frac{\lambda}{\lambda + \kappa} |h_{ae}|^\lambda \quad (2.13g)$$

The junction model of Rossi and Nimmo (1994) with a continuous first-order derivative achieved through the correction by Hutson and Cass (1987) reads

$$\theta(h) = \begin{cases} 0, & h \leq h_d \\ \theta_s \zeta_1 \ln \left( \frac{h_d}{h} \right), & h_d < h \leq h_j \\ \theta_s \left( \frac{h_{ae}}{h} \right)^\lambda, & h_j < h \leq h_i \\ \theta_s \left[ 1 - c_1 \left( \frac{h}{h_c} \right)^2 \right], & h_i \leq h \leq 0 \end{cases} \quad (2.14a)$$

with the derivative

$$\frac{d\theta}{dh} = \begin{cases} 0, & h \leq h_d \\ \frac{\theta_s \zeta_1}{-h}, & h_d < h \leq h_j \\ \lambda \theta_s |h_{ae}|^\lambda |h|^{-\lambda-1}, & h_j < h \leq h_i \\ \frac{-2c_1 \theta_s}{h_c^2} h, & h_i \leq h \leq 0 \end{cases} \quad (2.14b)$$

where

$$h_i = h_c \left( \frac{\lambda}{2} + 1 \right)^{\frac{1}{\lambda}} \quad (2.14c)$$

$$h_j = h_d e^{-\frac{1}{\lambda}} \quad (2.14d)$$

$$c_1 = \frac{\lambda}{2} \left( \frac{2}{\lambda + 2} \right)^{\frac{\lambda+2}{\lambda}} \quad (2.14e)$$

$$\zeta_1 = e\lambda \left( \frac{h_c}{h_d} \right)^\lambda \quad (2.14f)$$

where  $h_c$  [L] is a fitting parameter, together with  $\lambda$  and  $\theta_s$ . The parabolic wet end restricts  $\kappa$  to values between 0 and 1. For this reason, an expression for the conductivity curve is not derived.

Rossi and Nimmo (1994) also introduced an equation that summed up the power law and logarithmic contributions (the sum model):

$$\theta(h) = \begin{cases} 0, & h \leq h_d \\ \theta_s \left[ \left( \frac{h_c}{h} \right)^\lambda - \left( \frac{h_c}{h_d} \right)^\lambda + \zeta_2 \ln \left( \frac{h_d}{h} \right) \right], & h_d \leq h \leq h_i \\ \theta_s \left[ 1 - c_2 \left( \frac{h}{h_c} \right)^2 \right], & h_i \leq h \leq 0 \end{cases} \quad (2.15a)$$

with derivative

$$\frac{d\theta}{dh} = \begin{cases} 0, & h \leq h_d \\ -\frac{\theta_s}{h} \left[ \lambda \left( \frac{h_c}{h} \right)^\lambda + \zeta_2 \right], & h_d \leq h \leq h_i \\ -\frac{2c_2\theta_s}{h_c^2} h, & h_i \leq h \leq 0 \end{cases} \quad (2.15b)$$

in which we have

$$\zeta_2 = \left[ 1 - \left( \frac{\lambda}{2} + 1 \right) \left( \frac{h_c}{h_i} \right)^\lambda + \left( \frac{h_c}{h_d} \right)^\lambda \right] \left[ \frac{1}{2} + \ln \left( \frac{h_d}{h_i} \right) \right]^{-1} \quad (2.15c)$$

and

$$c_2 = \left( \frac{h_c}{h_i} \right)^2 \left[ 1 - \left( \frac{h_c}{h_i} \right)^\lambda + \left( \frac{h_c}{h_d} \right)^\lambda - \frac{1 - \left( \frac{\lambda}{2} + 1 \right) \left( \frac{h_c}{h_i} \right)^\lambda + \left( \frac{h_c}{h_d} \right)^\lambda}{\frac{1}{2 \ln \left( \frac{h_d}{h_i} \right)} + 1} \right] \quad (2.15d)$$

A closed-form expression for the hydraulic conductivity does not exist for this function and the permitted values for  $\kappa$  are not physically acceptable.

Fayer and Simmons (1995) used the approach of Campbell and Shiozawa (1992) to have separate terms for adsorbed and capillary bound water. If the capillary binding is represented by a Brooks-Corey type function, the retention model becomes

$$\theta(h) = \begin{cases} 0, & h \leq h_d \\ \theta_a \left( 1 - \frac{\ln|h|}{\ln|h_d|} \right) + \left[ \theta_s - \theta_a \left( 1 - \frac{\ln|h|}{\ln|h_d|} \right) \right] \left( \frac{h_{ae}}{h} \right)^\lambda, & h_d < h < h_{ae} \\ \theta_s, & h \geq h_{ae} \end{cases} \quad (2.16a)$$

This expression is denoted FSB below. The derivative is

$$\frac{d\theta}{dh} = \begin{cases} 0, & h \leq h_d \\ \frac{1}{|h|} \left( \frac{h_{ae}}{h} \right)^\lambda \left[ \lambda(\theta_s - \theta_a) + \theta_a \left( \frac{\ln|h|}{\ln|h_d|} - \frac{1}{\ln|h_d|} \right) \right], & h_d < h < h_{ae} \\ 0, & h \geq h_{ae} \end{cases} \quad (2.16b)$$



The corresponding conductivity model is

$$K(h) = \begin{cases} 0, & h \leq h_d \\ K_s S_e^\tau \left\{ \frac{\left[ \frac{|h_{ae}|^\lambda}{\ln|h_d|(\lambda + \kappa)} \left[ \theta_a \left( \frac{\lambda + \kappa - 1}{\lambda + \kappa} - \ln|h| \right) - \lambda(\theta_s - \theta_a) \ln|h_d| \right] |h|^{-\lambda - \kappa} \right]_{h_d}^h}{\left[ \frac{|h_{ae}|^\lambda}{\ln|h_d|(\lambda + \kappa)} \left[ \theta_a \left( \frac{\lambda + \kappa - 1}{\lambda + \kappa} - \ln|h| \right) - \lambda(\theta_s - \theta_a) \ln|h_d| \right] |h|^{-\lambda - \kappa} \right]_{h_d}^{h_{ae}}} \right\}^\gamma, & h_d < h \leq h_{ae} \\ K_s, & h \geq h_{ae} \end{cases} \quad (2.16c)$$

$$= K_s \left\{ \frac{\theta_a \left( 1 - \frac{\ln|h|}{\ln|h_d|} \right)}{\theta_s \left( 1 - \frac{\ln|h|}{\ln|h_d|} \right)} + \left[ 1 - \frac{\theta_a \left( 1 - \frac{\ln|h|}{\ln|h_d|} \right)}{\theta_s \left( 1 - \frac{\ln|h|}{\ln|h_d|} \right)} \right] \left( \frac{h_{ae}}{h} \right)^\lambda \right\}^\tau$$

$$\left\{ \frac{[\theta_a(G - \ln|h|) - I] |h|^{-\lambda - \kappa} - J}{[\theta_a(G - \ln|h_{ae}|) - I] |h_{ae}|^{-\lambda - \kappa} - J} \right\}^\gamma,$$

where

$$G = \frac{\lambda + \kappa - 1}{\lambda + \kappa} \quad (2.16d)$$

$$I = \lambda(\theta_s - \theta_a) \ln|h_d| \quad (2.16e)$$

$$J = [\theta_a(G - \ln|h_d|) - I] |h_d|^{-\lambda - \kappa} \quad (2.16f)$$

Note that the above model is valid if  $h_{ae}$  does not exceed -1 cm. This condition will usually be met, unless the soil texture is very coarse.

If capillary binding is described by a van Genuchten function, the resulting equation is

$$\theta(h) = \begin{cases} 0, & h \leq h_d \\ \theta_a \left[ 1 - \frac{\ln|h|}{\ln|h_d|} \right] + \left\{ \theta_s - \theta_a \left[ 1 - \frac{\ln|h|}{\ln|h_d|} \right] \right\} \left[ 1 + (-\alpha h)^n \right]^{\frac{1}{n} - 1}, & h_d < h < 0 \end{cases} \quad (2.17a)$$

with derivative

$$\frac{d\theta}{dh} = \begin{cases} 0, & h \leq h_d \\ \frac{\theta_a}{h \ln|h_d|} \left\{ \left[ 1 + (-\alpha h)^n \right]^{\frac{1}{n}-1} - 1 \right\} \\ + \alpha(1-n)(-\alpha h)^{n-1} \left[ 1 + (-\alpha h)^n \right]^{\frac{1}{n}-2} \left\{ \theta_a \left[ 1 - \frac{\ln|h|}{\ln|h_d|} \right] - \theta_s \right\}, & h_d < h < 0 \end{cases} \quad (2.17b)$$

The derivative has several terms that pose severe restrictions on the value of  $\kappa$  (the first term even requires that  $\kappa < -1$ ), and other terms that limit the permitted values of  $n$ . The conductivity function is therefore omitted here.

In the original equations of both versions as presented by Fayer and Simmons (1995), the adsorbed water content reached zero at  $h_d$ , while there is still some capillary bound water at and below that matric potential, which is inconsistent. Furthermore, the terms with ratios of logarithms become negative for matric potentials below  $h_d$ . We therefore modified the original equations by setting the water content to zero below  $h_d$ .

Kosugi (1996) and Kosugi (1999) presented a soil water retention curve for soils with a lognormal pore size distribution. Khlosi et al. (2008) extended the approach of Campbell and Schiozawa (1992) and Fayer and Simmons (1995) to Kosugi's (1996, 1999) model. We again set the water content to zero for matric potentials below  $h_d$ :

$$\theta(h) = \begin{cases} 0, & h \leq h_d \\ \theta_a \left( 1 - \frac{\ln|h|}{\ln|h_d|} \right) + \left[ \theta_s - \theta_a \left( 1 - \frac{\ln|h|}{\ln|h_d|} \right) \right] \frac{1}{2} \operatorname{erfc} \left[ \frac{\ln \left( \frac{h}{h_m} \right)}{\sigma \sqrt{2}} \right], & h_d < h < 0 \end{cases} \quad (2.18a)$$

with the derivative (see Olver et al., 2010, p. 163 and p. 443)

$$\frac{d\theta}{dh} = \begin{cases} 0, & h \leq h_d \\ \frac{\theta_a}{h \ln|h_d|} \left\{ \frac{1}{2} \operatorname{erfc} \left[ \frac{\ln \left( \frac{h}{h_m} \right)}{\sigma \sqrt{2}} \right] - 1 \right\} + \frac{\theta_a \left( 1 - \frac{\ln|h|}{\ln|h_d|} \right) - \theta_s}{h \sigma \sqrt{2\pi}} \exp \left\{ - \left[ \frac{\ln \left( \frac{h}{h_m} \right)}{\sigma \sqrt{2}} \right]^2 \right\}, & h_d < h < 0 \end{cases} \quad (2.18b)$$

Parameter  $h_m$  [L] represents the matric potential corresponding to the median pore size, and  $\sigma$  characterizes the width of the pore size distribution. The behavior of the derivative near saturation is not readily clear. Expressions for the corresponding hydraulic conductivity function can only be found for integer values of  $\kappa$ . For  $\kappa = 1$ , the expression for the hydraulic conductivity is

$$K(h) = \begin{cases} 0, & h \leq h_d \\ K_s S_e^\tau \left\{ \left[ \frac{\theta_a}{2\theta_s |h_m| \ln|h_d|} \left\{ e^{L^2} \operatorname{erf}(P(h) + L) + \frac{h_m}{h} [\operatorname{erfc}(P(h)) - 2] - \right. \right. \right. \\ \left. \left. \left. M_1 e^{L^2} \operatorname{erf}(P(h) + L) - \frac{2Lh_m}{h\sqrt{\pi}} e^{-P^2(h)} \right\} \right]_{h_d}^h \right\}^\gamma \\ \left[ \frac{\theta_a}{2\theta_s |h_m| \ln|h_d|} \left\{ e^{L^2} \operatorname{erf}(P(h) + L) + \frac{h_m}{h} [\operatorname{erfc}(P(h)) - 2] - \right. \right. \\ \left. \left. M_1 e^{L^2} \operatorname{erf}(P(h) + L) - \frac{2Lh_m}{h\sqrt{\pi}} e^{-P^2(h)} \right\} \right]_{h_d}^0 \right\} \\ = K_s S_e^\tau \left\{ \begin{aligned} & e^{L^2} [\operatorname{erf}(P(h) + L) - \operatorname{erf}(P(h_d) + L)] + \\ & h_m \left[ \frac{\operatorname{erfc}(P(h)) - 2}{h} - \frac{\operatorname{erfc}(P(h_d)) - 2}{h_d} \right] - \\ & M_1 e^{L^2} [\operatorname{erf}(P(h) + L) - \operatorname{erf}(P(h_d) + L)] - \\ & \frac{2Lh_m}{\sqrt{\pi}} \left( \frac{e^{-P^2(h)}}{h} - \frac{e^{-P^2(h_d)}}{h_d} \right) \\ & - e^{L^2} [1 + \operatorname{erf}(P(h_d) + L)] + \\ & h_m \left[ \frac{\operatorname{erfc}(P(0)) - 2}{0} - \frac{\operatorname{erfc}(P(h_d)) - 2}{h_d} \right] + \\ & M_1 e^{L^2} [1 + \operatorname{erf}(P(h_d) + L)] - \frac{2Lh_m}{\sqrt{\pi}} \left( \frac{e^{-P^2(0)}}{0} - \frac{e^{-P^2(h_d)}}{h_d} \right) \end{aligned} \right\}, \quad h_d < h \leq 0 \end{cases} \quad (2.18c)$$

where  $S_e$  is obtained by dividing Eq. (2.18a) by  $\theta_s$ . The following functions and derived variables have been used for clarity:

$$L = \frac{\sigma\sqrt{2}}{2} \quad (2.18d)$$

$$P(h) = \frac{\ln\left(\frac{h}{h_m}\right)}{\sigma\sqrt{2}} \quad (2.18e)$$

$$M_1 = \left(1 - \frac{\theta_s}{\theta_a}\right) \ln|h_d| - \ln|h_m| + \sigma^2 \quad (2.18f)$$

For  $\kappa = 2$ , the expression for the hydraulic conductivity reads:

$$K(h) = \begin{cases} 0, & h \leq h_d \\ K_s S_e^\tau \left\{ \left[ \frac{\theta_a}{2\theta_s h_m^2 \ln|h_d|} \left\{ \frac{e^{4L^2} \operatorname{erf}(P(h) + 2L)}{2} + \frac{1}{2} \left( \frac{h_m}{h} \right)^2 [\operatorname{erfc}(P(h)) - 2] - \right. \right. \right. \\ \left. \left. \left. M_2 e^{4L^2} \operatorname{erf}(P(h) + 2L) - \frac{2Lh_m^2}{h^2 \sqrt{\pi}} e^{-P^2(h)} \right\} \right]_{h_d}^h \right\}^\gamma, & \\ \\ K_s S_e^\tau \left\{ \left[ \frac{\theta_a}{2\theta_s h_m^2 \ln|h_d|} \left\{ \frac{e^{4L^2} \operatorname{erf}(P(h) + 2L)}{2} + \frac{1}{2} \left( \frac{h_m}{h} \right)^2 [\operatorname{erfc}(P(h)) - 2] - \right. \right. \right. \\ \left. \left. \left. M_2 e^{4L^2} \operatorname{erf}(P(h) + 2L) - \frac{2Lh_m^2}{h^2 \sqrt{\pi}} e^{-P^2(h)} \right\} \right]_{h_d}^0 \right\}^\gamma, & \\ \\ = K_s S_e^\tau \left\{ \left[ \frac{e^{4L^2}}{2} [\operatorname{erf}(P(h) + 2L) - \operatorname{erf}(P(h_d) + 2L)] + \right. \right. \\ \left. \frac{h_m^2}{2} \left[ \frac{\operatorname{erfc}(P(h)) - 2}{h^2} - \frac{\operatorname{erfc}(P(h_d)) - 2}{h_d^2} \right] - \right. \\ \left. M_2 e^{4L^2} [\operatorname{erf}(P(h) + 2L) - \operatorname{erf}(P(h_d) + 2L)] - \right. \\ \left. \frac{2Lh_m^2}{\sqrt{\pi}} \left( \frac{e^{-P^2(h)}}{h^2} - \frac{e^{-P^2(h_d)}}{h_d^2} \right) \right]_{h_d}^h \right\}^\gamma, & h_d < h \leq 0 \\ \\ = K_s S_e^\tau \left\{ \left[ -\frac{e^{4L^2}}{2} [1 + \operatorname{erf}(P(h_d) + 2L)] + \right. \right. \\ \left. \frac{h_m^2}{2} \left[ \frac{\operatorname{erfc}(P(0)) - 2}{0^2} - \frac{\operatorname{erfc}(P(h_d)) - 2}{h_d^2} \right] + \right. \\ \left. M_2 e^{4L^2} [1 + \operatorname{erf}(P(h_d) + 2L)] - \frac{2Lh_m^2}{\sqrt{\pi}} \left( \frac{e^{-P^2(0)}}{0^2} - \frac{e^{-P^2(h_d)}}{h_d^2} \right) \right]_{h_d}^0 \right\}^\gamma, & \end{cases} \quad (2.18g)$$

with

$$M_2 = \left( 1 - \frac{\theta_s}{\theta_a} \right) \ln|h_d| - \ln|h_m| + 2\sigma^2 \quad (2.18h)$$

There are several terms with zero in the denominator in Eqs. (2.18c) and (2.18g). In these terms, the numerator is zero as well. The terms  $\exp[P^{-2}(h)] \cdot h^{-1}$  and  $\exp[P^{-2}(h)] \cdot h^{-2}$  appearing in Eqs. (2.18c) and (2.18g) both become infinite for all physically acceptable values of  $h_m$  and  $\sigma$ . As a consequence, the unsaturated hydraulic conductivity for both values of  $\kappa$  suffers from the non-realistic increase near

saturation diagnosed by Ippisch et al. (2006) for van Genuchten's (1980) soil water retention model, and the use of Eqs. (2.18c-h) is not recommended.

Groenevelt and Grant (2004) proposed:

$$\theta(h) = \begin{cases} 0, & h \leq -10^{6.9} \text{ cm} \\ g_1 \left\{ \exp\left(\frac{-g_0}{6.9^\eta}\right) - \exp\left[\frac{-g_0}{(\log_{10}|h|)^\eta}\right] \right\}, & -10^{6.9} \leq h \leq -1 \text{ cm} \\ g_1 \exp\left(\frac{-g_0}{6.9^\eta}\right), & h \geq -1 \text{ cm} \end{cases} \quad (2.19a)$$

where  $g_0$ ,  $g_1$ , and  $\eta$  are fitting parameters. The constant water content for matric potentials larger than -1cm is imposed. Groenevelt and Grant (2004) proposed a more flexible curve-shifting approach, but that procedure is cumbersome to perform in a global search parameter fitting operation. The derivative is

$$\frac{d\theta}{dh} = \begin{cases} 0, & h \leq -10^{6.9} \text{ cm} \\ \frac{g_0 g_1 \eta [\ln(10)]^\eta}{|h| (\ln|h|)^{\eta+1}} \exp\left\{ \frac{-g_0 [\ln(10)]^\eta}{(\ln|h|)^\eta} \right\}, & -10^{6.9} \leq h \leq -1 \text{ cm} \\ 0, & h \geq -1 \text{ cm} \end{cases} \quad (2.19b)$$

This expression does not permit a closed-form expression for the hydraulic conductivity function.

Peters (2013) introduced four soil water retention models. He used a logarithmic model for adsorbed water that differed from that of Campbell and Shiozawa (1992) and the capillary model of either van Genuchten (1980) or Kosugi (1999). He developed versions for which the water content could be non-zero at the oven-dry matric potential  $h_d$ , which is incorrect but permits closed-form expressions of the hydraulic conductivity function. He also presented versions for which the water content is forced to be zero at  $h_d$ .

For the versions with nonzero water contents at  $h_d$ , the capillary bound and adsorbed water contents are added (Peters, 2013, Eq. (2)):

$$S_e(h) = w S^{cap}(h) + (1-w) S^{ad}(h) \quad (2.20)$$

where the superscripts *cap*, and *ad* reflect capillary bound and adsorbed water, respectively, and  $w$  is a weighting factor ranging between 0 and 1. The van Genuchten-version with non-zero water content at  $h_d$  is

$$\theta(h) = \begin{cases} \theta_s w \left[ 1 + (-\alpha h)^n \right]^{\frac{1}{n}-1} + \theta_s (1-w) \frac{1 - \frac{\ln\left(1 + \frac{h}{h_a}\right)}{\ln\left(1 + \frac{h_d}{h_a}\right)}}{1 - \frac{\ln(2)}{\ln\left(1 + \frac{h_d}{h_a}\right)}}, & h_d \leq h \leq h_a \\ \theta_s w \left[ 1 + (-\alpha h)^n \right]^{\frac{1}{n}-1} + \theta_s (1-w), & 0 \geq h \geq h_a \end{cases} \quad (2.21a)$$

with derivative

$$\frac{d\theta}{dh} = \begin{cases} -\theta_s w \alpha (1-n) (-\alpha h)^{n-1} \left[ 1 + (-\alpha h)^n \right]^{\frac{1}{n}-2} + \frac{\theta_s (1-w)}{h+h_a} \frac{1}{\ln\left(1 + \frac{h_d}{h_a}\right) - \ln(2)}, & h \leq h_a \\ -\theta_s w \alpha (1-n) (-\alpha h)^{n-1} \left[ 1 + (-\alpha h)^n \right]^{\frac{1}{n}-2}, & 0 \geq h \geq h_a \end{cases} \quad (2.21b)$$

The parameter  $h_a$  [L] represents the matric potential at which the soil reaches the maximum adsorbed water content.

The Kosugi-version with non-zero water content at air-dryness is:

$$\theta(h) = \begin{cases} \frac{\theta_s w}{2} \operatorname{erfc} \left[ \frac{\ln\left(\frac{h}{h_m}\right)}{\sigma\sqrt{2}} \right] + \theta_s (1-w) \frac{1 - \frac{\ln\left(1 + \frac{h}{h_a}\right)}{\ln\left(1 + \frac{h_d}{h_a}\right)}}{1 - \frac{\ln(2)}{\ln\left(1 + \frac{h_d}{h_a}\right)}}, & h_d \leq h \leq h_a \\ \frac{\theta_s w}{2} \operatorname{erfc} \left[ \frac{\ln\left(\frac{h}{h_m}\right)}{\sigma\sqrt{2}} \right] + \theta_s (1-w), & 0 \geq h \geq h_a \end{cases} \quad (2.22a)$$

with derivative

$$\frac{d\theta}{dh} = \begin{cases} -\frac{\theta_s w}{h\sigma\sqrt{2\pi}} \exp\left\{-\left[\frac{\ln\left(\frac{h}{h_m}\right)}{\sigma\sqrt{2}}\right]^2\right\} + \frac{\theta_s(1-w)}{h+h_a} \frac{1}{\ln\left(1+\frac{h_d}{h_a}\right) - \ln(2)}, & h \leq h_a \\ -\frac{\theta_s w}{h\sigma\sqrt{2\pi}} \exp\left\{-\left[\frac{\ln\left(\frac{h}{h_m}\right)}{\sigma\sqrt{2}}\right]^2\right\}, & 0 \geq h \geq h_a \end{cases} \quad (2.22b)$$

The van Genuchten-version with zero water content when the soil is air dry is

$$\theta(h) = \begin{cases} 0, & h \leq h_d \\ \theta_s \left( w \left\{ \left[ 1 + (-\alpha h)^n \right]^{\frac{1}{n}-1} - 1 \right\} + 1 \right) \frac{1 - \frac{\ln\left(1+\frac{h}{h_a}\right)}{\ln\left(1+\frac{h_d}{h_a}\right)}}{1 - \frac{\ln(2)}{\ln\left(1+\frac{h_d}{h_a}\right)}}, & h_d \leq h \leq h_a \\ \theta_s w \left[ 1 + (-\alpha h)^n \right]^{\frac{1}{n}-1} + \theta_s(1-w), & 0 \geq h \geq h_a \end{cases} \quad (2.23a)$$

with derivative

$$\frac{d\theta}{dh} = \begin{cases} 0, & h \leq h_d \\ -\theta_s w \alpha (1-n) (-\alpha h)^{n-1} \left[1 + (-\alpha h)^n\right]^{\frac{1}{n}-2} \frac{1 - \frac{\ln\left(1 + \frac{h}{h_a}\right)}{\ln\left(1 + \frac{h_d}{h_a}\right)}}{1 - \frac{\ln(2)}{\ln\left(1 + \frac{h_d}{h_a}\right)}}, & h \leq h_a \\ \theta_s \left( w \left\{ \left[1 + (-\alpha h)^n\right]^{\frac{1}{n}-1} - 1 \right\} + 1 \right) + \frac{\theta_s \left( w \left\{ \left[1 + (-\alpha h)^n\right]^{\frac{1}{n}-1} - 1 \right\} + 1 \right)}{(h + h_a) \left[ \ln\left(1 + \frac{h_d}{h_a}\right) - \ln(2) \right]}, & h \leq h_a \\ -\theta_s w \alpha (1-n) (-\alpha h)^{n-1} \left[1 + (-\alpha h)^n\right]^{\frac{1}{n}-2}, & 0 \geq h \geq h_a \end{cases} \quad (2.23b)$$

The Kosugi-version with zero water content at  $h_d$  is

$$\theta(h) = \begin{cases} 0, & h \leq h_d \\ \theta_s \left( w \left\{ \frac{1}{2} \operatorname{erfc} \left[ \frac{\ln\left(\frac{h}{h_m}\right)}{\sigma\sqrt{2}} \right] - 1 \right\} + 1 \right) \frac{1 - \frac{\ln\left(1 + \frac{h}{h_a}\right)}{\ln\left(1 + \frac{h_d}{h_a}\right)}}{1 - \frac{\ln(2)}{\ln\left(1 + \frac{h_d}{h_a}\right)}}, & h_d \leq h \leq h_a \\ \frac{\theta_s w}{2} \operatorname{erfc} \left[ \frac{\ln\left(\frac{h}{h_m}\right)}{\sigma\sqrt{2}} \right] + \theta_s (1-w), & 0 \geq h \geq h_a \end{cases} \quad (2.24a)$$

with derivative



$$\frac{d\theta}{dh} = \begin{cases} 0, & h \leq h_d \\ -\frac{\theta_s w}{h\sigma\sqrt{2\pi}} \exp\left\{-\left[\frac{\ln\left(\frac{h}{h_m}\right)}{\sigma\sqrt{2}}\right]^2\right\} \frac{1 - \frac{\ln\left(1 + \frac{h}{h_a}\right)}{\ln\left(1 + \frac{h_d}{h_a}\right)}}{1 - \frac{\ln(2)}{\ln\left(1 + \frac{h_d}{h_a}\right)}}, & h \leq h_a \\ + \left( w \left[ \frac{1}{2} \operatorname{erfc}\left[\frac{\ln\left(\frac{h}{h_m}\right)}{\sigma\sqrt{2}}\right] - 1 \right] + 1 \right) \frac{\theta_s}{(h + h_a) \left[ \ln\left(1 + \frac{h_d}{h_a}\right) - \ln(2) \right]}, & h \leq h_a \\ -\frac{\theta_s w}{h\sigma\sqrt{2\pi}} \exp\left\{-\left[\frac{\ln\left(\frac{h}{h_m}\right)}{\sigma\sqrt{2}}\right]^2\right\}, & 0 \geq h \geq h_a \end{cases} \quad (2.24b)$$

Both water retention functions based on van Genuchten's (1980) model (Eqs. (2.21a) and (2.23a)) lead to the requirement that  $\kappa$  be smaller than  $n - 1$  (see Eq. (2.9)) and therefore do only have a physically acceptable conductivity curve associated with them for a very limited range of  $\kappa$ . The Kosugi-based versions (Eqs. (2.22a) and (2.24a)) suffer from the same lack of clarity about the behavior of the derivative as Khlosi et al.'s (2008) modified Kosugi function and require integer values of  $\kappa$ . Because of these limitations and the unwieldy nature of the equations (compare Eqs. (2.18c-h)), their practical value seems limited.

Iden and Durner (2014) proposed modifications of Peters' (2013) models that permitted an analytical expression for the conductivity function even if the water content was forced to be zero at  $h_d$ . To apply the criterion of Eq. (2.4) to this modification, we multiply the derivative of their retention curve (their Eq. (3)) for adsorbed water by  $h^{-\kappa}$ :

$$\theta_s |h|^{-\kappa} \frac{dS^{ad}}{dh} = \frac{\theta_s |h|^{-\kappa-1}}{\ln(10)(\log|h_a| - \log|h_d|)} \left[ 1 - \frac{\exp\left(\frac{\log|h_a| - \log|h|}{b}\right)}{1 + \exp\left(\frac{\log|h_a| - \log|h|}{b}\right)} \right] \quad (2.25)$$

where  $b$  is a shape parameter. High values of  $b$  lead to a sharp transition between the two linear segments in the semi-logarithmic form of the adsorbed water retention curve with different slopes. Iden and Durner recommend values of  $b$  between 0.1 and 0.3. In the limit as  $h$  approaches zero, Eq. (2.25) simplifies to

$$\lim_{h \rightarrow 0} \left( \theta_s |h|^{-\kappa} \frac{dS^{ad}}{dh} \right) = \frac{\theta_s |h|^{-\kappa-1}}{\ln(10)(\log|h_a| - \log|h_d|)} \left[ 1 - \frac{\exp\left(\frac{-\log|h|}{b}\right)}{1 + \exp\left(\frac{-\log|h|}{b}\right)} \right] \quad (2.26)$$

The approximation in the last term leads to the requirement that  $\kappa < -1$  for the limit to go to zero for any value of  $b$ , but small values of  $b$  allow larger ranges of  $\kappa$ . For  $b = 0.3$ , trial calculations showed that the value in the limit appears to be zero for  $\kappa < 0.2$ , which still rules out the established conductivity models. For  $b = 0.1$ , the limit is zero even for large positive values of  $\kappa$ . It might be recommendable to fix  $b$  at 0.1 instead of treating it as a fitting parameter.

The scaling of the capillary soil water retention curves proposed by Iden and Durner (2014) does not alleviate the problems with the van Genuchten curve near saturation while the Kosugi-function remains unwieldy. Conductivity functions for Peters' (2013) retention models will therefore not be derived.

In summary, many of the retention curves examined result in conductivity curves with physically unacceptable behavior near saturation, even though several of these expressions were derived with the explicit purpose of providing closed-form expressions for the hydraulic conductivity. Only the Brooks-Corey function (1964) (BCO, Eq. (2.5a)), the junction model of Rossi and Nimmo (1994) without the parabolic correction (RNA, Eq. (2.13a)), and the model of Fayer and Simmons (1995) based on the Brooks-Corey (1964) retention function (FSB, Eq. (2.16a)) lead to an acceptable conductivity model with full flexibility (three free parameters:  $\kappa$ ,  $\gamma$ ,  $\tau$ ). The modified van Genuchten (1980) retention curve with a distinct air-entry value by Ippisch et al. (2006) (VGA, Eq. (2.11a)) leads to a conductivity model with two fitting parameters if  $m = 1 - 1/n$  because  $\kappa = 1$ .

## 2.3. Materials and methods

### 2.3.1. Soil water retention and hydraulic conductivity data

Data were obtained from Schelle et al. (2013) who measured soil water retention curves for a range of soil textures (clay, silt, silt loam, and sand). They took undisturbed and disturbed samples of a silt loam, a silt, and a sand near Braunschweig (northern Germany), and of a clay near Munich (southern Germany). The retention data were measured on soil samples using different laboratory methods and cover the moisture range from saturation to near oven dryness at pF approximately 7. For silt, silt loam and sand they used data obtained by suction plates, pressure plates and the dew point method. For clay they used HYPROP<sup>®</sup> (UMS, 2015) (until pF 3), pressure plate and drying dew point methods. Here, we trimmed the disproportionately large data set in the HYPROP<sup>®</sup> range by stratifying the data into intervals of 0.5 on the pF scale and then randomly picking one data point for each interval. This ensured an adequate sensitivity of the fit in the dry range for all textures. For some of the soil samples, hydraulic conductivity data were available, including the values at saturation (unpublished). Hydraulic conductivity data were obtained by the evaporation method according to Peters and Durner (2008).

Undisturbed samples of 4.0 cm height and 100 cm<sup>3</sup> volume were used for the suction plate method, with 4 to 6 replicates for each soil. The HYPROP® setup worked with an undisturbed sample of 5.0 cm height and 250 cm<sup>3</sup> volume (one replicate). The pressure plate method required disturbed samples of 1.0 cm height and 5.2 cm<sup>3</sup> volume (5 or 6 replicates for each soil). The dew point method worked with disturbed samples of approximately 10 g dry mass (7 to 24 replicates with pF values between 3.5 and 6.2). Additional details are given by Schelle et al. (2013).

The fitting routine uses the variance of the data error to determine the weighting factor each data point. We estimated these on the basis of estimated measurement errors of water level readings, pressure gauges, sample masses, etc.

When the three conductivity parameters are set to the values dictated by Burdine (1953), Mualem (1976), or Alexander and Skaggs (1986), hydraulic conductivity curves can be derived from soil water retention data only, supplemented by an estimate for the saturated hydraulic conductivity. For the soils with available conductivity data we compared the hydraulic conductivity curves to the direct measurements.

## 2.3.2. Parameter fitting

### 2.3.2.1. Selected parameterizations

We fitted the original Brooks-Corey (BCO, Eq. 2.5a) and van Genuchten (VGN, Eq. 2.8a) parameterizations, and the derivatives thereof that do not lead to unrealistic hydraulic conductivities near saturation: FSB (Eq. 2.16a) and RNA (Eq. 2.13 a), both of which emerged from BCO, and VGA (Eq. 2.11a), which emerged from VGN. Thus, BCO (Eq. 2.5a), FSB (Eq. 2.16a), and RNA (Eq. 2.13a) all have a power law shape in the mid-range of the matric potential (and for BCO over the full range below the air-entry value). The slope therefore monotonically increases with decreasing water content. VGN (Eq. 2.8a) and VGA (Eq. 2.11a) have a sigmoid shape and therefore are able to fit curves that have an inflection point. As Groenevelt and Grant (2004) pointed out,  $\theta_r$  serves as the third required shape parameter for curves with an inflection point, frequently resulting in improbable values for this parameter. Table 2.1 shows the fitting parameters and their physically permitted range.

All three conductivity models are compatible with BCO, FSB and RNA. Burdine's (1953) and Mualem's (1976) conductivity models can be used with VGA. VGN only works with Mualem's conductivity model (1976). Note that VGN leads to an unrealistically rapid increase of the conductivity near saturation. It was included for comparison, because it is the most widely used parameterization at the moment.

### 2.3.2.2. The objective function and its weighting factors

A set of parameters describing the soil water retention curve must be optimized to provide the best fit to an arbitrary number of data points. To do so, an objective function was minimized, construed by the sum of weighted squares of the differences between observed and fitted values. The fitted values depend on the parameter values in the parameter vector  $\mathbf{x}$ . Assume  $q_\theta$  observation pairs of water content vs. matric head  $(h_i, \theta_i)$ . Here,  $\theta_i$  denotes the  $i$ th observation of the volumetric water content,  $h_i$  [L] is the matric head at which that water content was observed (expressed as an equivalent water column), and  $i \in \{1, 2, \dots, q_\theta\}$  is a counter. In the code, the assumed units are cm water column for  $h$  and cm<sup>3</sup> cm<sup>-3</sup> for  $\theta$ .

The definition of the objective function  $F_R(\mathbf{x}_{p,R})$  at the  $R^{\text{th}}$  iteration during the fitting operation is:

$$F_R(\mathbf{x}_{p,R}) = \mathbf{w}_{\theta,R}^T \mathbf{d}_{\theta}(\mathbf{x}_{p,R}, \mathbf{x}_f) \quad R \in \{1, 2, \dots, R_{\max}\} \quad (2.27)$$

Here,  $\mathbf{d}_{\theta}$  denotes a vector of length  $q_{\theta}$  of squared differences between observations and fits that are functions of the fitted parameter values  $\mathbf{x}_p$  and the fixed (non-fitted) parameters in vector  $\mathbf{x}_f$ . Together,  $\mathbf{x}_p$  and  $\mathbf{x}_f$  constitute  $\mathbf{x}$ . Each squared difference is weighted. The weight factor vector is denoted by  $\mathbf{w}_{\theta,R}$ . Its dependence on the water content and iteration step is explained below. The superscript T indicates that the vector is transposed. To terminate infinite loops, the number of iterations is capped by  $R_{\max}$ .

For relatively wet soils ( $0 > h > -100$  to  $-200$  cm), measurement methods are available that create a hydrostatic equilibrium in a relatively large sample. In such cases  $h_i$  reflects the matric potential at the center of the sample but  $\theta_i$  is that determined for the entire sample. The vertical variation of  $h$  results in a non-uniform water content, and the average water content of the sample ( $\theta_i$ ) may not be well represented by the water content corresponding to  $h_i$ . For these cases, the height of the sample can be specified on input. The code then divides the sample into 20 layers, calculates  $h$  in the center of each layer, computes the corresponding water contents from  $\mathbf{x}_{p,R}$ , and averages these to arrive at an estimate of  $\theta_i$ .

If and only if the standard deviation of the measurement error of the individual observations is known, a maximum-likelihood estimate of the soil hydraulic parameters can be obtained (Hollenbeck and Jensen, 1998). To ensure this, the weighting factors in vector  $\mathbf{w}_{\theta,R}$  must be equal to the reciprocal of the variance of the measurement error. Note that this choice eliminates any effect of measurement units because the squared differences have the same units as the variances by which they are divided (Hollenbeck and Jensen, 1998). Only then can model adequacy be examined. A model is considered adequate if the residuals after parameter fitting are solely caused by measurement noise (Hollenbeck et al., 2000). Furthermore, only if these conditions are met can confidence intervals of fitted parameters be determined (Hollenbeck and Jensen, 1998). Even in that case, the contouring of the parameter space for permissible increases of the objective function required to determine the confidence region is not practically feasible for four or more parameters, and very laborious even for fewer parameters. A popular approximation based on the Cramer-Rao theorem was shown to be rather poor by Hollenbeck and Jensen (1998), so we refrained from implementing it. Instead we record the evolution of the parameter values through the iterative process. Low information content (indicated by large random fluctuations of a parameter value), correlated parameters, and parameters trending towards a minimum or maximum permitted value can usually be diagnosed from such records.

Data points for a retention curve over the whole moisture range cannot be obtained by a single method. Furthermore, measurement errors occur in both  $h_i$  and  $\theta_i$ . To accommodate this, the error standard deviations  $\sigma_{h,i}$  and  $\sigma_{\theta,i}$  for  $h$  and  $\theta$ , respectively can be provided individually for any data point  $i$ . To improve the performance of the fitting routine, the values of  $\sigma_{\theta,i}$  are scaled to ensure their average equals 0.20, i.e., the same order of magnitude as  $\theta$ . The values of  $\sigma_{h,i}$  are then scaled by the same scaling factor. The weighting factor  $w_{R,i}$  for observation  $\theta_i$  during iteration  $R$  is:

$$w_{R,i} = \sigma_{i,R}^{*-2} = \left( \sigma_{h,i}^* \frac{d\theta}{dh} \Big|_{R,i} + \sigma_{\theta,i}^* \right)^{-2} \quad (2.28)$$

where the asterisk denotes a scaled value. The subscripts  $i$  and  $R$  label data points and iteration steps as above. The gradient is determined from the  $R^{\text{th}}$  fitted  $\theta(h)$  relationship defined by  $\mathbf{x}_{p,R}$ . Thus, the weighting factors are updated for every iteration.

In the code, the gradient is approximated by  $\Delta\theta/\Delta h$  computed from the water contents at  $h_i \pm \max(1 \text{ cm H}_2\text{O}, 0.01 \cdot h_i)$ . For data points acquired at hydrostatic equilibrium, this would require 40 additional calls to the function that computes the  $\theta$  corresponding to a given value of  $h$ , which would be rather inefficient. Instead, the water content is calculated for one virtual layer below and one above the sample. By subtracting the water content of the top (bottom) layer in the sample and adding the water content of the virtual layer below (above) the sample, the water content corresponding to  $h_i + H/20$  ( $h_i - H/20$ ) can be found, with  $H$  the sample height in cm. In this way,  $\Delta\theta/\Delta h$  can be computed with only two additional calls to the function that defines the parameterized  $\theta(h)$  relationship.

### 2.3.2.3. Parameter optimization by Shuffled Complex Evolution

The calibration algorithm employed here is the Shuffled Complex Evolution (SCE) algorithm introduced by Duan et al. (1992) with parameter adjustments of Behrangi et al. (2008). The strategy of this algorithm is to form out of  $j + 1$  parameter sets, where  $j$  is the number of model parameters, so-called complexes (e.g. triangles in 2D). Each vertex of the complex not only represents one of the  $j + 1$  parameter sets but also the model's skill  $F_R(\mathbf{x}_{p,R})$  to match the observed data when it is forced with the according parameter set  $\mathbf{x}_{p,R}$ . This skill is usually referred to be the objective function value of an objective to be minimized. The vertex with the worst skill or largest objective function value is subsequently perturbed in order to find a better substitute parameter set. This strategy is repeated until the volume of the complex, i.e. the agreement of the parameter sets, is smaller than a threshold. To avoid that the search gets stuck in a local optimum, a number of  $Y$  complexes are acting in parallel. After a certain number of iterations the  $Y \cdot (j + 1)$  vertexes are shuffled and newly assigned to  $Y$  complexes. The algorithm converges when the volume of all complexes is lower than a threshold which means that all  $Y \cdot (j + 1)$  vertexes are in close proximity to each other. Infinite runs of the SCE are avoided by  $R_{\text{max}}$ , but convergence should be the desired target for termination of the SCE.

The SCE algorithm used here is configured with two complexes each consisting of  $(2j + 1)$  ensemble members. The different parameterizations we fitted had 3 to 5 fitting parameters. In each iteration,  $j + 1$  parameters are randomly selected and the vertex with the worst skill is perturbed. The reflection and contraction step lengths in the Simplex method (e.g., Press et al., 1992, p. 402-404) were set to 0.8 and 0.45, respectively. SCE seems to have an order of about  $O(j^2)$ . In our case it required between 280 and 1735 model evaluations to find the optimal parameter set. For each parameter estimation run, three sets of initial guesses of the fitting parameters must be provided. The results of the three trials were compared to reduce the chance of accepting a local minimum of the objective function. The selection of SCE was based on its widespread usage in hydrological studies and according to a preliminary experiment where the SCE outperformed other algorithms like the Simulated Annealing (Kirkpatrick et al, 1983) and the Dynamically Dimensioned Search algorithm (Tolson et al., 2007) in optimizing more than 80 analytical test functions with  $j$  ranging from 2 to 30.

### 2.3.3. Scenario study by numerical simulations

As stated in the Introduction, previous tests of parametric expressions of soil water retention functions mostly focused on the quality of the fit to direct observations of points on the water retention curve. Here, we will also examine how the various parameterizations affect the solution of Richards' equation by simulating water fluxes and soil water profiles for a scenario involving infiltration and evaporation. We set up a hypothetical 999-day scenario representative of a desert climate with prolonged drying, infiltration into dry soil, and redistribution after rainfall, permitting a comprehensive test of the parameterizations. We used the HYDRUS-1D model version 4.16.0090 (Šimůnek et al., 2013, <http://www.pc-progress.com/en/Default.aspx?hydrus-1d>) to solve Richards' equation in a 1-dimensional soil profile. We permitted flow of liquid water as well as diffusive water vapor fluxes.

We considered an unvegetated uniform soil profile of 1 m depth, initially in hydrostatic equilibrium with -400 cm matric potential at the soil surface. The upper boundary conditions were atmospheric (during dry periods: prescribed matric potential set to -50000 cm; during rain: prescribed flux density equal to the daily rainfall rate derived from observed daily sums). At the bottom of the profile, free drainage was assumed. The weather data (daily rainfall and temperature) were taken from the NOAA data base (<http://www.ncdc.noaa.gov/cdo-web/>) for a station in Riyadh city (Saudi Arabia) between June 4, 1993 and February 27, 1996. In this period spanning nearly three years, there were three clusters of rainfall events (Figure 2.1). The second cluster was the heaviest with a maximum daily sum of approximately 5.4 cm at the day 656. A prolonged dry spell preceded the first rainfall cluster. A prolonged dry spell preceded the first rainfall cluster. We used the first 250 days of this period as a 'burn-in' period to minimize the effect of the initial condition on the calculated fluxes. This leaves a period of 751 days for analysis.

The simulation period involved large hydraulic gradients when water infiltrated a very dry soil, limited infiltration of small showers followed by complete removal of all water, deeper infiltration after clusters of rainfall that delivered large amounts of water followed by prolonged periods in which flow of liquid water and water vapor occurred simultaneously. These processes combined permitted a comprehensive comparison of the various parameterizations. We were interested in the magnitude of the fluxes of liquid water and water vapor under various conditions, and the effect on these fluxes of the choice of parameterization. We did not intend or desire to carry out a water balance study. Under semi-arid conditions this would have required a much longer meteorological record, which was not available.

The various parameterizations are not implemented in HYDRUS. We therefore used the MATER.IN input file to supply the soil hydraulic property curves in tabular form to the model. The retention models BCO, FSB, and RNA permitted all three conductivity models (Burdine, Mualem and Alexander and Skaggs) to be used. VGA only gives useful expressions for Burdine and Mualem. VGN only allows Mualem's conductivity model. Thus, there are 12 combinations of retention and conductivity curves that we tested on four different textures, leading to 48 different simulations (and MATER.IN files) in total.

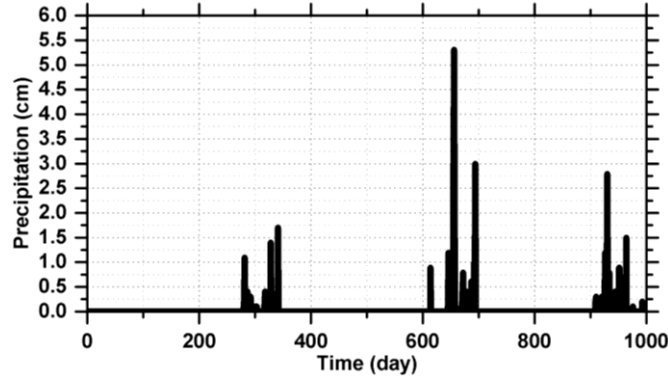


Figure 2.1: The record of daily rainfall sums from Riyadh city that was used in the numerical scenario study. Three rainfall clusters are visible. The largest daily rainfall amount (5.4 cm) fell on day 656. The observation period starts at June 4, 1993, and ends at February 27, 1996

## 2.4. Results and discussion

### 2.4.1. Fitted parameters and quality of the fits

Table 2.1 presents the fitted parameters for all combinations of texture and parameterization. The parameter with the best-defined physical meaning is  $\theta_s$ . All parameterizations give comparable values for it for each texture, which reflects the relatively narrow data clouds near saturation. The values of  $\theta_r$  are relatively high for the three parameterizations in which it occurs. The air-entry values ( $h_{ae}$ ) should increase (move closer to zero) from clay to silt loam to silt to sand, which is the case for BCO, FSB, and RNA, but not for VGA. The data in Figure 2.2 support relatively similar values for all textures other than clay, which is somewhat surprising. RNA gives rather high values in silt and sand, and VGA does very poorly in sand and silt loam. The high value for  $h_{ae}$  for FSB in clay may be related somehow to the very high value of the maximum adsorbed water content  $\theta_a$ , which we fixed close to  $\theta_s$ . The value of  $\theta_a$  for clay should be larger than that for silt loam, so it cannot be more than about 0.2 off though. The spread of  $h_j$  for RNA across the textures show that this parameter needs to be given the full range (between  $h_d$  and at least the minimum value of  $h_{ae}$ ). Even with initial guesses that differed by several orders of magnitude, the fits were still quite consistent, so evidently these values are supported by the data and not an artefact.

In three of the 48 parameter estimation runs, the fits pushed one of the parameters to one of its bounds (even after expanding these to their physical limits), irrespective of their initial guess: FSB for clay (we fixed  $\theta_a$  to 0.5), VGN for sand and RNA for silt (we fixed  $\theta_s$  on the basis of the data in both cases). For BCO and VGA in sandy soil, the code could not converge to a global minimum, indicated by the volume of the complexes, which exceeded the threshold. The fitted parameters should be viewed critically in these two cases.

The Root Mean Square Error (RMSE) of the fits (Table 2.2) illustrate why VGN has been very popular for over three decades. It gives the best fit in three cases (sand, silt and silt loam) and the second-best fit in the fourth (clay). BCO performs poorest in three cases (sand, silt and silt loam) and second-poorest in one (clay). The other three have varying positions, with no clearly strong or weak performers. FSB has the best performance in the finest soil (clay). The overall difference in the RMSE values between textures reflects the different scatter in the underlying data clouds.

Table 2.1: The fitting parameters for five parameterizations, their physically permitted ranges, and their fitted values for four textures. The three-character parameterization label is explained in the main text. The equations to which these labels refer are given in the first column.

Parameter -ization	Fitted parameter	Unit	Range	Texture			
				Silt	Sand	Clay	Silt loam
BCO Eq. (2.5a)	$\theta_r$	-	$0 - \theta_s$	0.000127	0.013300	0.000004	0.000015
	$\theta_s$	-	$\theta_r - 1$	0.445	0.366	0.516	0.358
	$h_{ae}$	cm	$-\infty - 0$	-21.426	-7.161	-50.577	-30.440
	$\lambda$	-	$0 - \infty$	0.197	0.520	0.091	0.163
FSB Eq. (2.16a)	$\theta_s$	-	$\theta_a - 1$	0.449	0.366	0.519	0.358
	$\theta_a$	-	$0 - \theta_s$	0.177	0.048	0.500	0.312
	$h_{ae}$	cm	$h_d - 0$	-11.537	-11.508	-16.783	-11.668
	$\lambda$	-	$0 - \infty$	0.254	0.719	0.152	0.364
RNA Eq. (2.13a)	$\theta_s$	-	$0 - 1$	0.460	0.382	0.522	0.358
	$h_{ae}$	cm	$h_j - 0$	-2.826	-1.884	-50.856	-30.250
	$h_j$	cm	$h_d - h_{ae}$	-2876	-359000	-49.882	-11641
VGA Eq. (2.11a)	$\theta_r$	-	$0 - \theta_s$	0.000133	0.012880	0.000019	0.000041
	$\theta_s$	-	$\theta_r - 1$	0.461	0.366	0.514	0.358
	$\alpha$	cm <sup>-1</sup>	$0 - \infty$	0.0197	0.8391	0.0055	0.0093
	$n$	-	$1 - \infty$	1.252	1.511	1.127	1.219
	$h_{ae}$	cm	$-\infty - 0$	-0.0015	-6.4626	-47.2530	-0.0081
VGN Eq. (2.8a)	$\theta_r$	-	$0 - \theta_s$	0.000025	0.013560	0.001160	0.000003
	$\theta_s$	-	$\theta_r - 1$	0.461	0.370	0.509	0.360
	$\alpha$	cm <sup>-1</sup>	$0 - \infty$	0.0200	0.1353	0.0042	0.0095
	$n$	-	$1 - \infty$	1.251	1.528	1.127	1.219

Table 2.2: Root mean square of errors (RMSE) for the different parameterizations.

Parameterization	Texture			
	Silt	Sand	Clay	Silt loam
BCO	0.1422	0.1164	0.1858	0.1122
FSB	0.1248	0.1163	0.1205	0.1068
RNA	0.0341	0.0130	0.2192	0.1101
VGA	0.0118	0.1164	0.1604	0.0412
VGN	0.0118	0.0111	0.1547	0.0411



The soil water retention curves defined by the different pits are plotted in (Figure 2.2). The models that were not developed with dry conditions in mind (BCO, VGA and VGN) have relatively high water contents in the dry end of clay and silt loam. The logarithmic dry end of FSB and RNA eliminates this asymptotic behavior. The cutoff to zero of the FSB parameterization is quite strong in fine-textured soils. The fixed value of  $h_d$  (where the water content is zero) of RNA seems to be too small for clay while appearing adequate for the other textures.

In the intermediate range, all fits are close to one another. RNA underperforms in sand and silt compared to the others. In the wet range, the absence of an air-entry value in VGN results in a poor fit for sand. Here, the contrast between VGN and VGA is very clear. Overall, the inclusion of the water-entry value as a parameter seems beneficial to the fits. FSB has the most satisfactory overall performance.

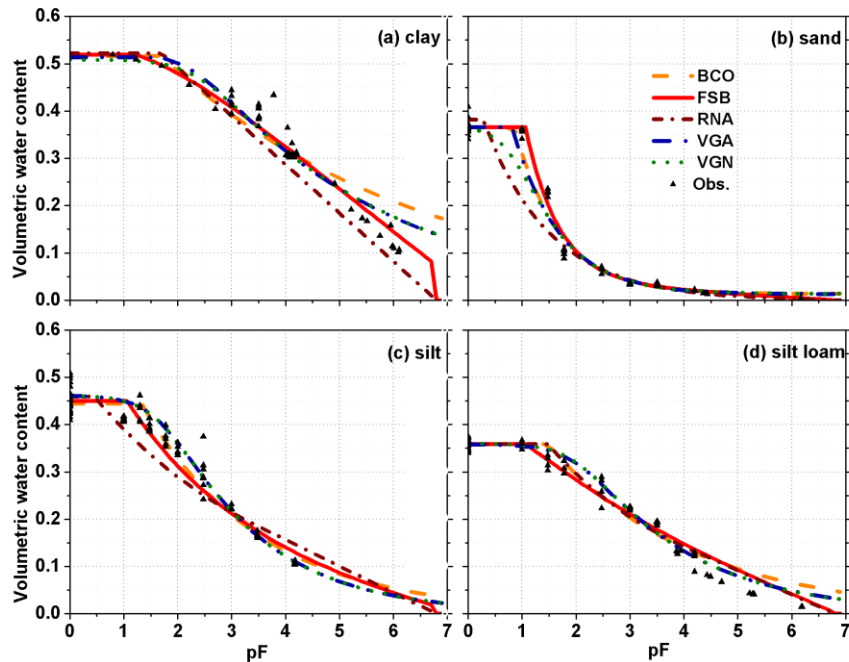


Figure 2.2: Observed and fitted retention curves for the different soil textures.

For sand, silt, and silt loam, independent observations of  $K(h)$  were available. The fits of Burdine's (1953) and Mualem's (1976) parameterizations based on retention data only were remarkably good for all parameterizations. The function of Alexander and Skaggs (1986) severely overestimated the hydraulic conductivity in all three cases, but very accurately described the slope of the curve for silt loam. Figure 2.3 demonstrates this for FSB, the results for the other parameterizations were comparable.

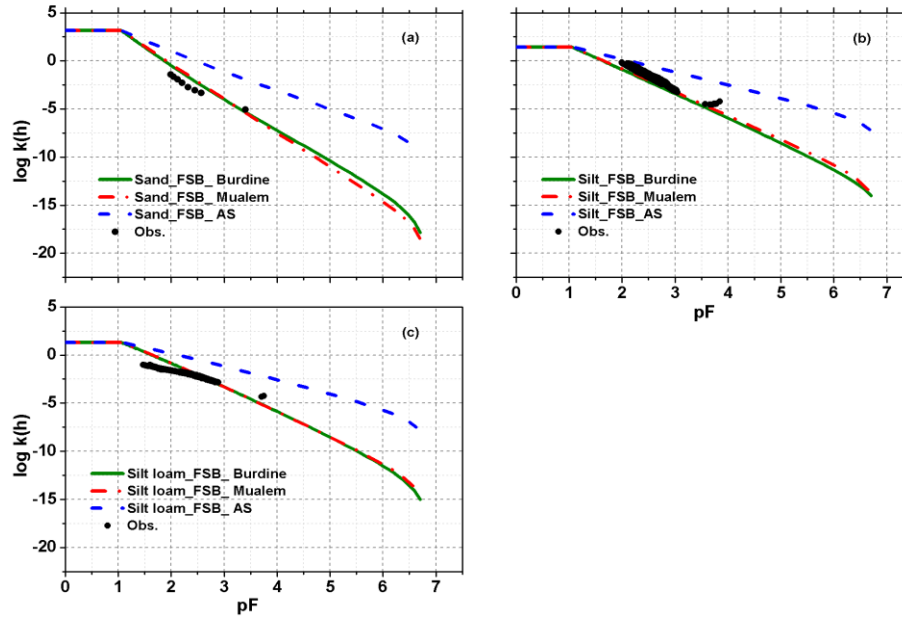


Figure 2.3: The observed and fitted hydraulic conductivity curve according to Burdine (1953), Mualem (1976) and Alexander and Skaggs (1986) using the fitted parameters of the Fayer and Simmons soil water retention curve (1995) for (a) sand, (b) silt, and (c) silt loam.

## 2.4.2. Simulation results

### 2.4.2.1. Silt

We start the analysis by examining the flux at the bottom of the soil profile. Panels a-e of (Figure 2.4) show all combinations of parameterizations of the retention and conductivity curves. The early rainfall cluster event at around  $t = 300$  d did not generate any bottom flux, and therefore only wetted up the soil profile. In doing so it increased the effect of the heavier rainfall around  $t = 656$  d on the bottom flux.

For the individual parameterizations, Mualem (M) and Burdine (B) gave reasonably similar results in which the second and third rainfall cluster generated a little more downward flow for B than for M. In all cases, Alexander and Skaggs (AS) gave a more rapid response of a very different magnitude. Clearly visible is a sustained, constant flux leaving the column during prolonged dry periods for the AS conductivity curves. This is physically implausible.

Figure 2.4f shows the substantial effect of the parameterization of the water retention curve on bottom fluxes when the M-type  $K(h)$  function is deployed. The results for B-type  $K(h)$  were comparable. Different retention curves gave very different responses to the initial conditions (not shown), highlighting the need to add a sufficiently long lead time ahead of the target time window to the simulated time period. RNA's response to the second and third rainfall clusters was about 2.4 times that of the others. At  $h = -300$  cm ( $pF$  2.48),  $K$  according to M is at least 5 times higher for RNA than for the rest, while the water content at that matric potential and higher values is relatively small (Figure 2.2c). Thus, infiltrated water was transported downward with relative ease, giving rise to the relatively high bottom fluxes and low evaporation rates that were computed for RNA (Figures 2.4f, 2.5f). The parameterizations other than

RNA behaved rather similar, except for the fact that VGA responded much faster to a change in the forcings than the other parameterizations.

Figure 2.4g shows the similar comparison of all parameterizations for the AS-type  $K(h)$  function. The response to rainfall was very fast and short-lived, which seems improbable for a silt soil that is far from full saturation. The non-physical bottom flux during dry periods (especially for VGA), the slow calculation times (half as fast as the others) with the time step always at the smallest permitted value, and non-negligible mass balance errors all point to numerical problems associated with AS.

The evaporative flux was nearly identical for B and M conductivity functions (Figure 2.5a-c). Since their bottom fluxes differed, this necessarily implies that the storage in the soil profile must also be different for B and M. The AS parameterization gave a much more spiky response of evaporative flux to rainfall than B or M, with zero evaporation most of the time (Figure 2.5a-d). In terms of cumulative evaporation, AS responded more strongly to the second rainfall cluster around  $t = 650$  d (Figure 2.5a-c). Overall, the effect of the conductivity function on evaporation was less pronounced than on the bottom flux. The same was true for the parameterization of the retention curve, as demonstrated by the relatively similar shapes of the curves in panels f and g of Figure 2.5.

Given the non-physical behavior of the bottom flux of AS for VGA in particular (Figure 2.4d), we also examined the infiltration. We first compare infiltration for VGA with M and AS-type conductivity (Figure 2.6a), and clearly see the zero infiltration for VGA during periods without rain contrasted to the impossible non-zero infiltration rates for AS during dry spells. For the other water retention parameterizations in combination with AS, the effect is less pronounced (Figure 2.6b). Still, the AS conductivity should be used with care and the results and mass balance checked.

Table 2.3 summarizes the bottom and evaporative fluxes. For evaporation, the differences are inconsequential except for the markedly low values for RNA. For the bottom flux, the difference between B and M is small enough to be within the margin of error for typical applications. The effect of the parameterization of the retention curve is an order of magnitude between the smallest bottom flux (for VGA) and the largest (for RNA).

Table 2.3: Cumulative bottom and evaporative fluxes (positive upwards) for silt from day 281 (the start of the first rainfall) onwards for Burdine and Mualem conductivity functions with the different parameterizations. The hydraulic conductivity at  $h = -300$  cm (the initial condition at the bottom is also given).

Parameterization	Cumulative bottom flux (cm)		Cumulative evaporation (cm)		$K(-300)$ (cm d <sup>-1</sup> )
	Burdine	Mualem	Burdine	Mualem	Mualem
BCO	-0.70	-0.500	34.147	34.445	0.00080
FSB	-1.240	-0.910	33.219	33.736	0.00147
RNA	-4.337	-3.650	27.046	28.184	0.00702
VGA	-	-0.248	-	34.956	0.00014
VGN	-	-0.744	-	34.359	0.00119

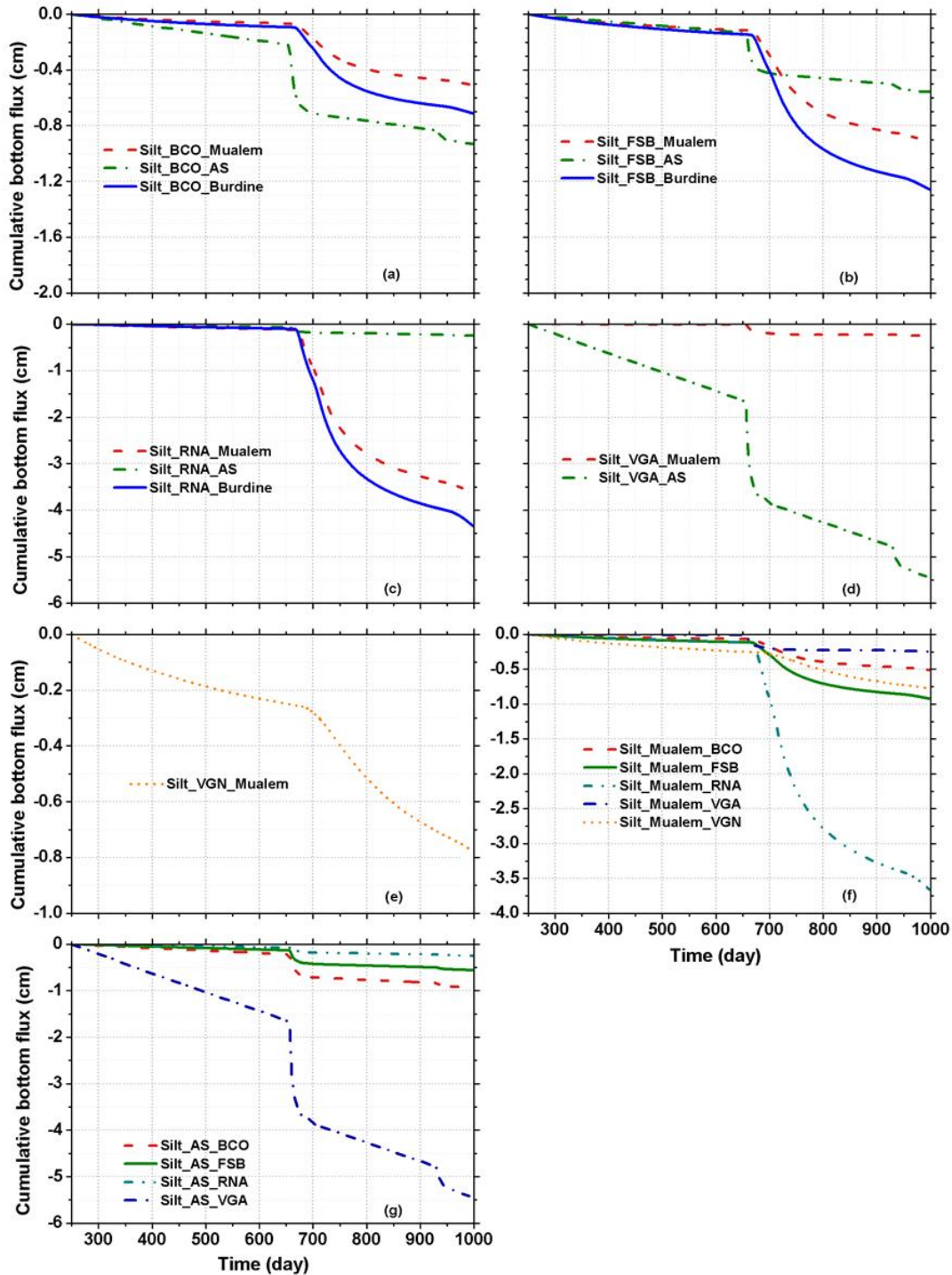


Figure 2.4: The cumulative bottom fluxes leaving a silt soil column for the different combinations of soil water retention curve and hydraulic conductivity parameterizations. Panels a through e present the results for the indicated retention parameterizations (see Table 2.1). Panels f and g organize the results according to the conductivity function: either Mualem (1976) (f) or Alexander and Skaggs (1986) (g).

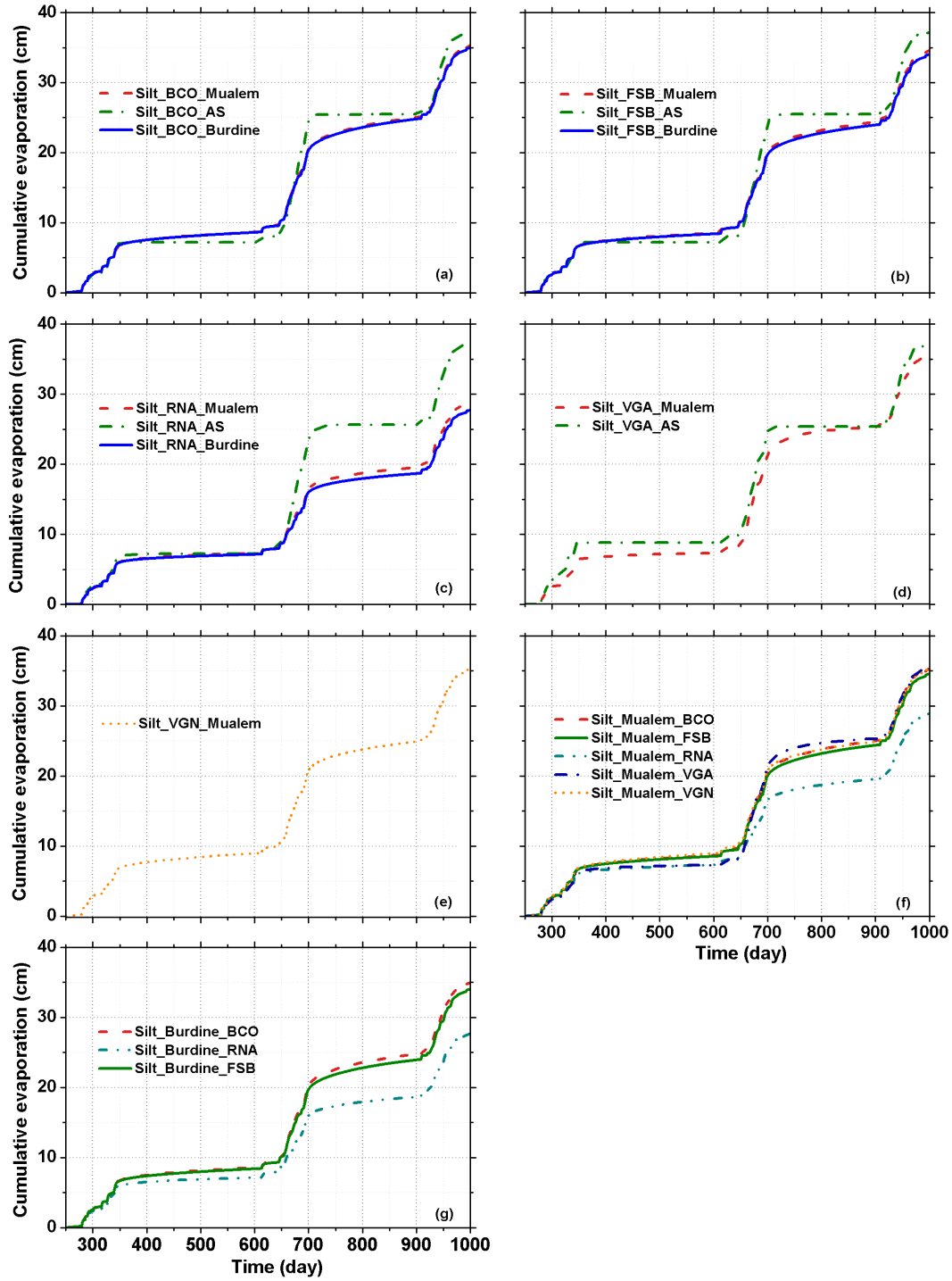


Figure 2.5: Cumulative evaporation from a silt soil column for the different combinations of soil water retention and hydraulic conductivity parameterizations. Panels a through e present the results for the indicated retention parameterizations (see Table 2.1). Panels f and g organize the results according to the conductivity function: either Mualem (1976) (f) or Burdine (1953) (g).

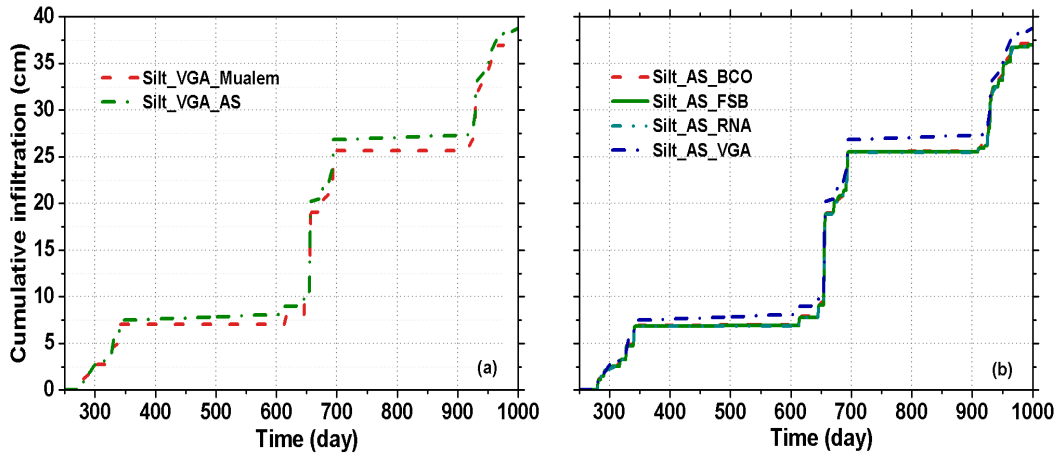


Figure 2.6: Cumulative infiltration in a silt profile for the VGA parameterization (see Table 2.1) with conductivity functions according to Mualem (1976) and Alexander and Skaggs (1986) (a) and four different parameterizations for the retention curve (see Table 2.1) with the Alexander and Skaggs conductivity function (b).

#### 2.4.2.2. Sand

The relationship between the bottom (Figure 2.7) and evaporative fluxes (Figure 2.8) as generated by the various parameterizations for the sandy soil were comparable to those for silt, and the analysis applied to the silt carries over to sand. The response to the initial conditions was less pronounced for AS conductivity functions, but still quite large. The bottom fluxes in sand responded faster and with less tailing than in silt, and the third rainfall cluster near the end of the simulation period produced a clear signal (Figure 2.7).

The FSB (Figure 2.7b) and RNA (Figure 2.7c) parameterizations were both in their logarithmic dry range when bottom fluxes occurred, and gave comparable values. BCO is not well adapted for dry conditions, and this is reflected by a bottom flux that is four times lower than the others (Figure 2.7g).

The bottom fluxes for BCO and FSB with AS-type  $K(h)$  are similar (Figure 2.7h), in stark contrast to the bottom fluxes based on B (Figure 2.7f) and M (Figure 2.7g) for these parameterizations. The similarity in the fluxes for AS reflect the facts that the evaporative fluxes (occurring in the wet range, where BCO and FSB both have Brooks-Corey retention curves) are very similar and the spiky response typical for AS results in small difference in storage between BCO and FSB. Consequently, the bottom flux, as the only remaining term of the water balance, cannot differ strongly between BCO and FSB. The difference in the bottom fluxes generated for VGN and VGA with M-type  $K(h)$  (Figure 2.7g) is even more extreme than in case of the silty soil.

For both M and B conductivity functions, the evaporation (Figures 2.8b and a) and the bottom flux (Figures 2.7a, f, and g) for BCO differed from the other parameterizations. These differences seem to have been dominated by the complementary responses of evaporation and bottom fluxes to the rainfall events around  $t = 656$  d. BCO converted roughly 5-7 cm more of this rainfall to evaporation than the other parameterizations, for both B and M. Therefore, less water was available for downward flow,

resulting in a cumulative bottom flux for BCO that was roughly 6 to 8 cm smaller than for the other parameterizations.

The AS-type  $K(h)$  function again gave a spiky response (Figure 2.8c). Nevertheless, the differences in the evaporation and the bottom flux compared to those of B and M are not very large. The bottom fluxes resulting from rainfall events were considerably smaller for RNA than for the other parameterizations.

Coarse-textured soils have the sharpest drop in the hydraulic conductivity as the soil desaturates. We therefore used the result for the sandy column to study the relationship between the matric potential at the bottom of the column and the bottom flux in order to evaluate water fluxes in dry soils. The free drainage lower boundary condition ensures there is always a downward flux that is equal to the hydraulic conductivity at the bottom at any time. Particularly for coarse soils this can still lead to negligible bottom fluxes for considerable periods of time. We first consider FSB and RNA, these being the parameterizations specifically developed to perform well in dry soils.

The difference in matric potentials between FSB and RNA is immediately clear from Figs. 2.9a, b and 2.10a, b. The effect of the conductivity function is manifest by including Figs. 2.9c and 2.10c in the comparison. The effect of the first rainfall cluster is visible in the matric potential in all cases (Figs. 2.9 and 2.10), but not enough to generate a significant flux. A flux through the lower boundary first occurs when the matric potential there exceeds (i.e. 795 becomes less negative than) -70 cm for FSB (Fig. 2.9a and b) and -30 cm for RNA (Figs. 2.10a and b).

The second rainfall cluster at  $600 < t < 700$  d did not rely on prewetting: it produced a bottom flux no matter how dry the soil was. The third rainfall cluster around day 930 probably would not have generated a bottom flux for B- and M-type  $K(h)$  functions, had the previous rainfall cluster not prewetted the soil. Note that the previous rainfall affects matric potentials at 1 m depth for several hundreds of days for B and M-type conductivity functions, but only for a few months at most for AS.

The AS-type  $K(h)$  function gave such rapid responses that only the second flux event at about 694 d was a result of recent pre-wetting at  $t = 656$  d (Figs. 2.9c and 2.10c). Despite the very different matric potentials at the bottom, the cumulative bottom fluxes produced by a single rainfall cluster generated by FSB and RNA were quite similar for B and M and only somewhat larger for AS (Figs. 2.9 and 2.10).

The AS conductivity function led the soil to dry out so completely that the atmospheric matric potential during dry spells was reached at 1 m depth in a few months (Figs. 9c and 10c). This seems unrealistic, and seems to be related to the significant overestimation of the unsaturated hydraulic conductivity by AS evidenced in Fig. 2.3.

For comparison, the bottom matric potentials and fluxes are given for BCO as well (Fig. 2.11). They are very different, and given the poor suitability of BCO for dry soils and the poor fitting performance probably incorrect. The differences between the parameterizations illustrate the need to carefully consider the suitability of the parameterization for the intended purpose.



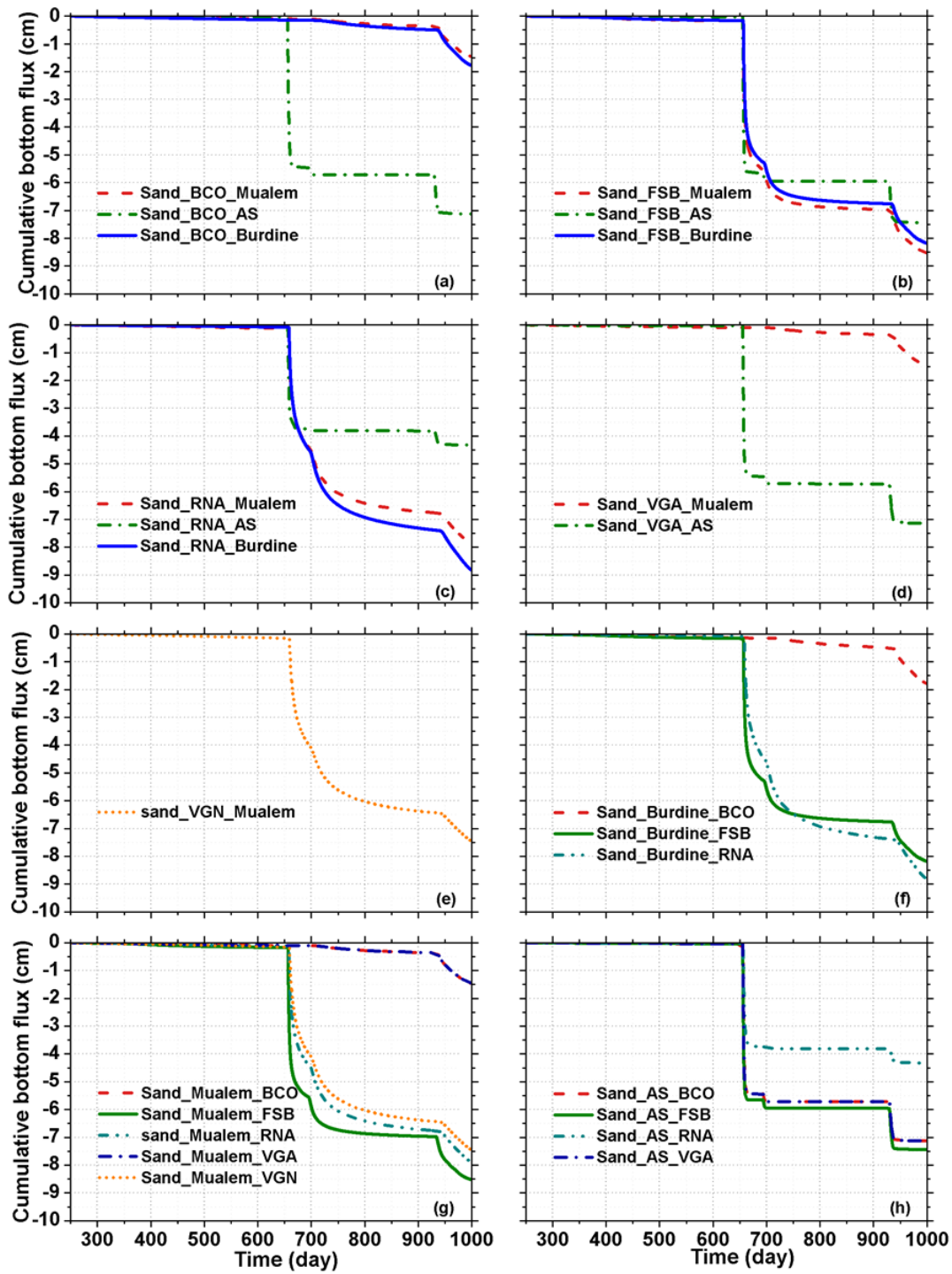


Figure 2.7: As Fig. 2.4, but for a sandy soil column. Unlike Fig. 2.4, the results of Burdine's (1953) conductivity curve are shown (panel f).



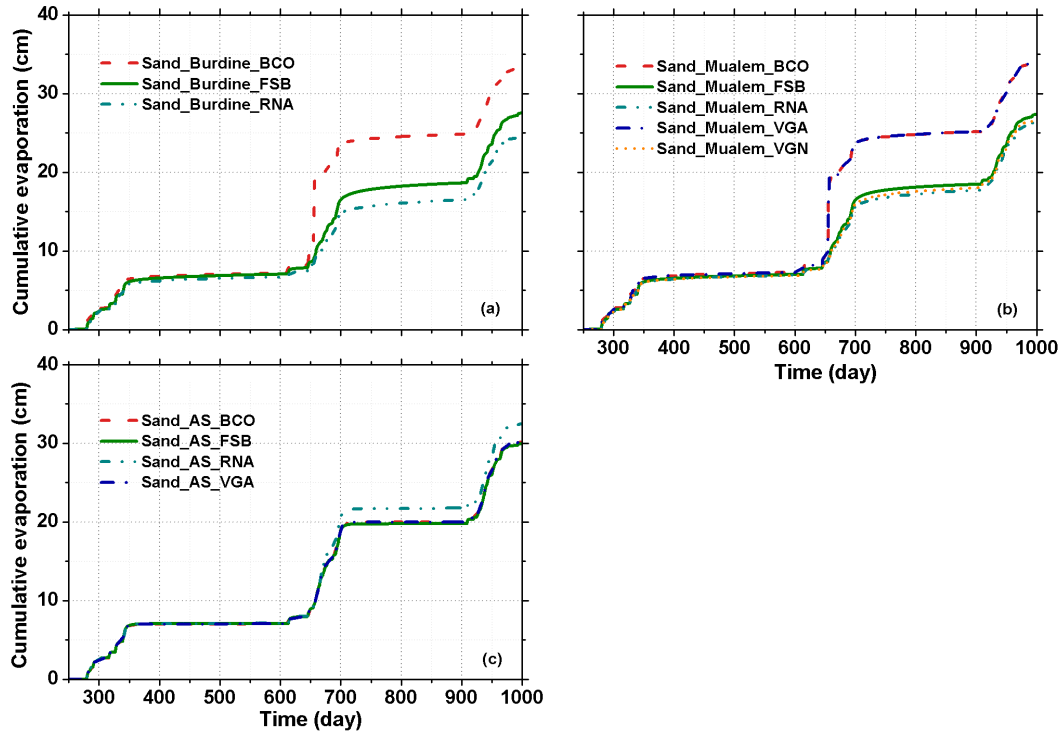


Figure 2.8: Cumulative evaporation from a sandy profile for the different combinations of retention curve parameterizations (see Table 2.1) and hydraulic conductivity functions: Burdine (1953) (a), Mualem (1976) (b) or Alexander and Skaggs (1986) (c).

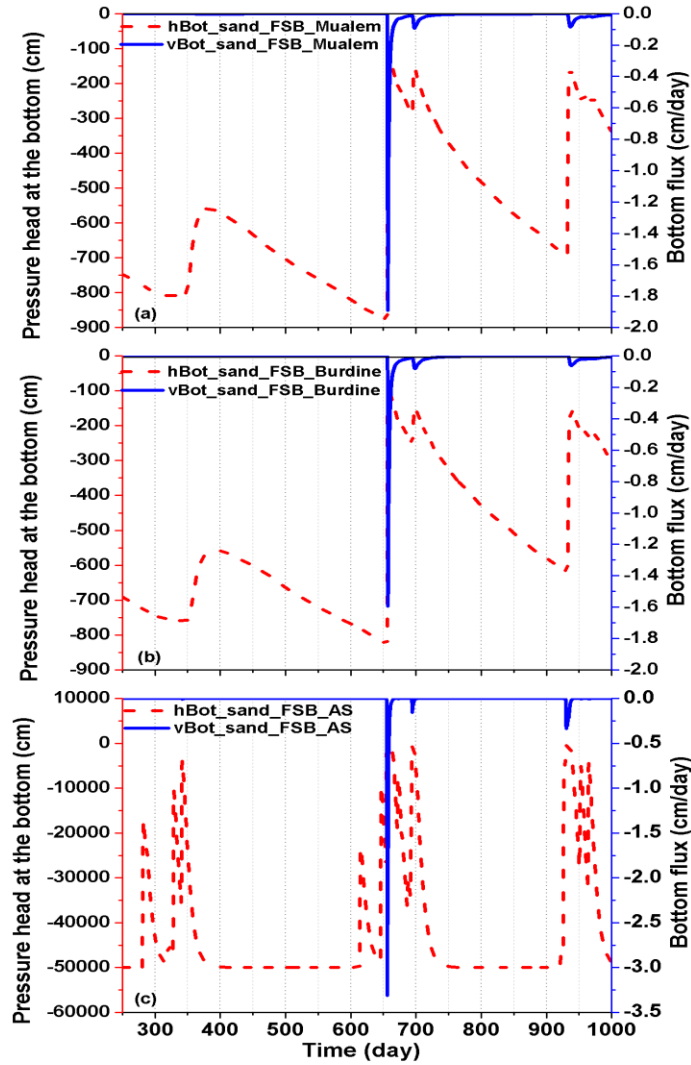


Figure 2.9: Pressure head  $h_{Bot}$  and flux density  $v_{Bot}$  at the bottom of the sand column for the FSB parameterization (see Table 2.1) and the conductivity functions of Mualem (1976) (a), Burdine (1953) (b) and Alexander and Skaggs (1986) (c).

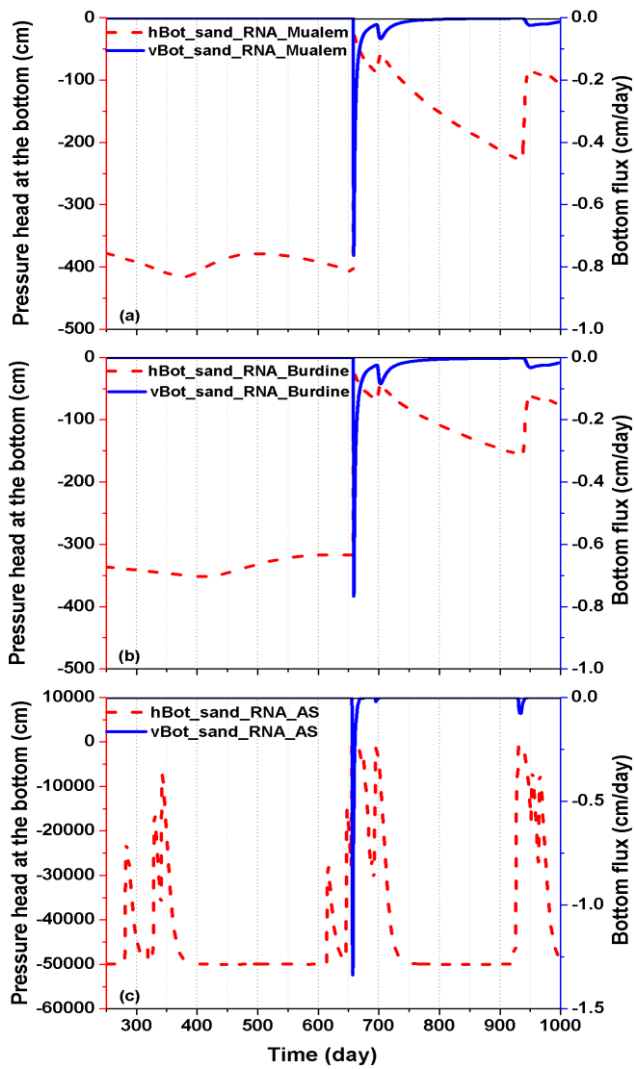


Figure 2.10: As Figure 2.9, but for the RNA parameterization (see Table 2.1).

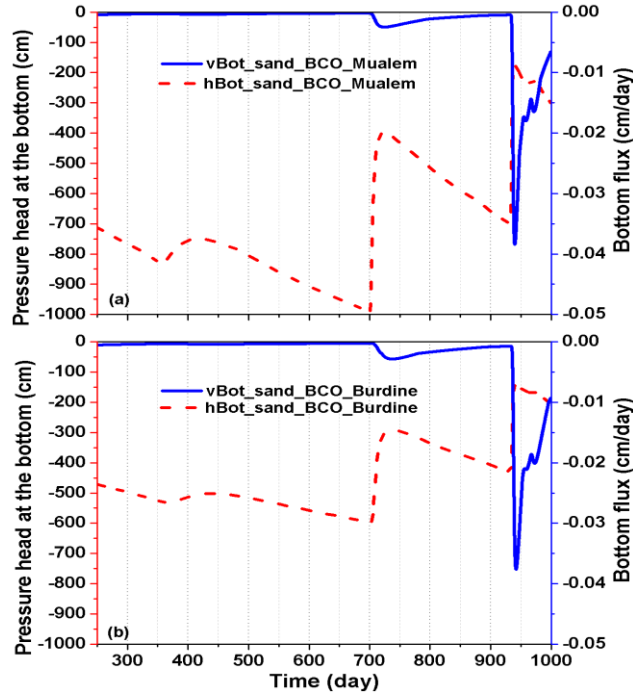


Figure 2.11: As Figure 2.9, but for the BCO parameterization (see Table 2.1).

### 2.4.2.3. Silt loam and clay

The bottom fluxes from the clay and the silt loam soil for all combinations of parameterizations for the soil water retention and hydraulic conductivity curves were similar to those for the silt soil (Figures 2.12 and 2.15), with two notable exceptions: for RNA, there was a much more damped response to the rainfall around  $t = 656$  d for either the B or the M-type  $K(h)$  function (Figure 2.12c), in comparison to the rapidly increasing bottom flux in silt. In clay, there was virtually no response anymore (Figure 2.15c). In general, the bottom fluxes for all parameterizations displayed comparable behavior with the exception of those with AS-type  $K(h)$  functions (Figures 2.12 and 2.15).

The behavior of the evaporative fluxes from the silt loam and the clay soil for all combinations of parameterizations for the soil water retention and hydraulic conductivity curves was essentially similar to that for the silty soil (Figures 2.13 and 2.16). The main difference was the less gradual response of the evaporation for VGA, particularly for clay, which was, in fact, rather similar to the notoriously spiked response of the AS-type conductivity function. The relative amounts of evaporation of the various parameterizations varied from one texture to another.

For AS in combination with the VGA retention curve, there was significant infiltration during periods of zero rainfall (Figures 2.14 and 2.17). This numerical artefact led to erroneous simulations of the bottom flux. This is the most significant occurrence of mass balance errors that plague the simulations with AS-type  $K(h)$  functions in silt loam and clay, as they did in silt. Evidently, the AS parameters for the  $K(h)$  curve cause numerical problems in fine-textured soils.

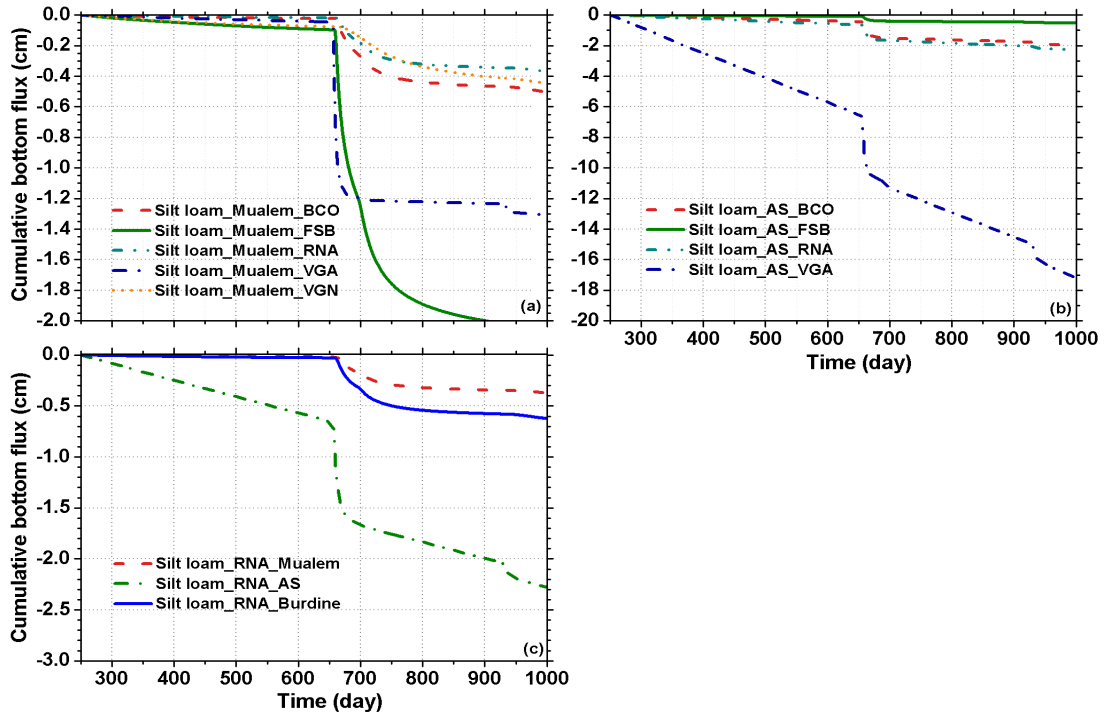


Figure 2.12: Cumulative bottom fluxes from a silt loam profile for all combinations of parameterizations (see Table 2.1) and Mualem's (1976) (a) and Alexander and Skaggs' (1986) conductivity functions (b), and for the RNA parameterization with all three conductivity functions (c).

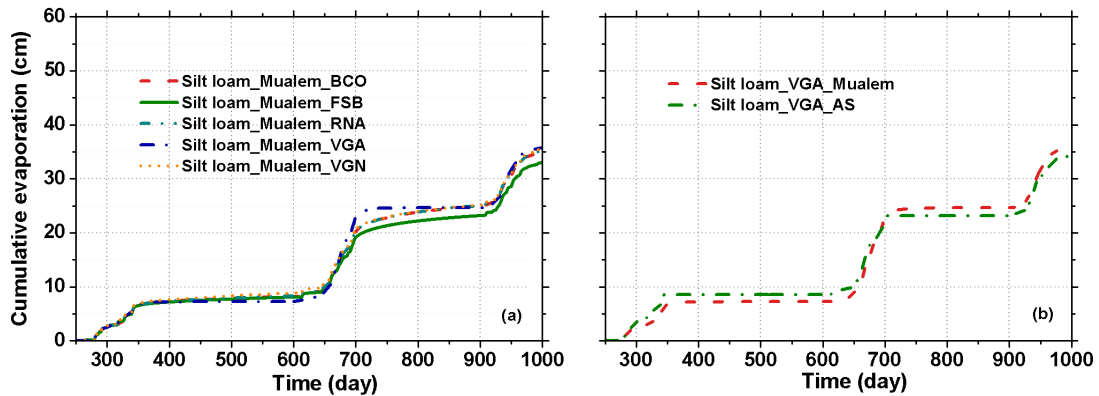


Figure 2.13: Cumulative evaporation from a silt loam profile for all parameterizations (see Table 2.1) with Mualem's (1976) conductivity function (a) and the VGA parameterization with conductivity functions according to Mualem (1976) and Alexander and Skaggs (1986) (b).

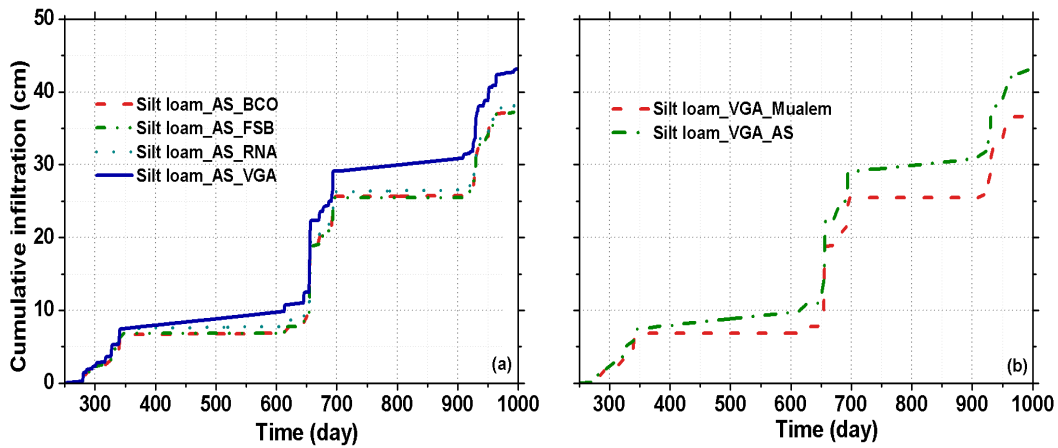


Figure 2.14: Cumulative infiltration from a silt loam profile for four parameterizations (see Table 2.1) with the Alexander and Skaggs (1986) conductivity function (a) and for the VGA parameterizations with conductivity functions according to Mualem (1976) and Alexander and Skaggs (1986) (b).

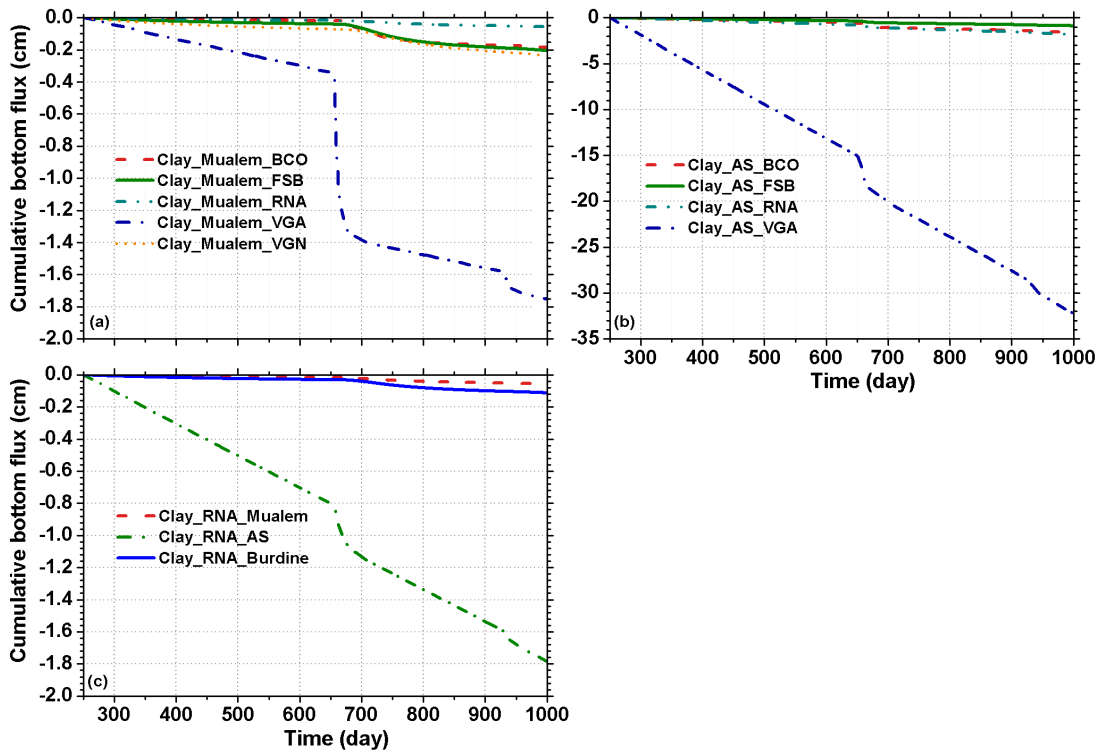


Figure 2.15: As Fig. 2.12, for clay.

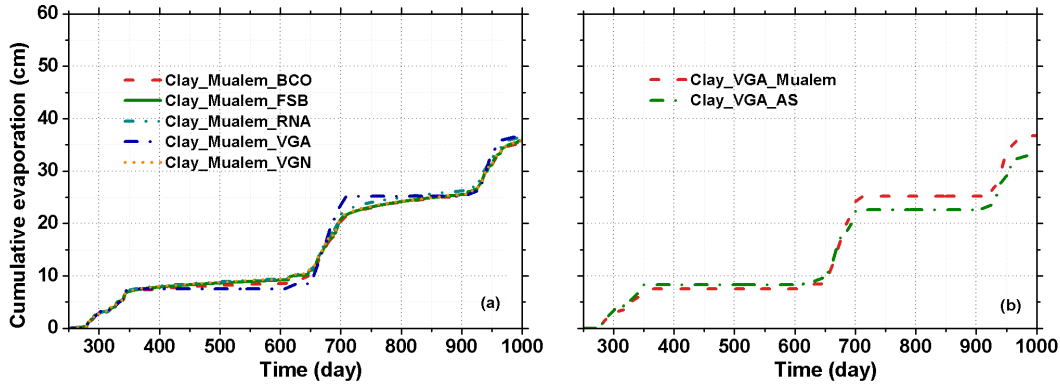


Figure 2.16: As Fig. 2.13, for clay.

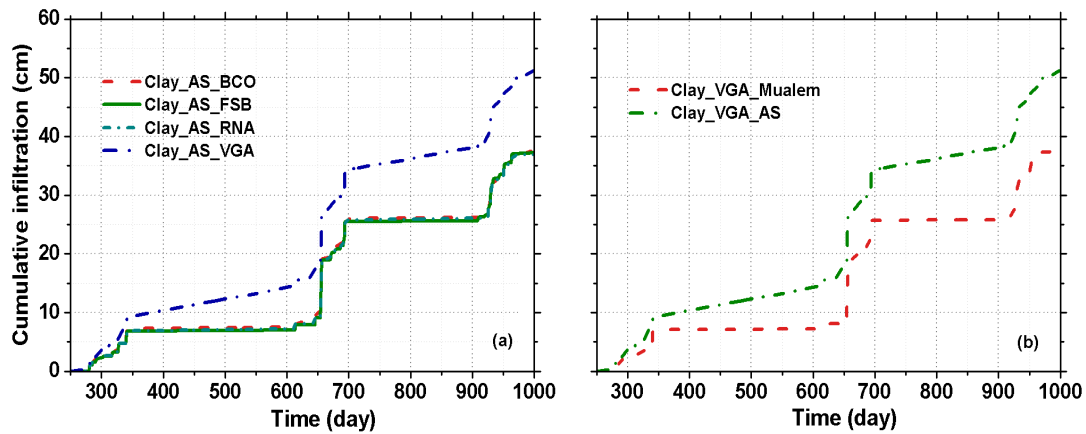


Figure 2.17: As Fig. 2.14, for clay.

### 2.4.3. General ramifications

We found that 14 out of 18 parameterizations of the soil water retention curve were shown to cause non-physical hydraulic conductivities when combined with the most popular (and effective) class of soil hydraulic conductivity models. For one of these cases (VGN), Ippisch et al. (2006) demonstrated convincingly that their alternative (VGA) significantly improved the quality and numerical efficiency of soil water flow model simulations, and our simulations confirmed the profound effect of this modest modification on the model results. We hope that the general criterion we developed for verifying the physical plausibility of the near-saturated conductivity will be used in the selection of suitable soil hydraulic property parameterizations for practical applications of numerical modeling of water flow in soils, and likewise will be of help in improving existing parameterizations (as we have done in a few cases here) and developing new ones.

The ability of both Burdine's (1953) and Mualem's (1976) models of the soil hydraulic conductivity function to predict independent observations of the soil hydraulic conductivity curve on the

basis of soil water retention parameters fitted on water content data only is reasonably good, at least for the limited data available to test this. The conductivity model of Alexander and Skaggs (1986) overestimated the conductivity of the soils for which independent data were available. This resulted in a rapid and unrealistically strong response to changes in atmospheric forcings even at 1 m depth, as shown in our simulation study.

The simulations with different parameterizations showed that under the given boundary conditions the choice of the parameterization had a modest effect on evaporation, but strongly affected the partitioning between soil water storage and deep percolation. The uncritical use of a default soil hydraulic parameterization or selecting a parameterization solely based on the quality of the fit to soil water retention data points entails the risk of an incomplete appreciation of the potential errors of the water fluxes occurring in the modeled soil. This points to the importance of carefully considering the soil hydraulic parameterization to be used for long-term water balance studies that aim to determine or predict the variation of seasonal water availability to plants or long-term groundwater recharge to assess the sustainability of extractions from an underlying aquifer. If at all possible, observations during dynamic flow (water contents, matric potentials, fluxes) should be included in the parameterization selection process. In this context it would be interesting to see if parameter-estimation-processes based on inverse modeling of a non-steady unsaturated flow experiment would lead to a different choice of parameterization than fitting parameters to data points obtained at hydrostatic equilibrium. This requires the inclusion of all the parametric expressions of interest in the numerical solvers of Richards' equation capable or running in parameter estimation mode.



## Chapter 3

### 3. Liquid water and vapor flow in dry sand: column experiments and numerical tests of different retention curve parameterizations.

#### Abstract:

To estimate groundwater recharge in (semi-)arid regions under changing conditions, the processes in the unsaturated zone, including the movement of water vapor, need to be considered. Calculating coupled flow of liquid water and vapor requires soil water retention and hydraulic conductivity curves that are accurate over the full water content range from oven-dryness to saturation. We tested those parameterizations of the soil water retention curve that can be combined with the most popular parameterization for the conductivity curve without giving physically unrealistic behavior of the near-saturation conductivity, as well as the *de facto* standard parameterization. The latter can give unrealistically rapid increases of the conductivity close to saturation. We filled columns with dry to slightly moist sand over a saturated 1-cm bottom layer and let them dry out under a high potential evaporation rate. We monitored soil temperature, soil air humidity, and evaporation rate. At the end we determined the salt profile for the columns that started with saline water in the saturated bottom layer. Simulations of coupled liquid water and vapor flow only converged for the two parameterizations with realistic conductivity curves. They revealed the downward movement of a sharp interface between liquid flow below a vaporization layer and vapor flow above it, which created a salt profile that was in qualitative agreement with the observations. Only one parameterization was able to reproduce the evaporation rate with time.

#### 3.1. Introduction

In (semi-)arid regions, the vapor flux in the unsaturated zone is likely to be important: its flux density will probably be small at any time, but it can operate for months and even years between sporadic rainfall events and thus contribute significantly to the long-term water balance of the unsaturated zone. Philip and de Vries (1957) were the first to present a theoretical treatment of liquid and vapor flow. Since then, work specifically targeted at (semi-)arid conditions emerged.

Some of this work considered the magnitude of individual rainfall events. It was found that one role of vapor flow in (semi-)arid regions is the transfer of all water delivered by small rain showers back to the atmosphere (e.g., Schulz et al., 2016). Other work considered long dry spells, and found that during such spells, vapor flow is likely to be the dominant water transport mechanism (Jackson, 1964; Zeng et al., 2009). Consistent with this, Rose (1963a, 1963b, 1968a, 1968b) demonstrated that the liquid diffusivity in semi-arid regions is generally smaller than the vapor diffusivity, and that the evaporative demand typically exceeds the ability of soil to conduct liquid water. Walvoord and Scanlon (2004) found that vapor flow is an important factor in the redistribution of water in deep soils, particularly in coarse-

grained sediments. Scanlon's (1992) tracer studies showed that the calculated vapor flux was two to eight orders of magnitude larger than the liquid fluxes in a desert field site in Texas. Barnes and Turner (1998) reported considerable mass transport in the unsaturated zone in the vapor phase driven by thermal gradients in a deep (>10 m) sand dune soil, and de Vries and Simmers (2002) showed in their work significant effects of vapor fluxes on groundwater recharge. Recently, Goss and Madliger (2007) conducted in situ measurements of relative humidity and temperature in a dry Tanzanian soil, then calculated the water vapor diffusion fluxes from the coupled relative humidity and temperature measurements, and found that the water vapor transport dominated in the surface layer under dry conditions. These independent findings suggest that reliable estimates of groundwater recharge in semi-arid regions require that the vapor flux is properly accounted for (Scanlon et al., 2003; Saito et al., 2006).

An interesting aspect is the location and movement of the evaporation front in the soil, below which water is mainly transported in the liquid phase, whereas vapor flow is the dominant transport mode between the front and the soil surface. Konukcu et al. (2004) were able to determine the critical water content (below which water is mainly transported in the vapor phase) and the range of water contents in the transition zone from liquid to vapor, both theoretically and in column experiments. Gowing et al. (2006) carried out experiments to locate the evaporation front and to predict the evaporation rate under isothermal conditions. They found a relation between the evaporative demand, the depth of the evaporation front, and salt accumulation within the soil profile. Shokri and Or (2011) were able to define the vapor diffusion length by estimating the depth of the evaporation front at evaporation stage 2 (the stage with a gradually dropping evaporation rate in which the vapor-transport is diffusion-limited (Or et al., 2013)).

The desire to predict groundwater recharge under changing conditions and the importance of water flow in both the liquid and the vapor phase in the unsaturated zone leads to the need to consider coupled flow of liquid water, water vapor, and heat in dry soils (Saito et al., 2006). To handle the liquid water flow component, the soil water retention curve and the hydraulic conductivity curve that characterize the soil are typically supplied in parametric form. Particular attention needs to be paid to the behavior of these curves in the dry end, not only because vapor flow is dominant there (Barnes and Turner, 1998; de Vries and Simmers, 2002), but also because film flow and corner flow become the main modes of liquid flow (Tuller and Or, 2001; Lebeau and Konrad, 2010; Peters, 2013).

The most widely used soil hydraulic parameterization is that of van Genuchten (1980) coupled with Mualem's (1976) model for unsaturated hydraulic conductivity. Unfortunately, its performance in dry soils is not very good (Sakai et al., 2009; Schneider and Goss, 2012), where the water contents go below the residual water content (Fuentes et al., 1991). Several parameterizations were developed specifically to perform well in the dry range (e.g., Rossi and Nimmo, 1994; Fayer and Simmons, 1995; Morel-Seytoux and Nimmo, 1999; Webb, 2000). Leij et al. (1997) and Khlosi et al. (2008) provide an overview of many soil hydraulic parameterizations.

In Chapter 2 we critically evaluated the most-used parameterizations and those specifically developed for dry conditions. The main objective of this chapter is to test those that were found to be physically sound. To do so we designed a column experiment in which vapor flow would be important and modeled it with a code (HYDRUS-1D) capable of solving the coupled partial differential equations for liquid water flow, heat flow, and water vapor diffusion in a porous medium (Šimůnek et al., 2016). Another objective is to verify if the numerical model is capable of reproducing the occurrence of an evaporation front, and if so, how the behavior of this front is affected by the choice of hydraulic parameterization.

## 3.2. Materials and Methods

### 3.2.1. Experimental set-up

We prepared 8 PVC cylinders (15.0 cm inner diameter and 25.0 cm height, closed at the bottom), made ports in their walls to facilitate various sensors (Figure 3.1), and filled them with commercially available sand (<http://sand-schulz.de/>) with sieve fractions < 0.63 mm (6%), 0.63 – 0.8 mm (12%), 0.8 – 1.0 mm (54%), and 1.0 – 2.0 mm (28.7%). We measured the soil water retention curve (Figure 3.2) of the sand with the HYPROP<sup>®</sup> apparatus (UMS GmbH, Munich, Germany), based on Schindler et al.'s (2010) evaporation method. We measured a saturated hydraulic conductivity of  $3.69 \cdot 10^4 \text{ cm d}^{-1}$  according to the constant head method of Dirksen (1999, p. 78-79).

To achieve different initial conditions, we mixed the air-dry sand with tap water to obtain estimated volumetric water contents of 0.00, 0.02, 0.05, and 0.08. To do so, we determined the dry bulk density and the mass of sand of 10 prepacked columns. We converted the target volumetric water contents to gravimetric water contents and then added the desired mass of water to weighed amounts of sand in plastic bags. The bags were then sealed plastic for a few days to allow redistribution. Immediately before packing the columns, the content of the bags was thoroughly mixed without breaking the seals.

In order to create a wet region at the bottom of the columns, we filled the bottom 1 cm of four columns with sand saturated with tap water. Then, we added the sand-water mixtures in 3 – 4 cm layers, packed each layer by gentle pounding (Figure 3.3), loosened the top 1 cm and added the next layer. The other four columns were packed similarly, but this time the tap water of the bottom centimeter was replaced by a 10 mmol l<sup>-1</sup> NaCl solution in tap water. The aim was to have an independent check on the depth of the evaporation front from the salt profile at the end of the experiment: we expected the salt to accumulate at the evaporation front. We kept the concentration low to minimize the effect of the osmotic potential on the total water potential (Kamphorst et al., 1978). All columns were packed to 0.5 cm below the rim.

In each column, the water content was measured using three EC-5 probes (Decagon Devices, Inc.), installed at 17.0, 20.0, and 23.0 cm depth (Figure 3.1). We calibrated the sensors for the sand we used and found an accuracy of 2%. The relative humidity (2.5% accuracy) and the temperature (0.3 °C accuracy) were measured at 5.0, 17.0, and 20.0 cm depth by EE060 sensors (E+E Electronic Company). At 23.0 cm depth, a platinum resistance sensor PT100 gave an independent temperature reading (accuracy not known). All sensors were installed during the soil packing procedure.

The columns were placed on electronic balances (0.1 g accuracy) inside a climate chamber. The masses were logged automatically every 15 minutes. The sensors were hooked up to a DT80 Data Taker datalogger through two multiplexers from the same supplier, and logged in 15-minute intervals as well. Potential evaporation was measured by placing two PVC water cylinders (15.0 cm inner diameter, 5.5 cm height) filled with tap water on electronic balances inside the climate chamber and manually recording their masses once a day. The water level in these cylinders was kept at about 0.2 to 1.5 cm below the rim.

The temperature in the climate chamber was set to 40 (±1) °C, and the target relative humidity of the air in the chamber at 0.1. The experiment ran for 95 days, after which the mass of the columns had become nearly constant. At the end of the experiment we measured the NaCl concentrations along the column length for the four columns with the saline solution in the bottom centimeter by extracting manually all sand of every 1-cm interval column and then adding a measured amount of water and measuring the electrical conductivity of the resulted solution by a regular EC meter. The volume of resident water in the sand was negligible for all depths.

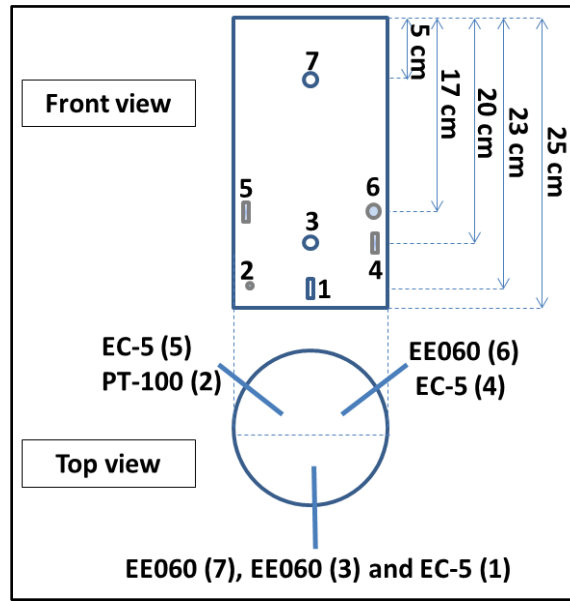


Figure 3.1: Schematic drawing of the top and front view of an experimental column with the location of the slots (denoted by numbers) for the sensors. The relative humidity sensors are denoted EE060, the water content sensors EC-5, and the temperature sensor PT-100. The top view shows how deep the sensors penetrated the soil. The water content probes were installed with the two leads vertically aligned.

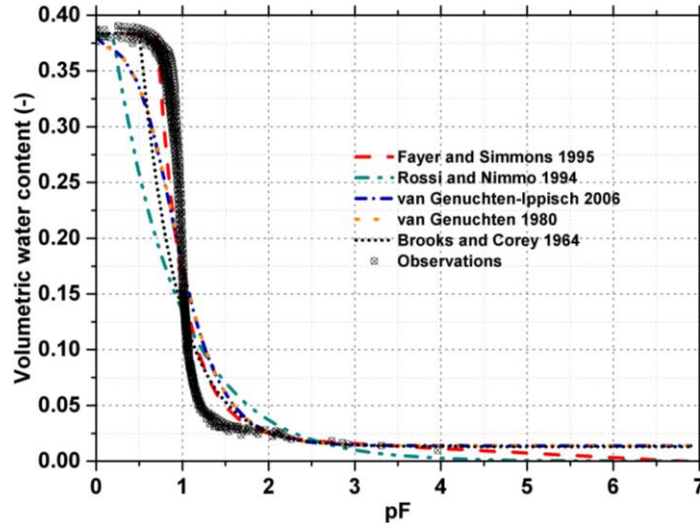


Figure 3.2: The measured water retention curve of the sand used in the experiment. The fitted water retention curves according to Brooks and Corey (1964), van Genuchten (1980), Rossi and Nimmo (1994) (junction model without parabolic correction at the wet range), Fayer and Simmons (1995), and Ippisch et al. (2006) are shown as well.

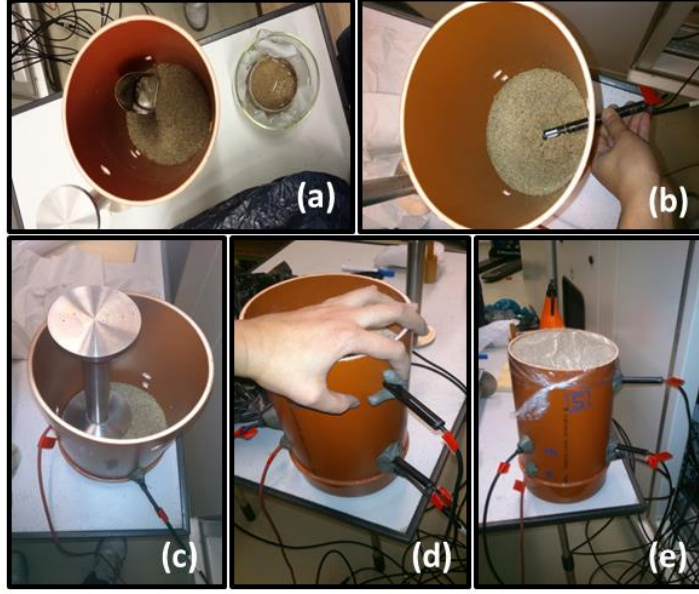


Figure 3.3: The different column packing steps: (a) packing the first saturated sand layer, (b) inserting the first sensor, (c) packing the added sand layers, (d) sealing the installation ports, (e) covering the column's upper surface with plastic until the start of the experiment.

### 3.3. Numerical modeling

#### 3.3.1. Governing equations and their numerical implementation

The simulations were carried out with the public-domain modeling package HYDRUS-1D for Windows version 4.16.0090 (Šimůnek et al., 2013, 2016). Liquid water movement was governed by the conventional Darcy-Buckingham Law. Water vapor movement was assumed to be purely diffusional, implying that there was no advective movement of the gas phase in the soil. This assumption may not be valid in case of an infiltration front that displaces the soil gas phase. But under more gradual infiltration and especially in dry periods, the assumption is physically plausible. An additional assumption was that the local equilibrium between the matric potential of the liquid water and the vapor pressure in the gas phase was instantaneous. With this assumption, liquid water and vapor movement in a soil profile could be captured in a single partial differential equation that is based on Richards' equation for liquid water flow:

$$\frac{\partial \theta_T(h)}{\partial t} = \frac{\partial}{\partial z} \left[ (K + K_{vh}) \frac{\partial h}{\partial z} - K \right] \quad (3.1)$$

where  $z$  is the vertical coordinate (positive upwards; L),  $t$  denotes time (T),  $h$  is the matric potential expressed as an equivalent water column (L),  $K$  is the isothermal hydraulic conductivity of the liquid phase ( $LT^{-1}$ ),  $K_{vh}$  is the isothermal hydraulic conductivity of water vapor ( $LT^{-1}$ ), and  $\theta_T = \theta + \theta_v$  is the total volumetric water content, with  $\theta$  the volumetric liquid water content and  $\theta_v$  the volumetric water vapor content. If desired, root water uptake could be represented by a sink term.

Given the isothermal nature of the experimental set-up as verified in the soil temperature measurements, we did not adopt a more rigorous version of equation (3.1) with terms accounting for temperature gradients. For the same reason, the coupled solution of the heat flow equation was also unnecessary. We refer to the Hydrus manual (Šimůnek et al., 2013) for details on these equations and their implementation.

In order to model vapor diffusion with Eq. (3.1), the vapor diffusion coefficient that describes vapor flow driven by a gradient in the vapor pressure must be converted into an equivalent hydraulic conductivity that describes vapor flow driven by a gradient in the matric potential, which is achieved through the following equation (Šimůnek et al., 2013, equation 2.43):

$$K_{vh} = \frac{D_v}{\rho_w} \rho_{vs} \frac{Mg}{RT} H_r \quad (3.2)$$

where  $D_v$  is vapor diffusivity in soil ( $L^2T^{-1}$ ),  $\rho_{vs}$  is the saturated vapor density ( $ML^{-3}$ ),  $\rho_w$  is the density of liquid water ( $ML^{-3}$ ),  $M$  is the molar mass of water ( $M \text{ mol}^{-1}$ ),  $g$  is the gravitational acceleration ( $LT^{-2}$ ),  $R$  is the universal gas constant ( $J \text{ mol}^{-1} K^{-1}$ ), and  $H_r$  is the relative humidity. Additional equations for various parameters in equation (3.2) are given by Šimůnek et al. (2013, p. 28-29).

The movement of the salt was modeled by the conventional advection-dispersion equation (Leij and van Genuchten, 2002). Solute transport only occurred in the liquid phase. The liquid flux density that determined the advective transport component was derived from the solution of equation (3.1).

The initial condition was a uniform matric potential over the top 23.5 cm of the column, derived from the volumetric water content. The 1.0 cm thick bottom layer had an initial matric potential corresponding to hydrostatic equilibrium in a 1 cm thick saturated bottom layer. At the bottom of the column, a no-flow boundary condition applied. At the top, the temperature and target relative humidity of the air in the climate chamber were converted to a fixed matric potential boundary condition (pF 6.53) according to Kelvins's Law (Or and Wraight, 2000). Simulations were run for a 95-day period.

For the salt transport we set the longitudinal dispersivity to 0.2 cm and the bulk density equal to the average value of  $1.568 \text{ g cm}^{-3}$  (calculated from the mass of the experimental columns at the end of the experiment). At the upper and lower boundaries we implemented zero solute flux conditions. The initial salt concentration was  $0.584 \text{ mg cm}^{-3}$  in the lower 1.0 cm of the column and zero everywhere else.

Preliminary simulations showed that time steps in the order of  $10^{-5}$  to  $10^{-3}$  d sufficed to achieve convergence for the simulation of Eq. (3.1), but produced liquid water and vapor fluxes that were much smaller than those observed. The simulation results presented here are based on simultaneous solutions of equation (3.1) and the advection-dispersion equation (even for the solute-free columns), which had time steps that in the startup phase of the simulation were as small as  $10^{-7}$  to  $10^{-6}$  d, and toward of the simulation period increased to  $10^{-5}$  to  $10^{-4}$  d. The results of these model runs were much closer to the observations.

### 3.3.2. Selected Parameterizations

In Chapter 2 we identified two parameterizations that should perform well in dry soils and at the same time do not suffer from the detrimental shape of the hydraulic conductivity curve near saturation that was analyzed for van Genuchten's (1980) parameterization by Ippisch et al. (2006). One of these is

the parameterization by Fayer and Simmons (1995) based on Brooks and Corey (1964) (denoted FSB) (Eq. (2.16a) in Chapter 2). The other parameterization is the junction model of Rossi and Nimmo (1994), but without the parabolic correction for the wet end of the retention curve (denoted RNA) (Eq. (2.13a) in Chapter 2).

In Chapter 2 we also found two parameterizations with physically plausible hydraulic conductivities near saturation that were not tailored to do well in the dry range. The first (Eq. (2.5a)) is the original parameterization of Brooks and Corey (1964) (denoted BCO). The second (Eq. (2.11a)) is the modified version of *van Genuchten's* (1980) expression presented by Ippisch et al. (2006) (denoted VGA). Because of its widespread use and *de facto* status of being the current standard parameterization, we also selected for consideration the original parameterization of van Genuchten (1980) (Eq. (2.8a), denoted VGN).

All five parameterizations of the soil water retention curve were combined with Mualem's (1976) model for the soil hydraulic conductivity to yield closed-form expressions for both the retention and the hydraulic conductivity curve (see Chapter 2). We employed the Shuffled Complex Evolution parameter estimation used also in Chapter 2 to fit the various parameterizations to soil water retention data. With the retention parameters identified, Mualem's (1976) model fully defined the corresponding soil hydraulic conductivity curves. With the retention parameters known, we could convert the initial water contents to initial matric potentials (Table 3.1).

The parameter values were used to generate up to 100 points on the soil water retention and soil hydraulic conductivity curves spanning the full range from saturation to oven-dryness. These were then passed on to the HYDRUS-1D code as a look up table in input file MATER.IN.

Table 3.1: The initial conditions in volumetric water contents and in pressure heads for the various initial water contents and soil hydraulic parameterizations: BCO: Brooks and Corey (1964); FSB: Fayer and Simmons (1995); RNA: Rossi and Nimmo (1994); VGA: Ippisch et al. (2006); VGN: van Genuchten (1980).

Initial volumetric water content	Initial $h$ (cm H <sub>2</sub> O)			
	BCO	FSB	RNA	VGA and VGN
0.00	$-3.162 \cdot 10^6$	$-3.162 \cdot 10^6$	$-3.162 \cdot 10^6$	$-3.162 \cdot 10^6$
0.02	-199.5	-199.5	-299.9	-158.5
0.05	-34.4	-30.0	-55.0	-40.0
0.08	-18.0	-18.0	-25.0	-23.0

### 3.4. Results and Discussion

#### 3.4.1. Experimental results

The daily potential evaporation rate in the chamber was 0.9 cm d<sup>-1</sup>. This high atmospheric demand caused the columns to dry out within the 95-day experimental period. Figure 3.4 shows the evaporation rate with time. The data for the dry column with added salt (Figure 3.4b) and the column with an initial water content of 0.08 without added salt (Figure 3.4g) were very noisy for unclear reasons, and were not analyzed further. Most of the data sets did not cover the full experimental period because an unexpected surge in the power supply destroyed several of the balances.

The different levels of noise of the data are probably caused by external factors, such as movement of the cables of the sensors in by the air flow from the climate chamber ventilation system, by disruptions during battery replacement, datalogger hook-up to the laptop for data retrieval, etc. If we look beyond the noise, Figure (3.4) shows that the small amount of salt added to the water at the bottom of the column did not affect the evaporative flux.

Even for the columns that were initially dry above the saturated bottom 1 cm (Figure 3.4a, b), evaporation started immediately, albeit at a lower rate than for the wetter columns (Figure 3.4c-h). In the time between the filling of the columns and their placement in the climate chamber, some redistribution and evaporation within the sealed columns had already taken place, making some of the water available for immediate evaporation, even in the initially dry columns.

The driest column (Figure 3.4a) evaporated at a low rate that declined only slowly, until it dropped off sharply after 32 days to nearly zero. The other columns showed a more pronounced and gradually diminishing rate of decline of the evaporation rate that more closely resembled the shape often reported for soil-limited (stage-2) evaporation (e.g., Ritchie, 1971). From the difference with the dry column we surmise that early on, the water present in the top of the soil profile evaporated, causing a drying front to penetrate the soil and slow down the evaporation rate. This is somewhat comparable to stage-2 evaporation as discussed in detail by Or et al. (2013), which emerges when in initially wet soil starts to dry out to the degree that a continuous capillary link to the soil surface ceases to exist. After that, evaporation theory predicts the evaporation rate to be proportional to  $t^{-1/2}$  (e.g., Ritchie, 1971) or to  $(a + t)^{-1/2}$  (Or et al., 2013;  $a$  denotes a constant). It should be noted though, that in our case, even the wettest soil columns were relatively dry from the start, and that, unlike soils above a groundwater table, the columns held a finite amount of water.

Interestingly, the evaporation rate suddenly dropped to essentially zero in those cases where the data were collected long enough. This may well have been a reflection of the disappearance of liquid water with mild curvatures of its menisci. At the onset of the drop in the evaporation rate, much of the remaining liquid water probably resided in pendular rings around the contact points of the grains. In pendular rings the opposing signs of the principal radii of curvature (concave along the circumference of the ring and convex across the outside of the ring) can give relatively high water pressures inside the ring, leading to equilibrium vapor pressures that are not that different from that above free water. However, a small loss of water would dramatically increase the curvature of the cross-sectional meniscus while affecting the circumference much less, thus rapidly reducing the pressure of the liquid water and thereby the vapor pressure at equilibrium with that water, before depleting this liquid water altogether. This would result in a sudden drop in the vapor pressure inside the column near the location of the last remaining pockets of liquid water, thereby reducing the vapor pressure gradient driving the vapor flow whilst also exhausting the source that so far replenished the water vapor lost from the column.

We aimed to create conditions in which we would have a combination of liquid water flow and water vapor flow. We anticipated that, as the drying process progressed, liquid water flow would prevail in the lower end of the columns, whereas vapor diffusion would be the dominant transport mechanism for water in the top of the columns. By adding salt to the water in the bottom centimeter of the column, we hoped to be able to observe how high the continuous pathway for liquid water movement reached into the columns. The vaporization plane should be identifiable by an increased salt content. The salt profiles after completion of the experiment are shown in Figure (3.5).



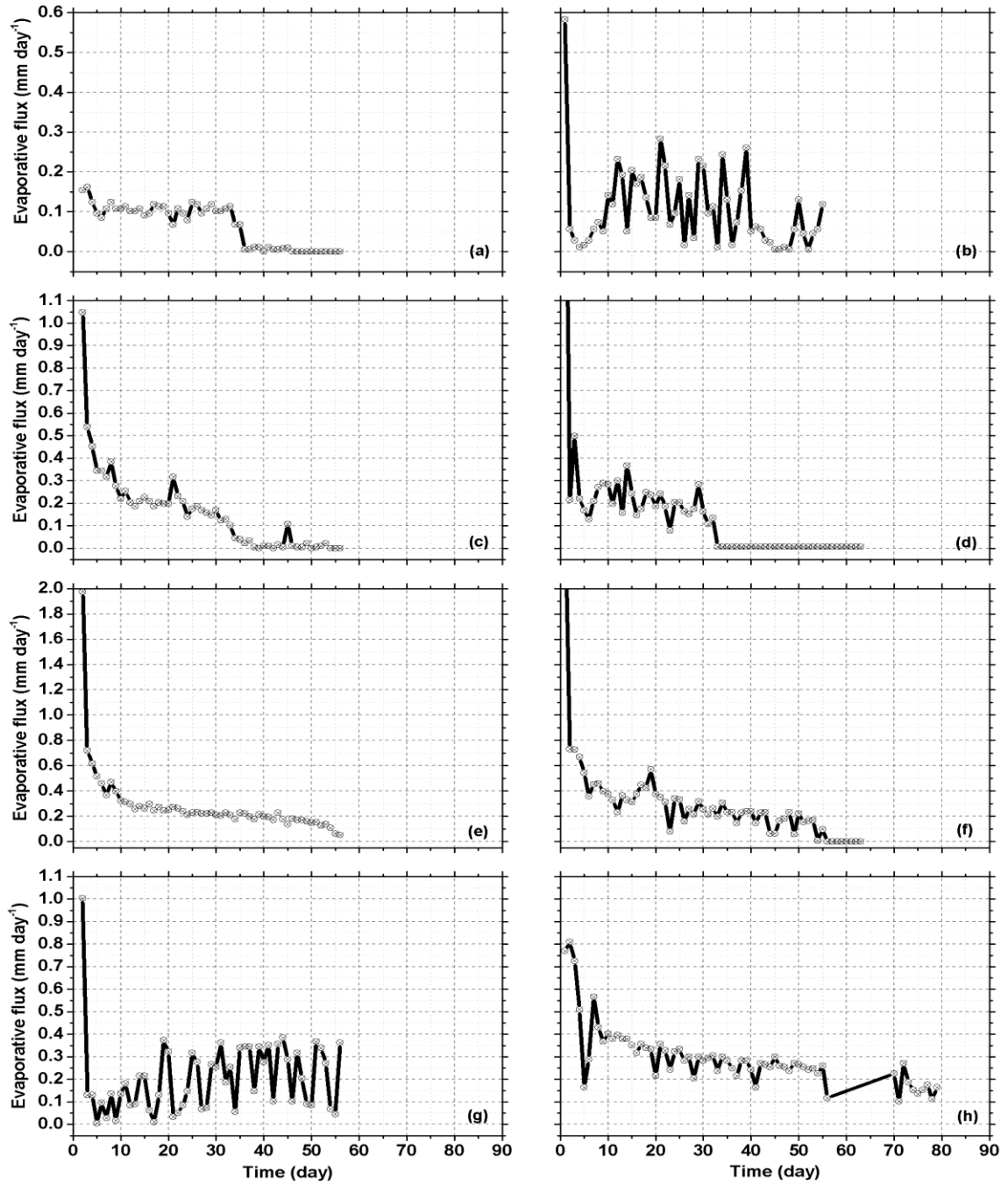


Figure 3.4: Measured evaporative fluxes for the columns with initial volumetric water contents in the top 23.5 cm of: 0.00 (a, b), 0.02 (c, d), 0.05 (e, f), and 0.08 (g, h). The left column presents the data for the soils without salt added to the water in the bottom 1 cm, the right column for the soils with added salt.

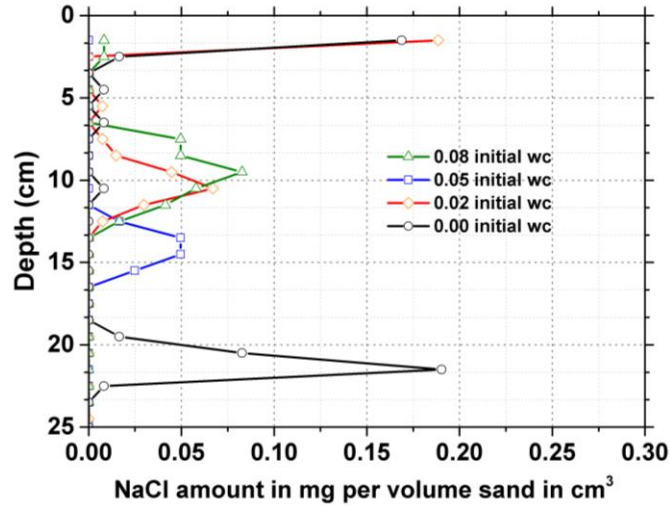


Figure 3.5: The measured amount of NaCl per volume of sand after the completion of the experiment.

All salt profiles provide clear evidence of the existence of a vaporization plane. For the initially dry sand, this plane could only form by capillary rise from the bottom 1 cm. It is therefore the deepest, rising only about 2 cm above the original top of the saturated layer. In the other columns, the initially resident water apparently created a continuum of liquid water that was broken up by a drying front entering from above. The vaporization plane developed below that, and as the water from the bottom centimeter was carried upwards through this liquid continuum it could rise in the liquid phase over a distance between 10 and 15 cm.

For the column with an initial water content of 0.02, the evaporation data discussed above showed that the effect of rapid evaporation from the water resident near the surface did not dominate the early stages of the experiment. Yet, the salt profile indicates that this small amount of initial water significantly affected the formation of the vaporization plane: it is much higher than that of the dry soil, and falls within those of the wetter columns.

Remarkably, a fraction of the water initially residing at the very bottom of the column could rise all the way to the soil surface along a continuous pathway of liquid flow, as evidenced by the elevated salt levels at the soil surface, especially from the two driest columns. We checked the salt profiles of the columns with initial water contents of 0.00 and 0.02 without added salt and could verify that the salt accumulation caused by the salt present in the sand and the tap water led to qualitatively similar profiles as those of Figure (3.5), but with peaks that are an order of magnitude smaller (Figure 3.6).

Thus, this unforeseen accumulation of salt in the top of the columns was not an experimental artefact, and significant amounts of salt did indeed travel over the full length of the column. We can only offer a speculative explanation at this time. The continuity of a liquid phase under conditions that strongly favor evaporation seems possible only if that liquid phase was considerably more saline than the water that initially contained the salt to be able to build up an osmotic potential low enough to reduce evaporation. This in turn implies that the flow above the vaporization plane only started sometime after the formation of that plane so that evaporation had already been effective in increasing the salinity of the remaining liquid water.

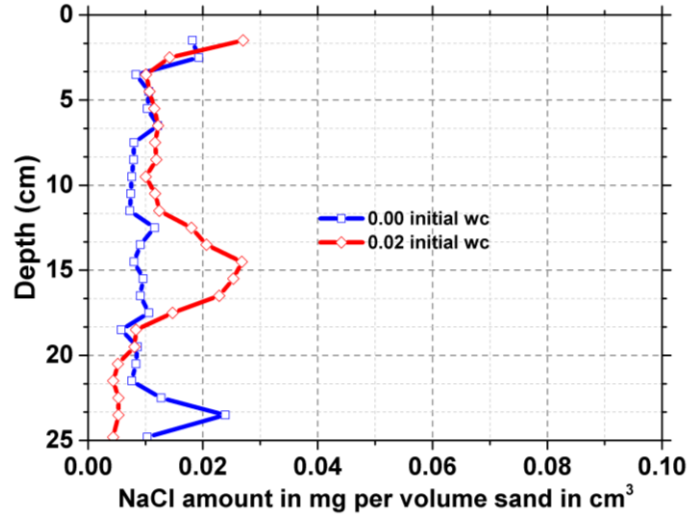


Figure 3.6: The measured amount of NaCl per volume of sand for the columns with the indicated initial water contents without added salt to the water in the bottom 1 cm. All salt originates from the tap water added to the sand and the sand itself.

This leads to the hypothesis that initially, slightly saline water moved upward from the bottom of the column. At the vaporization plane, the water evaporated and left the salt behind. The remaining liquid water became increasingly saline, possibly even saturated. In the air-filled pore space, the water vapor was at equilibrium with the liquid water in the vicinity. The saline solution created a much lower osmotic potential at the depth of the vaporization plane, allowing the water to remain in the liquid phase under conditions where solute-free water would have evaporated. As a consequence of the lowered osmotic potential, the vapor pressure in equilibrium with that solution was lowered, reducing the vapor pressure gradient driving the vapor flow, which slowed down evaporation. The saline water could then slowly flow upwards, driven by the matric potential gradient created by the dry, warm air at the top of the soil column. It apparently reached the top of the column before evaporating, leaving the salt behind at the top of the sample.

This process was much slower than the liquid flow of solute free water: the brine was more viscous, and it only started flowing after much of the water had already left the column, leaving only film flow and corner flow as slow vehicles for liquid movement.

This explanation seems to be consistent with the less pronounced jump in the salt profile near the surface of the wettest column. It stands to reason that in this column the flow of liquid water of low salinity could be sustained the longest, and the brine flow could only get started after much of the liquid water had gone.

### 3.4.2. Fitted parameters

Of the conventional parameterizations, BCO is struggling with the shape of the observed retention curve (Figure 3.2) but does a reasonable job in capture the air-entry value. Surprisingly, VGN does not capture the shape very well either, especially in the wet range. The modification by Ippisch et al. (2006) that lead to VGA brought little improvement. RNA poorly fitted the air-entry value, and power-law shape does not match the observed curve very well, similarly to BCO, on which it is based. FSB gave

the best fit, particularly in the very wet range ( $0 < pF < 1$ ) and in the range of the driest observations ( $2 < pF < 4$ ). Table B.1 presents the fitted parameters for the parameterizations with their units and physical ranges.

### 3.4.3. Simulation results

The model runs with VGA, VGN, and BCO had severe convergence problems and also failed to simulate the extremely dry experimental conditions because the water contents dropped below their fitted residual values. Results are therefore only presented for RNA and FSB. Runs with FSB only converged if we limited the saturated hydraulic conductivity to  $150 \text{ cm d}^{-1}$ . RNA could handle the measured value for  $K_s$ .

#### 3.4.3.1. Liquid water and vapor fluxes

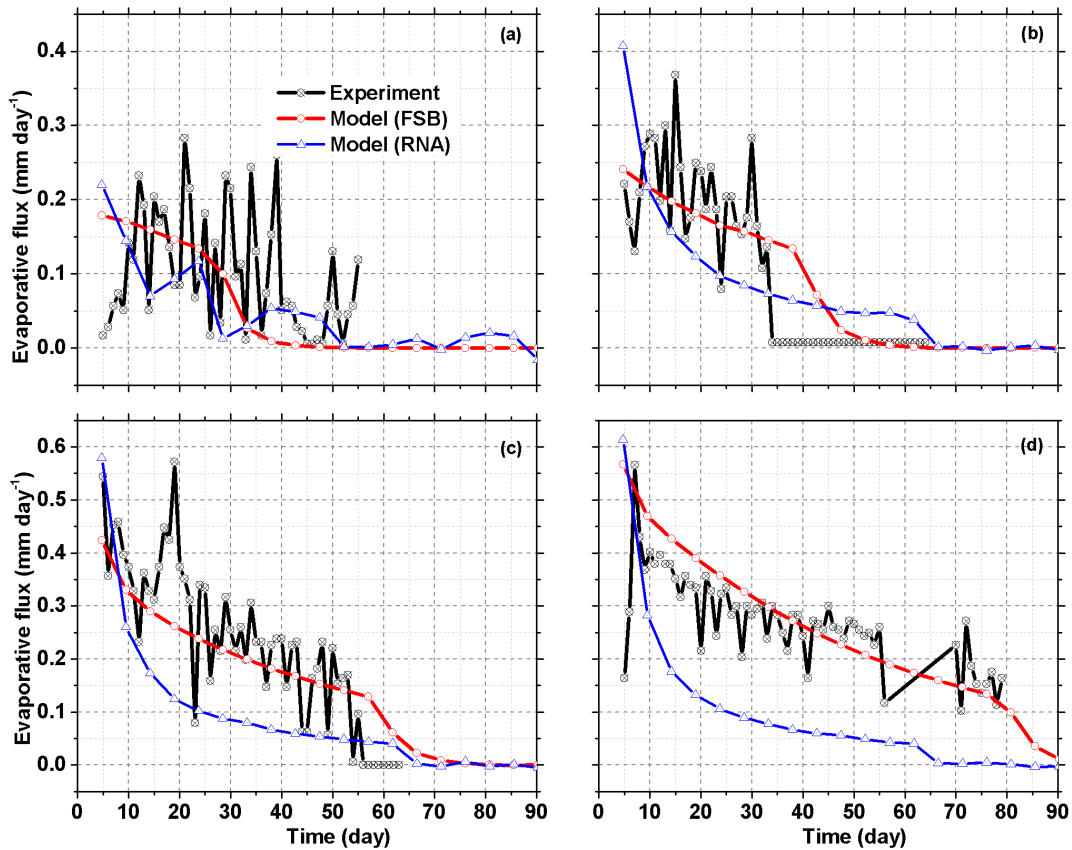


Figure 3.7: Observed and simulated evaporation for columns with initial water contents in the top 23.5 cm of 0.00 (a), 0.02 (b), 0.05 (c), and 0.08 (d). The observations are from the columns with a  $10 \text{ mmol l}^{-1}$  NaCl solution initially saturating the bottom 1 cm of the column.

For the dry column (Figure 3.7a), the model runs with RNA gave slow, non-physical oscillations of the evaporation rate. FSB did better initially, but dropped off to zero evaporation too soon. For the other columns (Figures 3.7b, c, d), both parameterizations generated gradually declining trends in which

the rate of decline slowly decreased, then suddenly increased again until the evaporation rate was essentially zero. In all cases, FSB outperformed RNA. FSB captured the trend rather well, and was not too far off predicting when the drop off to zero occurred that is clearly visible in the data for the columns with water contents of 0.02 and 0.05.

The evaporation fluxes at the top of the columns were generated by an interplay of liquid water and vapor fluxes inside the columns. The model simulations permit these fluxes to be examined side by side by looking at the profile of either flux at different times. To allow for a better comparison between columns with different initial water contents, we scaled the time by the time it took for the liquid water flux to become zero across the entire depth (Table 3.2).

Table 3.2: The time (d) at which the simulated liquid flux became zero throughout the columns for different initial water contents and soil hydraulic parameterizations.

Parameterization	Initial volumetric water content			
	0.00	0.02	0.05	0.08
FSB	54.63	59.38	64.13	64.13
RNA	26.13	40.38	57.00	78.38

All plots (Figures B.1-B.8) show a sharp vaporization plane separating a region with liquid water flow only below from a region with vapor flow only above. In all columns, these planes moved down gradually as the liquid water supply was depleted. As they did, the magnitude of the fluxes gradually decreased. In terms of solute transport and precipitation of salt, this should lead to a gradual deposition of salt over that part of the soil profile that was below the vaporization plane from the start, with the amount of salt decreasing with depth.

As long as there is liquid water present, the vapor flow rate above the vaporization plane is approximately constant with depth, reflecting the fact that there is nearly zero storage of water vapor in the profile and no liquid water remaining to evaporate. The liquid water flux increases higher up in the section of the profile below the vaporization front, indicating that the profile was drying everywhere below the vaporization plane. The more linear the liquid flux rate changed with depth below the vaporization plane, the more uniform was the water loss distributed over that section of the column.

There are minor to very large numerical oscillations in the vapor flux densities, but these did not affect the mass balances. Nevertheless, for vapor flow calculations in more natural settings these could become a point of concern.

For FSB, the depth of the vaporization plane at a scaled time of roughly 0.15 varies from 16 cm for the initially dry profile to 6 cm for the profile with an initial water content of 0.08. For RNA, the range was from 6 to 3 cm. The magnitude of the both liquid water and vapor fluxes was comparable for FSB and RNA early on in the process for all initial water contents, with the difference being largest in the wetter columns. These early fluxes in the wettest columns were roughly twice as large as those in the dry columns. As time progressed and the columns dried out, the liquid and vapor fluxes decreased considerably faster for RNA than they did for FSB.

In summary, FSB and RNA produced fluxes as a function of the initial water content and in their change with time that had trends in similar directions, and which made sense physically. The same holds for the evolution of the vaporization front. The rate of change and the dynamics of the vaporization front were distinctly different though, pointing to a marked effect of the choice of parameterization on the

dynamics of coupled liquid-vapor flow in dry soils. The comparison of the simulated evaporation rates with the observations indicates that FSB better captured the overall outcome of these dynamics.

### **3.4.3.2. Simulated and calculated pF values**

The temperature proved to be excessive for the water content sensors (even though it was within the manufacturer's specifications), so we derived matric potentials from the observed relative humidities in the soil gas phase. Figures 3.8 and 3.9 show the observed and simulated pF values at selected depths with time.

The observations at depths  $\geq 17$  cm only became useful after the soil had dried somewhat because air humidity sensors are not very sensitive in moist soils. Usually, the recorded relative humidity in that range was 1.0, which gave a pF of  $-\infty$ . But as the soil dried, a rapid increase in the pF was recorded that closely approximated the values recorded at 5 cm depth in all cases. The simulations did not perform very well reproducing the observations. This may be in part because the vapor diffusion was sufficiently effective to reduce the gradient in the vapor pressure more effectively than liquid flow could do so for the matric potential gradient (compromising the assumption of instantaneous local equilibrium between the matric potential and the vapor pressure in HYDRUS-1D), but it may also truly reflect deviations between the model and the experiment.

The experimental data showed a slight change in the slope, where the increase in the pF slightly slowed down before speeding up again before leveling off as the soil loses all its water. The timing of this slight slow-down corresponded to the drop in the evaporation rate visible in Figure 3.4. In the observations, this change of slope occurred nearly simultaneously throughout the columns, and the simulations captured this well, but the model runs gave a much more pronounced effect. Again, this may be related to the limited sensitivity of the sensors. Nevertheless, it is encouraging to see that the model was able to capture this phenomenon at least qualitatively. The runs with FSB timed this occurrence reasonably well, especially for the wetter columns (Figure 3.8c, d). The runs with RNA (Figure 3.9) underestimated the effect of the initial water content on the time when this phenomenon occurred, predicting them at 50-60 d for all water contents. This is consistent with the better performance of FSB in predicting the drop in the evaporation rate.

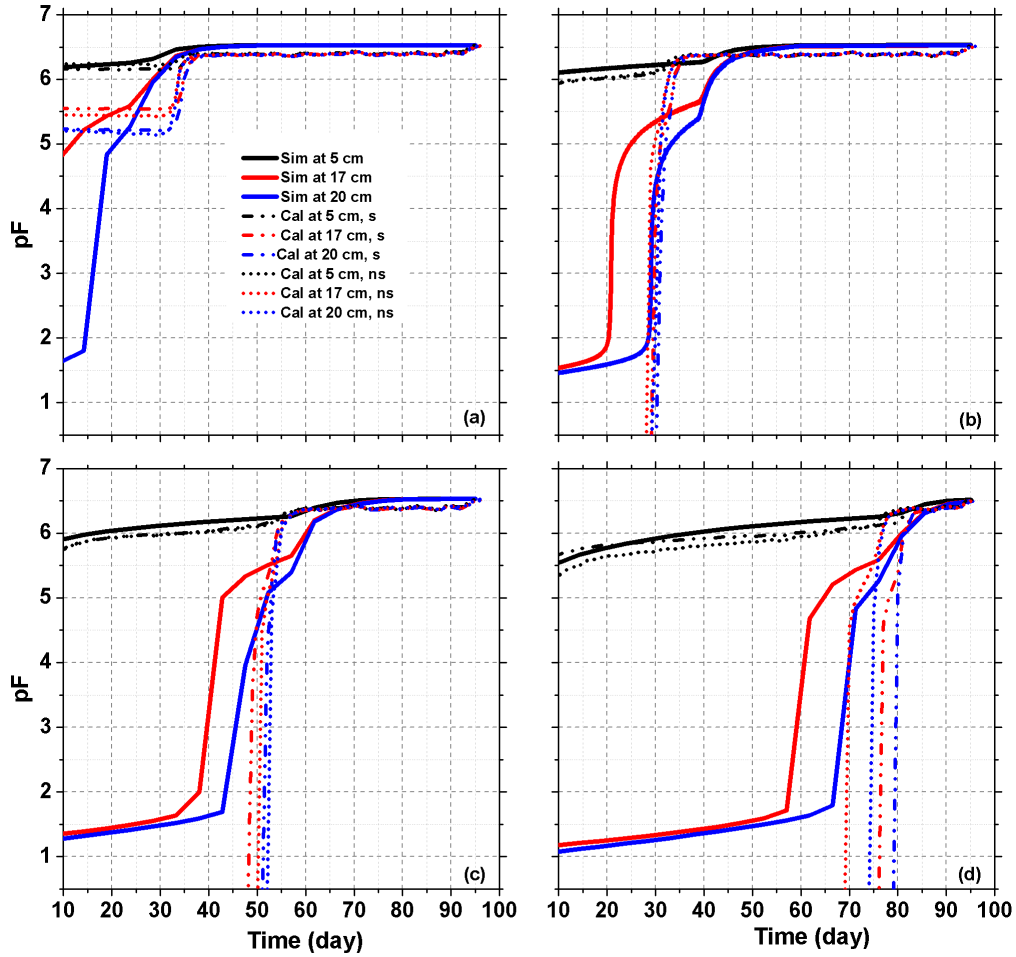


Figure 3.8: Simulated and calculated pF values for the FSB parameterization at three depths for columns with an initial water content of 0.00 (a), 0.02 (b), 0.05 (c), and 0.08 (d). The vertical drop-off in the observed pF values (labeled cal...) reflect a relative humidity of 1 observed at the times preceding the drop-off. When converted to pF this results in a value of  $-\infty$ , causing a steep rise towards the first observation of a relative humidity  $< 1$ . The labels 's' and 'ns' refer to columns with and without added salt in the bottom 1 cm.

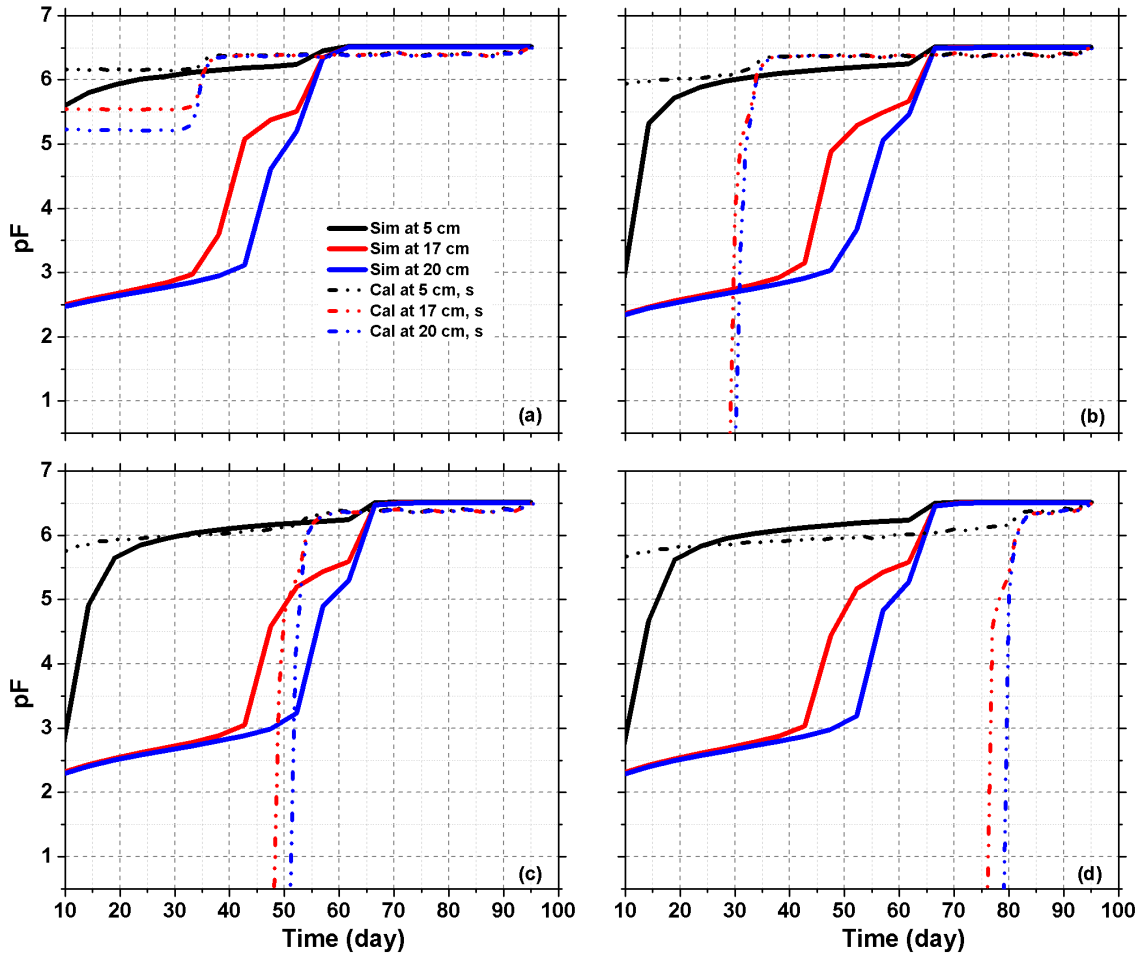


Figure 3.9: As Figure 3.8 but for the RNA parameterization.

### 3.4.3.3. Simulated and measured salt profiles

At the end of the simulated period we converted the salt concentrations and the water contents to amounts of salt per volume. Figure 3.10 shows the observed and simulated salt distributions. The simulated gradual distribution of salt with relatively high concentrations higher up in the profile, deposited when fluxes were largest as expected from the simulated fluxes in Figs. B.1–B.8, is confirmed by Figs. 3.10b and c, but is not supported by the data (Figure 3.10a). Both parameterizations predicted the peak amounts of salt for different initial water contents too close to one another. For the dry soil, FSB better predicted the depth of the vaporization plane than RNA. For the wetter columns, neither parameterization performed very well.

The surprising concentration of salt at the top of the profile could not be reproduced by HYDRUS-1D. Hydrus does not model the effect of salt on the water potential or the vapor pressure, so if the explanation we presented in section 3.4.1 has merit, HYDRUS-1D would be unable to model the processes that caused it.



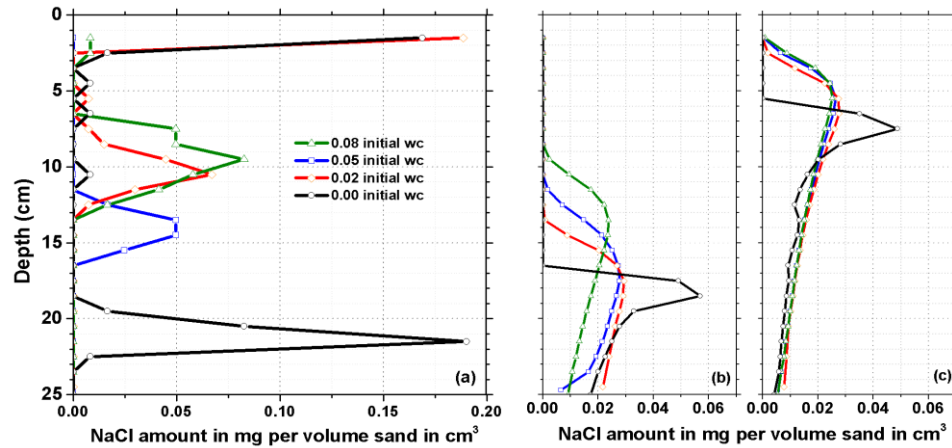


Figure 3.10: The distribution of NaCl in the various columns at the end of the experiment as to the observed (a) and according to the model runs using FSB (b) and RNA (c).

### 3.5. Summary and Conclusions

We observed the drying process in shallow columns that were closed at the bottom. The HYDRUS-1D model with the capability to solve water flow, vapor diffusion, and heat flow in unsaturated porous media was able to capture several intricacies of coupled liquid-vapor flow, including the rapid drop in evaporation rate when the columns became very dry, and the corresponding change in the rate of change in the pF. There were numerical instabilities in the vapor flux though, difficulties achieving convergence in the solution of the liquid water flow that did not permit us to test the entire set of soil hydraulic parameterizations we intended to evaluate. These problems will probably be less severe for natural soils instead of the extreme porous medium used in this study.

There was a clear effect of the choice of parameterization on the simulated fluxes, with FSB outperforming RNA. More testing (including field testing and long-term simulations) is required to see if we need to further expand the arsenal of soil water retention and hydraulic conductivity functions, and if any of these functions performs adequately for simulations of groundwater recharge.

The experiments revealed that there appears to be a mechanism that delivers salt above the vaporization plane all the way to the soil surface. This mechanism can only be tentatively explained at this time, and cannot be modeled when the solute concentration does not affect the soil water potential or the equilibrium vapor pressure.

## Chapter 4

### 4. Water, heat, and vapor flow in a deep vadose zone under arid and hyper-arid conditions: a numerical study.

#### Abstract:

Quantifying groundwater recharge is very difficult. One reason is data scarcity: reliable weather records are often lacking in remote areas, and the soil properties over the entire extent of the often very deep vadose zone are usually unknown. Another reason is the difficulty of modeling the intricately coupled relevant processes over extended periods of time.

In the presence of this myriad of problems, we focused on the latter: coupled flow of liquid water, heat, and water vapor in deep vadose zones. We limited ourselves to the simulation of a 1-dimensional profile of an unvegetated 100 m uniform vadose zone to see the role of wet and dry seasons on the dynamics of ground water recharge, the potential role of water vapor flow and the way the atmospheric input signal travels downward through the vadose zone in an arid and a hyper-arid climate for two soil hydraulic parameterizations suitable for dry conditions. The issue of data scarcity was resolved by using numerically generated rainfall records combined with a simple model for annual and daily temperature fluctuations.

The choice of parameterization had a very large effect on simulated groundwater recharge: under the arid/hyperarid scenarios, a Brooks-Corey-based parameterization converted 4.8%/1.6% of rainfall to recharge, whereas one based on van Genuchten only converted 1.9%/1%. A reduction in the mean annual rainfall resulted in a much stronger reduction of the groundwater recharge. The effect of including vapor flow and/or the effect of the geothermal gradient was noticeable but inconsequential in comparison to the choice of parameterization. The deep unsaturated zone strongly damped and delayed the atmospheric signal: at several tens of meters of depth, the delay with which wet and dry periods affected vertical fluxes was several decades, and the annual flux rate at any given year averaged the rainfall signal over several years up to a few decades.

#### 4.1. Introduction

Arid and semi-arid regions are expanding noticeably and currently represent about 30% of the global terrestrial surface area (Dregne, 1991). The effects of water scarcity in semi-arid and arid regions on human lives are felt with increasing severity by local populations. Groundwater is generally the main or even the only resource to meet the expanding urban, industrial, and agricultural water requirements (de Vries and Simmers, 2002; Scanlon, 2006, see section 1.1 for details).

The accurate evaluation of basin scale water budgets in (semi-)arid regions requires a quantitative understanding of water movement in vadose zones with depths ranging from several meters to hundreds of meters (Walvoord and Scanlon, 2004). The soil water dynamics in space and time depend strongly on the weather (rainfall, potential evapotranspiration, temperature, radiation), vegetation cover, land use, and

the physical properties of the soil and their spatial variation (Rosenbaum et al., 2012). The spatial and temporal distribution of soil moisture in turn affects many environmental processes, often in a non-linear way (Western et al., 2002). In deep vadose zones under dry climatic conditions, water movement in the vapor phase may be significant. The importance of vapor flow is under debate, with some attributing only a limited role to it (e.g., Milly, 1984), while others claim a significant effect on groundwater recharge (e.g., Barnes and Turner, 1998; de Vries and Simmers, 2002). Goss and Madliger (2007) found from 3-month *in situ* data of soil relative humidities and temperatures that the vapor transport is dominant only in the top soil layer and under very dry conditions. In a simulation over 16000 years with constant boundary conditions, Walvoord and Scanlon (2004) found a dominant effect of vapor flow in a relatively moist desert soil (volumetric water content  $> 0.15$ , as estimated from their graphed matric potentials) if the effect of simultaneous condensation and evaporation from different air-water interfaces of the same body of pore water was taken into account (Cass et al., 1984).

The parameterization used for the soil water retention curve should represent the dry end of the curve well. That section of the curve obviously is relevant for water flows during the prevalent dry conditions in (semi-) arid regions. The dry end of the curve also represents the condition under which the gas phase occupies most of the pore space, and therefore is highly relevant for vapor movement. Paradoxically, the very wet end of the curve is also important because rainfall on dry soils tends to lead to sharp wetting fronts with high water contents behind them because the infiltrating water needs to overcome the water-entry matric potential. The influence of the soil water retention curve on the soil hydraulic conductivity near saturation can be pathological (Durner, 1994), but the mathematical reasons for that are well understood and can be remedied (Durner, 1994; Ippisch et al., 2006). Several authors have developed parametric expressions that seek to improve the fit in the dry end (e.g., Rossi and Nimmo, 1994; Fayer and Simmons 1995; Peters, 2013; see also the review by Khlosi et al., (2008). Several of these alternative expressions were tested in the Chapter 2.

The relationship between rainfall and recharge is of considerable interest. Wu et al. (1996) could relate the annual recharge to the amount of rainfall in clusters of rainfall events within the same year with a simple linear relationship when the amount of rainfall exceeded a threshold value. This method worked for a groundwater level at 4.5 m below the soil surface. Turkeltaub et al. (2015) carried out an elaborated monitoring campaign in a 20 m-deep vadose zone in a Mediterranean climate with an average annual rainfall of 450 mm. They found that seasonal recharge was driven by the rainfall in rainy season of the previous year. For deeper vadose zones, the signal can be expected to fade out to a more or less constant recharge rate.

For predictive purposes, it is necessary to have access to long-term rainfall and temperature records in order to simulate scenarios over several decades to have sufficient model data on which to base rational decisions. Such records are generally missing in semi-arid regions. Furthermore, climate change might render any existing records of limited use for predictive purposes. It will therefore be necessary to have the ability to generate synthetic rainfall records based on parametric rainfall models in which the future values of the parameters or at least the trend of their change can be gestimated.

This chapter examines through numerical modeling of long periods of time the movement of liquid water and water vapor in a deep vadose zone, accounting for the effect of the geothermal gradient, and considering the coupling between the flow of liquid water, heat, and water vapor. The main objective is to assess the role of wet periods and droughts in an arid and a hyper-arid climate in the generation of ground water recharge, the potential role of water vapor flow, and the behavior of the atmospheric input signal traveling downward in deep vadose zones for two soil hydraulic parameterizations.

## 4.2. Materials and Methods

### 4.2.1. Rainfall data

Artificial rainfall records were generated using a modification of the Bartlett-Lewis model originally proposed by Rodriguez-Iturbe et al. (1988). In this model, the intervals between starting times of rain storms have an exponential distribution. Within each storm, rain cells of variable duration and with different but constant rainfall rates occur. The total rainfall rate at any given time equals the sum of the rainfall rates of all rain cells that are active at that time. The modified model we used had a Gamma-distributed parameter  $\eta$  that defined the exponential distribution of the cell duration in a storm. Indirectly,  $\eta$  also governed the duration of storms and the intervals between the times at which rains cells within a storm started. The rainfall rate in the cells was also Gamma-distributed. Because the Gamma distribution can occasionally produce unrealistically long-lasting rain cells, a truncated version was used that rejected values of  $\eta$  below a threshold. Pham et al. (2013) give full details of this truncated modified Bartlett-Lewis model with Gamma-distributed rainfall rates (TBLG model in their terminology).

We used this model to generate the 120 years of rainfall data, which we aggregated into daily sums. To do so, the model required 8 parameters for each of the user-prescribed periods into which a year was divided. We chose a dry period (December – September) and a wet period (October– November). We used two scenarios with average annual rainfall amounts of 30.63 cm (scenario (1), Figure 4.1a) and 7.88 cm (scenario (2), Figure 4.1b) that differed in the duration of the dry periods between storms and the distribution of  $\eta$ . The input parameters for both scenarios are given in Table 4.1.

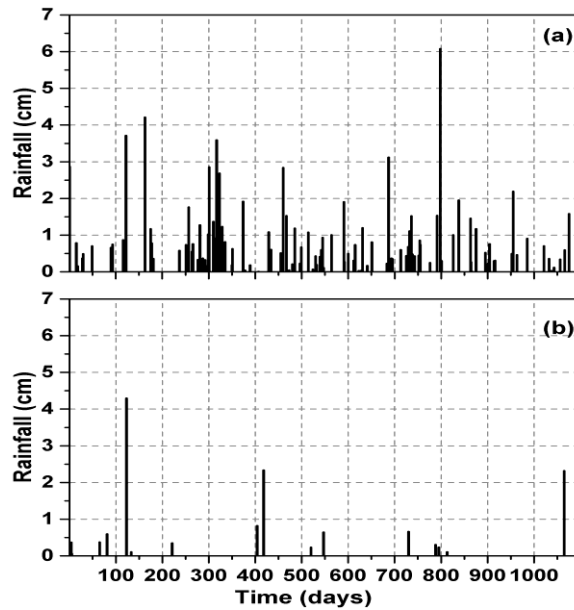


Figure 4.1: Daily rainfall data for a 3-year sample from the 120-year record. Panels (a) and (b) show the wetter scenario (1) and the drier scenario (2), respectively.

#### 4.2.2. Temperature data

Artificial mean annual and minimum ( $T_{MIN}$ ; °C) and maximum ( $T_{MAX}$ ; °C) daily temperature data were generated in order to compensate for the lack of temperature data for multiple centuries using the following simple model:

$$T_{MIN} = \bar{T} + A \left\{ \sin \left[ \frac{2\pi(\varphi + t)}{365.25} \right] \right\} + \sigma_m N_1(0,1) \mp e^{\mu_f + \sigma_f N_2(0,1)} \quad (4.1)$$

The first term  $\bar{T}$  (°C) of the right-hand side gives the long-term average temperature. The second term superimposes on the average a sinusoidal annual fluctuation around the mean with amplitude  $A$  (°C) and temporal shift  $\varphi$  (d). Time is represented in this term by  $t$  (d). If  $t = 0$  at 0.00 hrs on January 1<sup>st</sup> of a given year,  $t$  should have the value  $x - 0.5$  to represent day  $x$  since  $t = 0$ , leading to a series of incremental values of  $t$ :  $t = 0.5, 1.5, 2.5, \dots$ . The third term adds normally distributed random noise to the daily temperatures with zero mean and standard deviation  $\sigma_m$ . Thus, the first three terms generate a value for the mean temperature of the day corresponding to  $t$ . The final term creates a lognormally distributed range between the minimum and maximum temperatures of that day, with  $\mu_f$  and  $\sigma_f$  the mean and standard deviation of the natural logarithm of that distribution.  $N_1(0,1)$  and  $N_2(0,1)$  represent independent standard normally distributed variates. The calculated value of the final term is subtracted from the average temperature of that day to arrive at the minimum and added to find the maximum temperature.

Table 4.1: The parameters values of the the rainfall model with their units for each period. The periods are indicated by their starting times in the final column. For parameter  $\lambda$  the first value refers to the wetter scenario (1), and the second to the drier scenario (2).

$\lambda$ (d <sup>-1</sup> )	$p$ (mm d <sup>-1</sup> )	$\delta$ (d mm <sup>-1</sup> )	$\alpha$ (-)	$\nu$ (d)	$\kappa$ (-)	$\varphi$ (-)	$\varepsilon$ (d <sup>-1</sup> )	Starting time (d)
0.09 0.02	70	0.008	40	0.015	0.6	0.5	2.22E-11	0.0
0.5 0.3	60	0.0045	35	0.009	0.2	0.1	9.00E-9	273
0.09 0.02	70	0.008	40	0.015	0.6	0.5	2.22E-11	334

$\lambda$ : parameter of the exponential distribution of intervals between storm starting times

$p$ : shape parameter of the Gamma-distribution of the rainfall rate of a rain cell

$\delta$ : rate parameter of the Gamma-distribution of the rainfall rate of a rain cell

$\alpha$ : shape parameter of the Gamma-distribution of  $\eta$ , the parameter of the exponential distribution of the duration of rain cells in a storm

$\nu$ : rate parameter of the Gamma-distribution of  $\eta$

$\kappa$ :  $\kappa\eta$  is the parameter of the exponential distribution of intervals between rain cell starting times in a storm

$\varphi$ :  $\varphi\eta$  is the parameter of the exponential distribution of the duration of a storm

Fourteen years of daily temperature data were taken from the NOAA data base (<http://www.ncdc.noaa.gov/cdo-web/>) for a station in Riyadh city (Saudi Arabia) between January 1, 1985

and December 31, 1993. We fitted the first two terms (mean and annual fluctuation) of Eq. (4.1) to those temperature to estimate  $\bar{T}$ ,  $A$ , and  $\varphi$ . We selected the values of  $\sigma_m$ ,  $\mu_f$ , and  $\sigma_f$  by trial and error to give reasonable results.

### 4.2.3. Numerical modelling

The open source code HYDRUS-1D (Šimůnek et al., 2013, 2016) was used to solve the coupled liquid water, water vapor, and heat transport equations within a 100 m deep vadose zone for a period of 120 years. Liquid water flow was described by Richards' equation. Water vapor movement was assumed to be diffusive and driven by vapor pressure differences. The local vapor pressure was assumed to be in equilibrium with the matric potential of the liquid water. The osmotic potential was assumed to be negligible. Water vapor can condensate onto one air-water interface and water can evaporate simultaneously from another interface of the same body of liquid water. This leads to an apparent transport of water vapor that is faster than strictly diffusive transport in the gas phase. This vapor transport enhancement effect was parameterized according to Cass et al. (1984), and was computed internally by the model. The thermal conductivity was chosen according to Chung and Horton (1987) and the heat transport parameters were set to the default values of loamy soils (Šimůnek et al., 2013, p. 75).

#### 4.2.3.1. Initial and boundary conditions of the numerical model

An atmospheric upper boundary condition for liquid and vapor transport was set: during dry periods the matric potential at the soil surface was set to -40000 cm; during rain: prescribed flux density equal to the daily rainfall rate. At the lower boundary, zero matric potential and saturated water vapor pressure were implemented. For the upper boundary condition to the heat flow equation, a daily fluctuating sinusoidal air temperature with a temperature range generated by Eq. (4.1) was specified on input see (Table 4.2). Radiative heat input during the day and heat loss during the night were not considered. At the lower boundary we specified a constant temperature of 29.8 °C, consistent with a geothermal gradient of 35 °C km<sup>-1</sup> (Walwoord and Scanlon, 2004).

Table 4.2: Summary of parameter values of the temperature Eq. (4.1).

$\bar{T}$ (°C)	$A$ (°C)	$\varphi$ (d)	$\sigma_m$ (°C)	$\mu_f$ (-)	$\sigma_f$ (-)
26.3	11.0	255.84	2.67	6.41	0.27

As the initial condition, a unit gradient condition was imposed for the liquid water flow in the top 98 m of the profile. The matric potential was selected to create a strictly gravity-driven flux density of 30% and 10% of the average annual rainfall rate for the wet and dry rainfall scenarios, respectively. In the bottom 2 m, the matric potential was linearly interpolated between the values at 98 and 100 m depth (the latter being zero). as hydrostatic equilibrium. The model then ran through the 120-year atmospheric forcing. The resulting profile of matric potential and temperature was used as the initial condition for the warm-up period of the model (240 years in case of the wettest scenario and 720 years in case of the driest one) during which the weather record was repeated, which was then followed by the 120-year cycle we used for analysis. The matric potentials defined in this way also provided the initial vapor pressure profile

through the assumed local equilibrium between the two variables. The initial temperature varied linearly between 26.31 °C at the soil surface and 29.81 °C at 100 m depth.

#### 4.2.4. Soil water retention and hydraulic conductivity curves

The soil profile was uniform. We adopted the retention data (Figure 4.2) and the saturated hydraulic conductivity (106.1 cm d<sup>-1</sup>) for a sandy loam (Royal soil) from Rossi and Nimmo (1994). In Chapter 2 we reviewed various retention function parameterizations and found that the expression of Fayer and Simmons (1995) (Eq. (2.16a)) based on the Brooks-Corey function (1964) to be suitable for dry soils (denoted FSB in the remainder of the chapter).

Observations of retention data often show an inflection point in the retention curve, but the power-law term for the mid-range of the FSB curve cannot reproduce that. The retention curve according to van Genuchten (1980) has a reflection point, but also an undesirable asymptote in the dry range and a non-zero slope  $d\theta/dh$  at saturation, causing non-physical behavior of the hydraulic conductivity near saturation (Durner, 1994; Ippisch et al., 2006). We therefore combined the modification of Ippisch et al. (2006) that fixed the problem near saturation with the junction model of Rossi and Nimmo (1994), which replaced the asymptotic dry end by a logarithmic branch. We denote this parameterization by RIA:

$$\theta(h) = \begin{cases} 0, & h \leq h_d \\ \theta_s \beta \ln\left(\frac{h_d}{h}\right), & h_d < h \leq h_j \\ \theta_s \left(\frac{1 + |\alpha h|^n}{1 + |\alpha h_{ae}|^n}\right)^{\frac{1}{n}-1}, & h_j < h \leq h_{ae} \\ \theta_s, & h > h_{ae} \end{cases} \quad (4.2)$$

where subscript  $d$  denotes the value at which the water content reaches zero, and subscript  $j$  indicates the value at which the logarithmic and sigmoid branch are joined. Parameter  $\beta$  is a fitting parameter, just as parameters  $\alpha$  [L<sup>-1</sup>] and  $n$ , which determine the shape of the sigmoid branch (van Genuchten, 1980). By requiring that the function and its first derivative are continuous at  $h_j$ , the number of parameters can be reduced from seven to five.

The two selected parameterizations were combined with Mualem's (1976) model for the soil hydraulic conductivity. Neither of them is implemented in HYDRUS-1D. We therefore tabulated them and provided these tables through the input file MATER.IN to the model. The unit gradient initial condition mentioned translated into a matric potential of -257.1 cm for FSB and -569.7 cm for RIA under scenario 1, and of -408.8 cm for FSB and -917.8 cm for RIA under scenario 2.

#### 4.2.5. The relationship between rainfall and recharge

In view of the work by Wu et al. (1996) and Turkeltaub et al. (2015) discussed above, we expect for our much deeper vadose zone that the delay between rainfall and the recharge it generates will be several years at least, and that annual sums of rainfall will suffice to determine the relationship between rainfall and recharge. Following the reasoning by Wu et al. (1996) and Turkeltaub et al. (2015) it

appeared plausible that recharge at 100 m depth might depend on the occurrence of clusters of wet years. We therefore applied a moving-average filter to the time series of annual rainfall. We divided the total time period into complete 118 hydrological years (starting at day 273, see Table 4.1) and then ran the averaging window over the sequence of 118 annual rainfall sums ( $T_{MIN}$ ; °C). The filtered rainfall signal is calculated as:

$$\bar{P}(x, n, k) = \frac{1}{2k+1} \sum_{i=x-n-k}^{x-n+k} [P_{ANN}(i)] \quad (4.3)$$

where  $\bar{P}$  [L] denotes the average annual rainfall during the time window of the filter,  $P_{ANN}(i)$  [L] is the total rainfall in year  $i$ ,  $x$  denotes the year for which the recharge is considered,  $n$  is the time lag in number of years between year  $x$  and the center of the time window of the rainfall filter, and  $k$  defines the width of the time window (equal to  $2k + 1$ ), with the requirement that  $0 \leq k \leq n$ .

We regressed the annually accumulated downward fluxes at 10, 20, 60, and 100 m depth against the rainfall signal filtered according to Eq. (4.3). The resulting correlation coefficients  $r^2$  between the annual downward flux and  $\bar{P}(x, n, k)$  were computed for a range of combinations of lag times (by varying  $n$ ) and averaging window widths (by varying  $k$ ). The resulting  $r^2(n, k)$  maps gave an indication of the strength of the correlation and the sharpness with which the lag and the window width could be determined, and were also used to find the  $(n, k)$  pair that maximized  $r^2$ . The corresponding value of  $n$  gave the time delay in years of the downward flux response to rainfall, while  $2k + 1$  was the time period over which the soil water flux signal averaged the rainfall signal.

## 4.3. Results and Discussion

### 4.3.1. Fitted parameters

Figure 4.2 shows the fitted retention curves, and Table 4.3 gives the corresponding parameter values. The wet, mid-, and moderately-dry range ( $pF < 4$ ) were clearly fitted better by RIA. Note that in the wet end, the observations reflect the average water content in a soil cylinder and the fitting procedure accounted for a non-uniform water content over this height interval. The cylinder height was not reported so we assumed a height of 5.0 cm. The apparent deviations between the fits and the observations near the air-entry value are caused by the point-scale nature of the fitted equations and the vertical averaging of the observations. In the dry range there is some evidence of mild bimodality that neither of the unimodal parameterizations was able to capture.



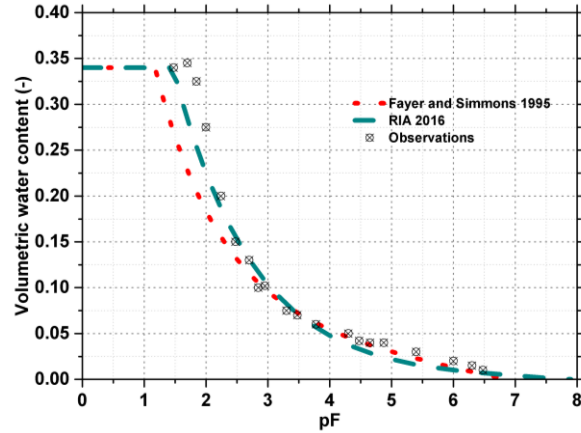


Figure 4.2: Retention data and fitted parameterization according to Fayer and Simmons 1995 (Eq. 2.16a) and RIA (Eq. (4.2)).

Table 4.3: The fitted parameters with their units and physical range for FSB and RIA. The parameters are given in equations (2.16a) and (4.2) in the main text.

Parameterization	Fitted parameter	Unit	Range	Fitted values
FSB	$\theta_s$	-	$\theta_a - 1$	0.340
	$\theta_a$	-	$0 - \theta_s$	0.089
	$h_{ae}$	cm	$h_d - 0$	-15.0
	$\lambda$	-	$0 - \infty$	0.437
RIA	$\theta_s$	-	$0 - 1$	0.339
	$h_{ae}$	cm	$h_j - 0$	-29.3
	$h_j$	cm	$h_d - h_{ae}$	-3.275E+06
	$\alpha$	$\text{cm}^{-1}$	$0 - \infty$	0.999
	$n$	-	$1 - \infty$	1.337

### 4.3.2. Simulation results

Test calculations with isothermal flow showed that ignoring the thermal conditions led to an error up to 10% in the total groundwater fluxes. Thus, the effect of the geothermal gradient and the temperature fluctuations is small but not insignificant.

#### 4.3.2.1. Wetter scenario (1)

##### 4.3.2.1.1. Signal propagation in the unsaturated zone

The simulated downward fluxes for the FSB parameterization and the wetter rainfall scenario show a clear propagation of wet and dry periods down the soil profile (Figure 4.3, top and bottom panel). At 10 and 20 m depth, clear peaks in the downward flux density can be distinguished (Figure 4.3, central panel). At 60 m depth, two peaks can be readily associated with the two wettest periods in the rainfall record. As explained above, the 120 year rainfall record was run for several cycles, and with the help of

the map in the bottom panel the early peak at 60 m can be connected to the period with heavy infiltration 105 to 115 years into the previous cycle. The second peak is associated with infiltration between years 57 to 66. The latter period produces the series of peaks around year 66 (10 m), 70 (20 m), 90 (60 m), and 110 (100 m), that illustrates the delay and dampening of the signal with depth. Similarly, the period of reduced infiltration during years 0 – 23 resulted in flux minima around year 15 (10 m), 27 (20 m), 58 (60 m), and 90 (100 m). The flux peaks tend to remain more distinct and move downward considerably faster than the drought signal.

The RIA parameterization leads to much faster attenuation of the signal: at 60 m the flux density is nearly constant in time (Figure 4.4, central panel) The slope of the signals generated by periods of low and high infiltration (Figure 4.4, bottom panel) is less steep than for FSB, indicating that the signal travels down the profile at lower speed. The minima and maxima in the downward flux at 10 and 20 m depth (Figure 4.4, central panel) are less pronounced than those for FSB, especially at 20 m depth. The arrival times of the minima and maxima that could be distinguished at 10 and 20 m depth differed from those for FSB by one year at most, so the difference in the velocity of the signal evident from the bottom panels of Figures 4.3 and 4.4 manifests itself at larger depths.

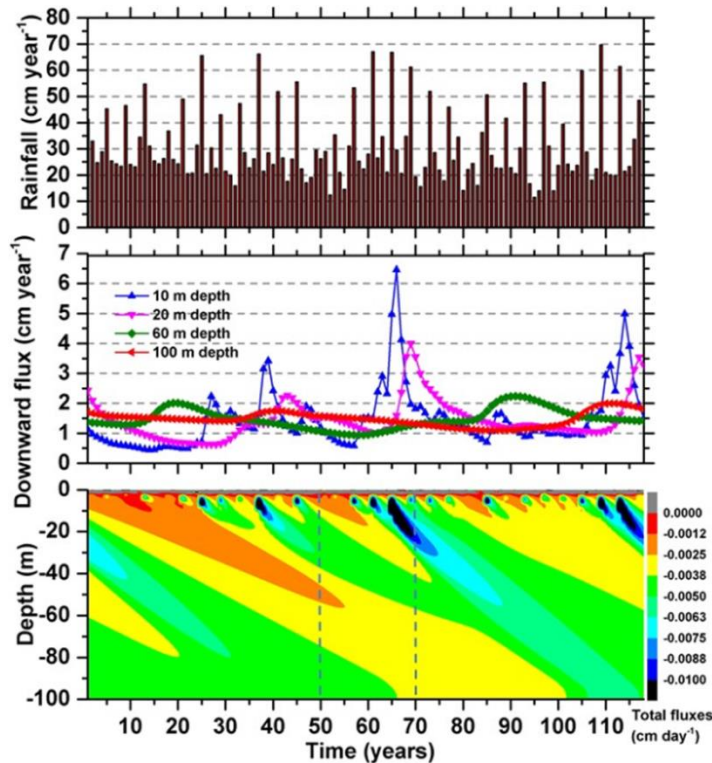


Figure 4.3: Annual rainfall amounts (top panel), the flux densities (positive downward) at selected depths (central panel) and the flux density map of the depth-time domain for the FSB parameterization (bottom panel, in which upward fluxes are positive, consistent with the vertical coordinate). The flux densities are comprised of liquid water and water vapor flux densities (the latter converted to its liquid water-equivalent) for scenario 1. The dashed verticals refer to soil profiles at 50 and 70 years (see Figures C.1 and C.3). The years plotted are hydrological years, starting at the beginning of the wet season (day 273 of non-leap years).

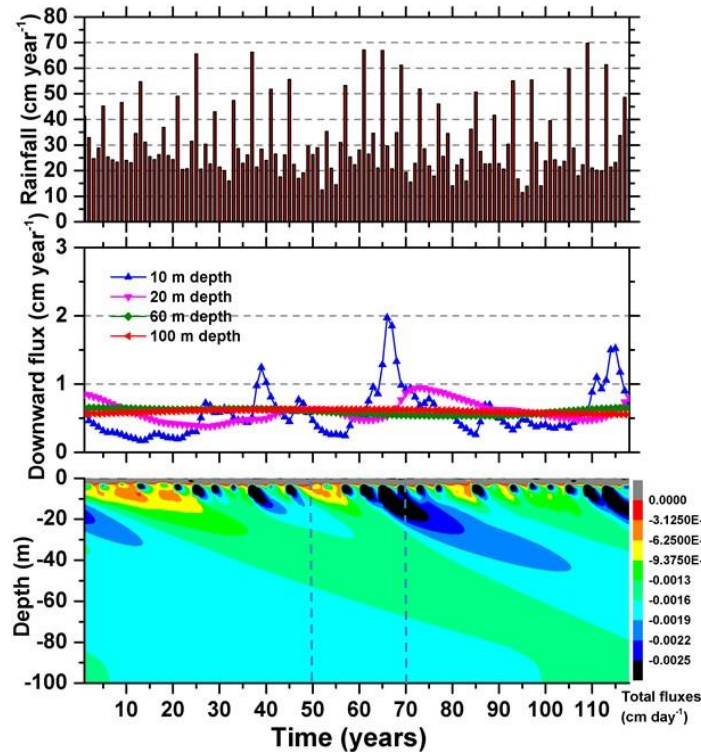


Figure 4.4: The same as Figure 4.3, but for the RIA parameterization. See Figures C.2 and C.4 for the profiles indicated by the dashed lines.

Figures 4.5-4.11 show the plots with  $r^2$  as a function of  $n$  and  $k$  and the corresponding unfiltered and filtered rainfall signals for the various depths under the wettest scenario. The noisiness of the rainfall signal resulted in relatively low correlations if  $k$  was small (e.g., Figures 4.5 and 4.7), but clear peaks could be distinguished in these cases, allowing a unambiguous identification of the lag and averaging window width at 10 and 20 m for both parameterizations. The relationship between the recharge and rainfall signal is much clearer in these cases for the filtered than for the unfiltered rainfall signal (Figures 4.7 and 4.8). The lag for RIA is larger than for FSB, with the difference increasing markedly with depth (Figures 4.6, 4.8, and 4.10). At 20 m depth, the averaging window was already 13 (FSB) or 17 years (RIA) wide. At 60 m it was multiple decades long (Figure 4.9), and the number of data points for the determination of  $r^2$  and the noisiness of the filtered rainfall record decreased accordingly. In combination with the long time lag, the large averaging windows led to short time ranges for which a filtered rainfall record could be plotted (Figure 4.10). The correlation plots (Figure 4.9) showed an increase in overall  $r^2$ -values illustrating the reduced noise in the filtered rainfall record but also showed that  $n$  and  $k$  could be determined with less accuracy. At 100 m, the lag was too large compared to the length of the rainfall record to allow a meaningful application of the method. A correlation plot could only be constructed for the FSB parameterization, but the 120-year time record was too short to permit any further analysis.

The analysis of the rainfall-recharge relationship in terms of lag times and filter window widths through correlation plots proved well suited to conditions in which it is not possible to relate groundwater recharge distinctly to the rainfall record of the past year. It also permits the analysis of the effect of droughts and relatively wet periods that extend over multiple years. For this reason we consider the

approach developed here to be a useful addition to the methods introduced by Wu et al. (1996) and Turklelltaub et al. (2015).

The combination of considerable lags and wide averaging windows poses considerable challenges for the estimation of groundwater recharge. It indicates that very long weather records may be required (several centuries) that will take generations to assemble. Climate will change during such time periods, making it very hard to calibrate any black- or grey-box models based upon such records, even if it were possible to directly observe groundwater recharge. It will be practically impossible to determine the cause (and possible remedies) of estimation errors. It can be argued that this calls for a physically-based model that reproduces the physical system and its coupled processes with as much accuracy as our state of knowledge allows. But even then the sheer impossibility of accurately characterizing a very deep vadose zone will leave even advanced modeling tools as the one we used with some components that should be considered grey-box submodels, the parameters of which can only be quantified by some form of calibration. For practical applications it stands to reason to run the model for multiple sets of judiciously chosen values of such calibration parameters to explore the range of groundwater recharge estimates within the plausible segment of the parameter space, and take into account the resulting estimate of the estimation error in the decision-making process.

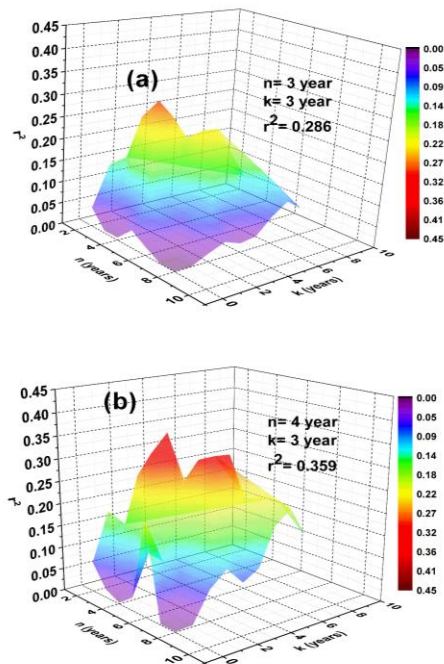


Figure 4.5: The ( $n$ ,  $k$  and  $r^2$ ) relation for FSB (a) RIA (b) for the wettest rainfall scenario at 10 m depth.

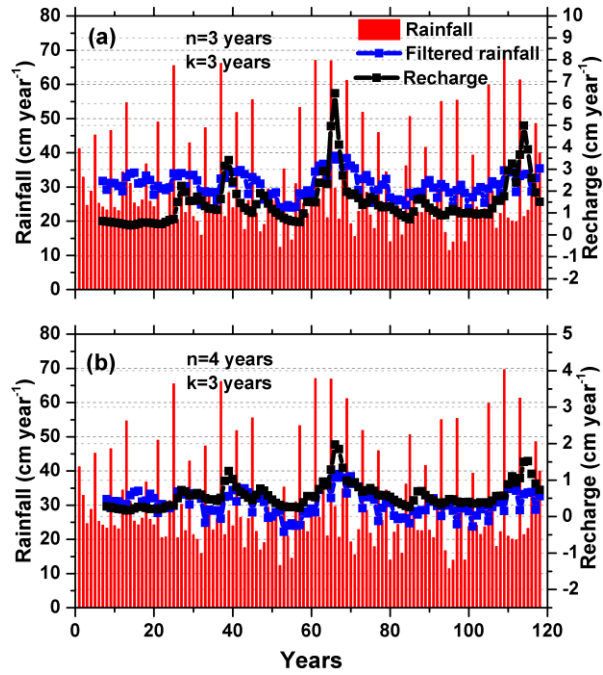


Figure 4.6: The filtered annual rainfall and the correlated annual recharge at 10 m depth for the wettest scenario with (FSB) (a) or (RIA) (b) parameterizations, where each filtered rainfall event is characterized by a lag time  $n$  and window width  $2k+1$ .

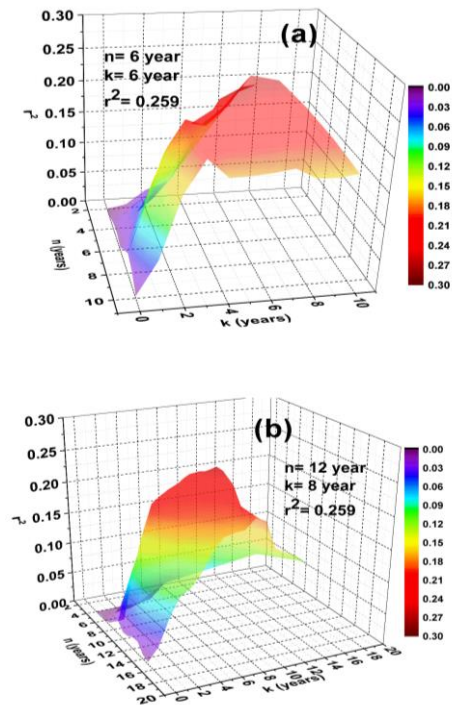


Figure 4.7: As Figure 5 at 20 m depth.

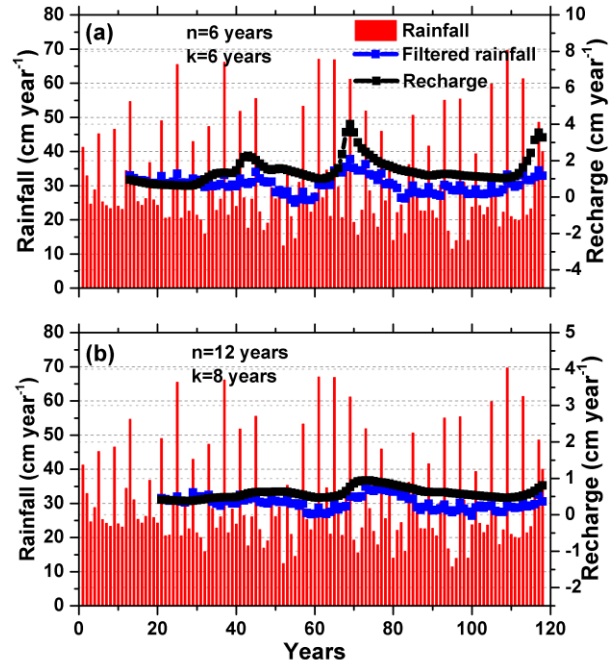


Figure 4.8: As Figure 6 at 20 m depth.

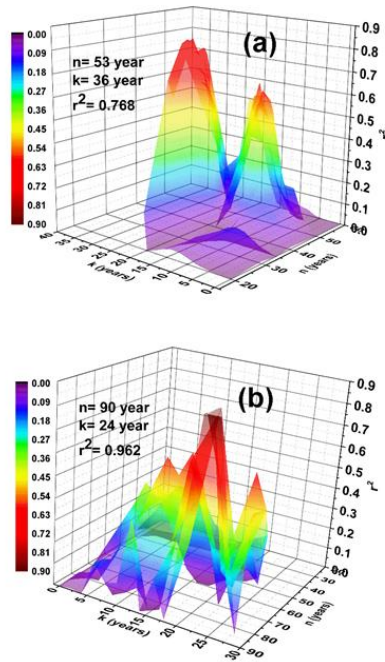


Figure 4.9: As Figure 5 at 60 m depth.



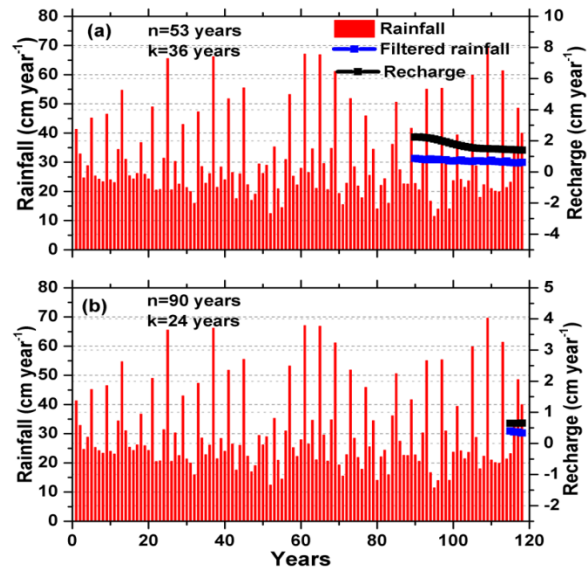


Figure 4.10: As Figure 6 at 60 m depth.

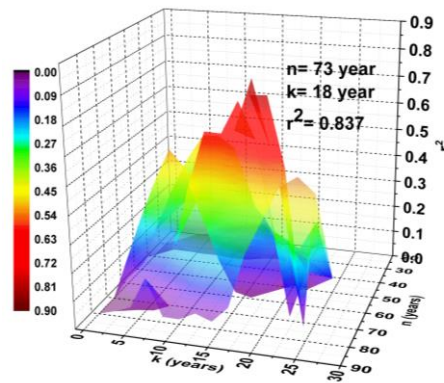


Figure 4.11: As Figure 5 only for (FSB) at 100 m depth.

#### 4.3.2.1.2. The effect of vapor flow

We repeated the simulations without including vapor flow in the numerical solution and found that its effect on groundwater recharge was only a few percent (Table 4.4), dwarfed by the effect of the soil parameterization. Even if it were known which parameterization is best, the effect of vapor flow would normally be well within the margin of error caused by other uncertainties in the forcings, hydrogeological make-up of the vadose zone, soil heterogeneity, etc.

The soil physical parameterization appears to have a strong effect of evaporation in the top few meters, because at all depths we analyzed in detail (10, 20, 60, and 100 m), the downward fluxes for FSB were about three times larger than those for RIA (Table 4.4). This of course also affects the groundwater recharge, with FSB generating 2.5 times as much groundwater recharge ( $1.47 \text{ cm yr}^{-1}$ ; 4.8% of rainfall) as

RIA (0.60 cm yr<sup>-1</sup>; 1.9% of rainfall). This is in line with Faust et al. (2006), who found nearly an order of magnitude difference in groundwater recharge estimates for an entire basin when changing the soil hydraulic parameterization.

The simulation results with vapor flow included show that the geothermal gradient did not generate a significant flux of water vapor. Figures C.1-C.4 show that the vapor flux is zero except in the very top of the unsaturated zone. In hydrological year 50 (Figures C.1 and C.2), a drought signal arrived around 40 (FSB, Figure 4.3) and 30 m (RIA, Figure 4.4) depth. In hydrological year 70 (Figures C.3 and C.4), significant downward flow occurred around 20 (FSB, Figure 4.3) and 15 m (RIA, Figure 4.4) depth. Neither of these two extremes exhibited a meaningful vapor flux below 10 m depth, and it is therefore unlikely that direct evaporation from the groundwater table is ever significant for this scenario.

Table 4.4: The total recharge (cm) at different depths of the soil profiles for scenario (1) with (FSB) and (RIA) and with and without considering vapor flow.

	Depth (m)			
	10	20	60	100
FSB wet scenario				
with vapor	172.41	171.67	174.18	173.88
without vapor	168.36	165.27	167.02	166.28
RIA wet scenario				
with vapor	67.26	70.09	70.42	70.65
without vapor	63.69	65.36	66.65	69.02

Near the soil surface, both the vapor flow and the liquid flow vary strongly between the parameterizations (insets of Figures C.1d-C.4d). In this region of the soil, the daily temperature cycles cause evaporation and condensation at different times in different depths. This complicated behavior affects the loss of soil water to the atmosphere through evaporation. For our test case with bare soil without crusting, vapor flow is of limited importance even there, as indicated by the small effect on the total fluxes (Table 4.4).

From Table 4.4 and Figures C.1d-C.4d it emerges that liquid and (to a small extent) vapor fluxes near the soil surface determine the amount of water that remains in the soil and thus is available to replenish the groundwater after decades of downward flow. Clearly, the soil hydraulic parameterization has a strong effect on evaporation and consequently on groundwater recharge. At larger depths, vapor flow is negligible. Our simulations therefore do not corroborate claims of vapor flow deep in the vadose zone affecting groundwater recharge, as reported by some of the work reviewed by de Vries and Simmers (2002).



#### **4.3.2.1.3. Vertical profiles of temperature, pressure head, water content, and liquid and vapor flux densities**

The temperature profiles reflect the effect of the geothermal gradient. Neither the daily nor the annual temperature cycle penetrates more than approximately 15 m for both parameterizations. The temperature gradient below 15 m is constant with depth and nearly constant time, but depends on the parameterization, with RIA at most approximately 0.8 °C cooler at 20 m depth than FSB. According to Table 4.3, RIA had on average 0.9 cm more evaporation per year than FSB, and the extra cooling this generated apparently is reflected throughout the temperature profile.

Comparing Figures C.1 and C.2, and Figures C.3 and C.4, it appears RIA has much lower pressure heads throughout the vadose zone than FSB, but the water content profiles are quite similar. Both sets of figures show a larger degree of damping for RIA than for FSB. This is reflected in the profiles of the liquid water flux density, which are nearly featureless for RIA below 50m depth, while episodes of high and low infiltration can be distinguished in the FSB profiles. This is consistent with the flux maps in Figures 4.3 and 4.4.

When comparing the FSB profiles of the pressure head, the water content, and the flux density for year 50 (Figure C.1) and year 70 (Figure C.3), it is possible to track the drought and infiltration signals. The elevated flux rates around 50 m depth (stemming from the rainfall in the final 15 years of the burn-in period (Figure 4.3)) in year 50 (Figure C.1d) are barely visible around 75 m depth 20 years later (Figure C.3d). The subsequent drought signal stemming from the first 25 years of rainfall (Figure 4.3) peaking at 36 m depth in year 50 is at 52 m depth in year 70. In the profiles of water pressure head and water content this propagation is much harder to detect. To illustrate this we highlighted the sharp change in the liquid water flux density near 20 m depth at year 70 (Figure C.3d, circle), caused by a large infiltration event 6 years earlier (Figure 4.3). The corresponding changes in pressure head and water content in Figures C.3b and c are much less conspicuous. Even for RIA, these features are visible (Figure C.4, circles), but at a smaller depth and less outspoken. Unfortunately, only the water content profile can realistically be expected to be observable to some extent.

#### **4.3.2.2. Drier scenario (2)**

##### **4.3.2.2.1. Signal propagation in the unsaturated zone**

Scenario 2 is much drier than scenario 1, with the rainfall in the wettest years remaining below 30 cm (Figures 4.12 and 4.13, top panels), about 40% of the amount of rainfall of the wettest years in scenario 1. Interestingly, while in the case of the wetter scenario, the damping of the rainfall signal in the unsaturated zone is stronger for RIA, under the drier scenario, FSB damps the signal more strongly, as is evident from the central and bottom panels of Figures 4.12 and 4.13. In both cases, signal damping is much more effective than for the wetter scenario, with most of the temporal variation vanished at 30 m depth. The damping is so strong that the analysis based on the correlation between annual flux rates and filtered rainfall could only be applied at 10 m depth. For FSB, the time lag was 80 years, with a window width of 21 years. RIA had a lag of 92 years and a window width of 13 years.

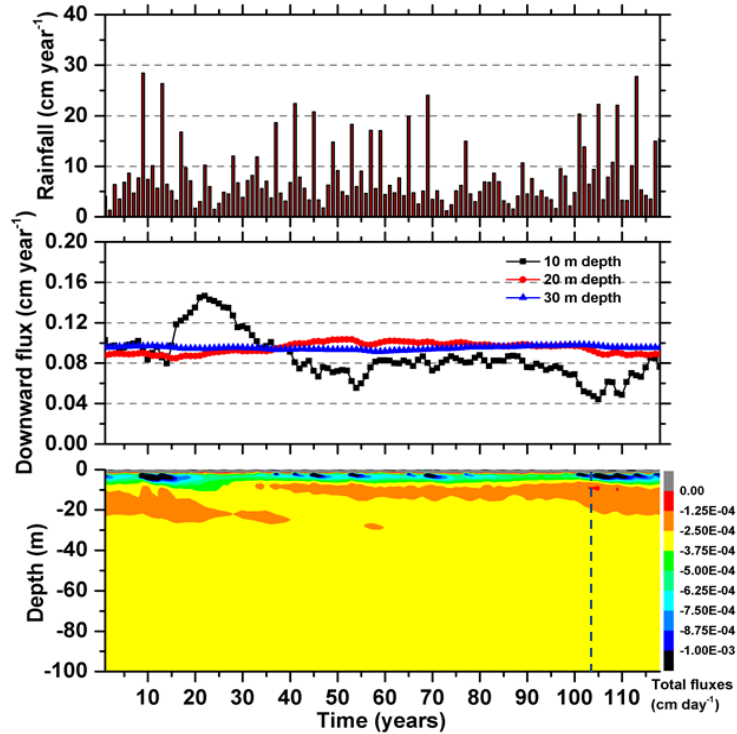


Figure 4.12: Annual rainfall amounts (top panel), the flux densities (positive downward) at selected depths (central panel) and the flux density map of the depth-time domain for the FSB parameterization (bottom panel, in which upward fluxes are positive, consistent with the vertical coordinate). The flux densities are comprised of liquid water and water vapor flux densities (the latter converted to its liquid water-equivalent) for scenario 2. The dashed vertical refers to soil profiles at 103 years (see Figure 4.18). The years plotted are hydrological years, starting at the beginning of the wet season (day 273 of non-leap years).

Despite the limited temporal variation, the total amount of net downward flow at various depths varies considerably (Table 4.5), indicating that there must be a degree of temporal variation in the flux densities in much of the soil profile. The rainfall record (top panels of Figures 4.12 and 4.13) has a wet period in the first 15 years and a drought between years 70 and 100, followed by a relative wet period with 4 years with at least 20 cm of rainfall within a 15-year time span. The central panels of Figures 4.12 and 4.13 show a spike in recharge at 10 m depth between roughly 15 and 30 years and a drop after year 100. Deeper in the profile, these signals are delayed considerably. The early spike in recharge is probably felt at every depth because it has almost a century to move travel through the profile. But the drought signal in all probability will have no effect at larger depths, as the signal at 20 m is indicating that the signal is already moving past the final year (the red line in the central panels of Figures 4.12 and 4.13). This interpretation is corroborated by total downward fluxes in Table 4.4 that are continuously increasing with depth.

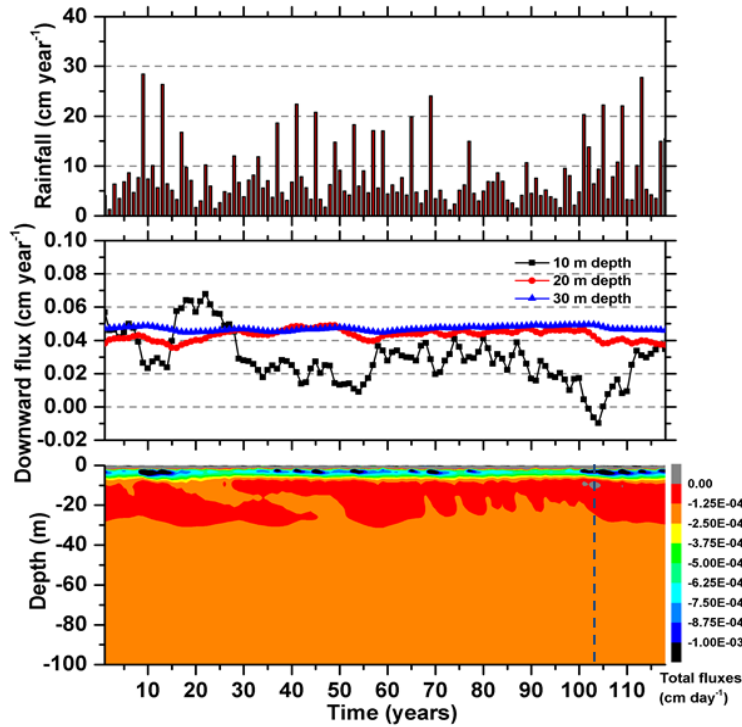


Figure 4.13: As Figure 4.12 but for the RIA parameterization. The profiles for the dashed vertical in year 103 are in Figure 4.19.

#### 4.3.2.2.2. The effect of vapor flow

Vapor flow had a distinct effect on the water flow in the top 20 m of the profile, decreasing the total downward flux by 15 to 20% for FSB, and by 20 to 42% for RIA. Below 60 m the effect was 4% or less. In one case (RIA, 60 m depth) vapor flow increased the downward flux, in all other cases it reduced it. The fact that vapor flow increases groundwater recharge is counterintuitive, but prevalent in both scenarios. At this time, an explanation cannot yet be given.

As was the case with scenario 1, the effect of the parameterization on the magnitude of the flow rates is larger than that of vapor flow, with the ratio of total flow for FSB over that for RIA decreasing from 3.0 at 10 m depth, to 1.6 at 100 m depth. The amounts of recharge are small:  $0.13 \text{ cm yr}^{-1}$  for FSB (1.6% of rainfall), and  $0.08 \text{ cm yr}^{-1}$  for RIA (1.0% of rainfall). Any substantial groundwater stock in this arid climate should therefore be considered fossil.

Table 4.5: The total recharge (cm) at different depths of the soil profiles for scenario (2) with (FSB) and (RIA) and with and without considering the vapor transport.

	Depth (m)			
	10m	20m	60m	100m
FSB dry scenario				
with vapor	10.13	11.19	12.59	15.28
without vapor	8.12	9.38	12.04	14.86
RIA dry scenario				
with vapor	3.41	5.09	7.69	9.29
without vapor	1.99	4.05	7.84	9.01

#### 4.3.2.2.3. Vertical profiles of temperature, pressure head, water content, and liquid and vapor flux densities

We analyze the profiles of various variables at midnight time of the 37898<sup>th</sup> day, at that time the flux density at 10 m depth is near its minimum. The difference in the temperature gradients (Figures 4.14a and 4.15a) below 20 m is smaller than for scenario 1, consistent with the smaller difference in average evaporation rate (0.5 cm yr<sup>-1</sup> for scenario 2).

The profiles of pressure head and water content are smooth, but indicate a deviation from unit gradient that is minor for FSB (Figure 4.14b) but considerable for RIA (Figure 4.15b). The drought signal in the downward flow rates entering the upper region of the soil profile (see the central panels of Figures 4.12 and 4.13) apparently already progresses downward in the pressure head profile, slowing downward flow throughout the profile.

The vapor fluxes are nearly zero below 20 m. The liquid water fluxes are only slightly negative in that region (Figures 4.14d and 4.15d), owing to the opposing effects of the pressure head gradient and gravity, especially for RIA. In the top 1 to 2 m of the profile, there is a high upward flux of both water and vapor for both FSB and RIA. The effect of the nightly cooling is reflected in a reversal of the trend near the soil surface: the upward fluxes of liquid water and vapor are at their maximum slightly below the soil surface. The plots reflect conditions at midnight, and the cooling soil surface results in a reduction of the fluxes. Nevertheless, the soil still appears to be losing water to the atmosphere, reflecting the aridity of the air in this very dry year.

The transmission of the annual fluctuations of the temperature and pressure head signals leads to a maximum in the matric potential and the temperature at approximately 3 m depth (Figures, 4.14a,b and 4.15a,b). This reflects the penetration of the summer-time temperatures. At some depth above this maximum, the pressure head gradient becomes too small to overcome the gradient in the gravitational potential, and the liquid water flux changes sign at this point. With temperature and pressure head gradients both decreasing, the vapor flux rate decreases as well, reaches zero, and changes sign, closely following the liquid water flux (Figures 4.14d and 4.15d).

Below the maximum, the temperature and the pressure head both decrease to reach a minimum (caused by winter temperatures), albeit at different depths (Figures 4.14a,b and 4.15a,b). Between these

two extremes, the pressure head gradient supports vertical flow, and the liquid flow reaches a minimum around 4 m depth for both FSB and RIA, indicating a peak in the downward flow (Figures 4.14d and 4.15d). Near the extreme, the pressure head gradient vanishes, then reverses sign again to oppose the gravitational pull. This leads to a very small flow rate of liquid water at approximately 6 m depth for FSB and 9 m for RIA. In the case of RIA, the flow around 9 m depth is almost entirely determined by vapor flow. The combination of the gradients in matric potential and temperature at that depth lead to upward vapor flow, and a pocket of upward total water flow develops (the grey spot in Figure 4.13, bottom panel) at a depth where the flow had been downward for a century. This illustrates the complexities of the interaction between water potentials, temperature gradients and flows when annual cycles in the boundary conditions are accounted for.

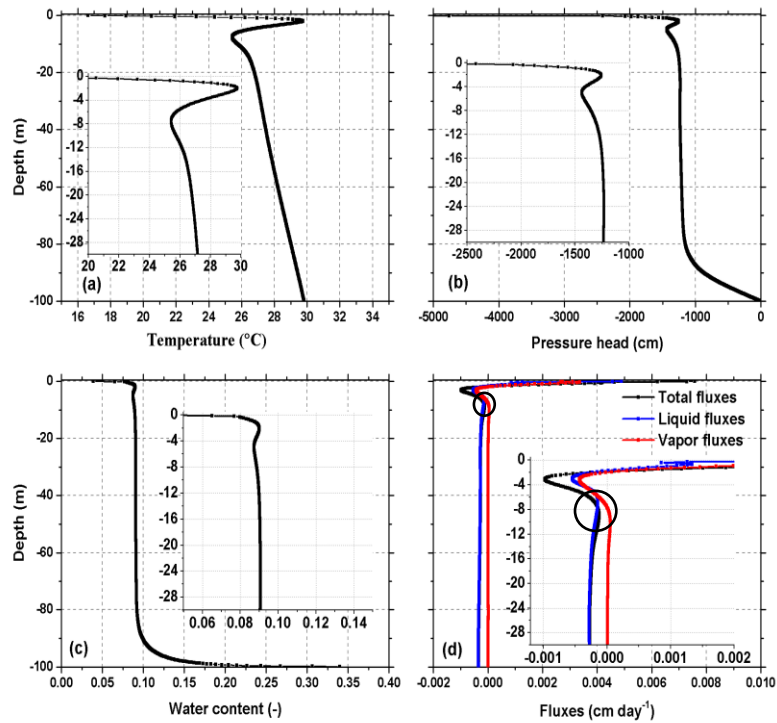


Figure 4.14: Profiles of various variables at midnight of the 37898<sup>th</sup> day in the 103<sup>th</sup> hydrological year for FSB under the drier scenario. The circle indicates the region where the liquid water flux approximates zero.

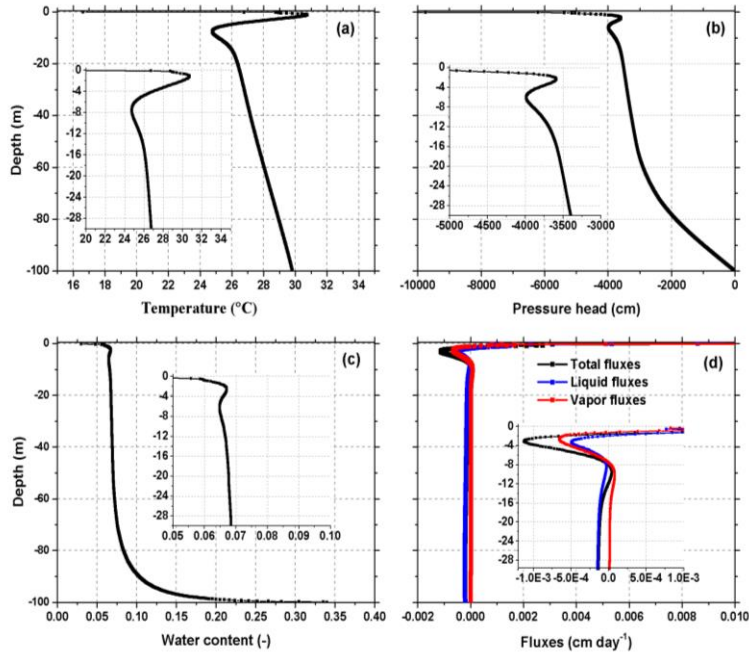


Figure 4.15: As Figure 4.14, for the RIA parameterization.

#### 4.4. Summary and Conclusions

Long-term simulations of coupled flow of liquid water, water vapor, and heat through 100 m uniform sandy loam soil profile were carried out in order to establish the rainfall-recharge relationship and to examine the effect of clusters of wet years and droughts on the dynamics of ground water recharge, the potential role of water vapor flow, and the behavior of the atmospheric input signal traveling downward in deep vadose zones in an arid and a hyper-arid climate for two soil hydraulic parameterizations.

The choice of parameterization had a very large effect on simulated groundwater recharge: under the arid scenario, FSB converted 4.8% of rainfall to recharge, whereas RIA only converted 1.9%. For the hyperarid scenario, FSB converted 1.6% to recharge, and RIA 1.0%. The total amount of rainfall under hyperarid conditions was 26% of that under arid conditions, but the amount of recharge in the hyperarid climate was only 9% (FSB) or 13% (RIA) of that under arid conditions. This suggests that a drying climate can have an amplified effect on groundwater recharge.

Neglecting vapor flow only reduced the total recharge by a few percent. Also, the geothermal gradient did not generate an autonomous vapor flux in the deep unsaturated zone. Vapor flow appeared to be significant in the upper regions of the soil, where daily and annual temperature cycles are noticeable. The complex effects of intrasoil evaporation and condensation likely led to the unexpected result that the inclusion of vapor flow in the simulations increased groundwater recharge.

The memory effect of the deep vadose zone was considerable: at several tens of meters of depth, the delay with which wet and dry period affect vertical fluxes was several decades, and the annual flux rate at any given year averaged the rainfall signal over several years up to a few decades. Particularly for RIA, the signal damping was such that the flow rates hardly varied below 20 (hyperarid) to 60 m depth (arid). The combination of rainfall record filtering and correlation analysis proved well suited for deep vadose zones as long as the signal is not too strongly damped.

## Chapter 5

### 5. Final conclusions and outlook

This thesis explored the potential of numerical modeling to quantify groundwater recharge in (semi-)arid areas by considering coupled flows of liquid water, heat, and water vapor in deep vadose zones. The ability to do so effectively was hampered by the poor performance in the dry range and a non-physical non-zero slope at saturation of the main parameterizations of the soil water retention curve. We reviewed existing parameterizations and introduced modified versions of some of them to remedy this problem. These modified parameterizations had a non-zero air-entry value and a logarithmic dry branch terminating at zero water content for a finite matric potential (no asymptote). Experimental verifications demonstrated that suitable parameterizations allowed a conventional numerical solver of Richards' equation to reproduce the development of an evaporation front in a drying soil column.

We then generated 120 years of synthetic weather data to drive long-term simulations of unsaturated flow in a very deep vadose zone. We used a model capable of solving the coupled partial differential equations of liquid water flow and heat in combination with a diffusion equation for water vapor under the assumption of instantaneous local equilibrium between the matric potential and vapor pressure. This allowed us to quantify the role of water vapor, for which conflicting observational evidence has been reported in the literature. We also studied the effect of the geothermal gradient, and specifically checked whether it was capable of generating a flow of water vapor from a deep groundwater table to the soil surface. We found that the contribution of vapor flow was only a few percent of the total water flux, and that there was no indication of a vapor flux driven by the geothermal gradient. In contrast, the choice of the soil hydraulic parameterization, which is often given little consideration, proved to have a very large effect on the calculated groundwater recharge.

The fact that vapor flow was negligible in most of the very deep unsaturated zone does not imply vapor flow is not important. Vapor flow near the soil surface determines the critical amount of rainfall that needs to be delivered in a given time period before groundwater recharge will be generated from it. Daily temperature cycles that do not penetrate deeply into the soil create a complex interplay between liquid water flow and vapor flow through evaporation and condensation processes that in turn affect the soil temperature dynamics. This may well affect root water uptake by sparse vegetation. These processes are investigated by other research groups (Saito et al., 2006, Pollacco and Mohanty, 2012). The focus of the thesis is to examine the long-term fate of the water once it leaves the most dynamic part of the unsaturated zone.

The apparent contrast between the literature reviewed in this thesis and the simulation results in Chapter 4 may reflect the difference of the role of vapor movement in the top soil (with diurnal and annual temperature cycles) and the deep subsoil (with the steady geothermal temperature gradient). Scanlon (1992) focused on the top 5 m of a roughly 150 m deep vadose zone. Her numerical simulations showed that the vapor transport was the main mode of mass transport but decreased rapidly with depth. De Vries and Simmers (2002) reported on a study on the role of vapor flow in the top 7 m of a vadose

zone of unspecified depth. Annual temperature cycles caused the vapor flow direction to change sign once a year, with the upward vapor flux in winter roughly cancelling out the downward vapor flow in summer. Both findings suggest that the overall effect on the water balance of the groundwater reservoir below a deep vadose zone could be limited, and our simulations confirm this.

We developed a new method to link events of significant infiltration deep into the vadose zone to the rainfall record. The method correlated the annual downward flux at a given depth to a moving average of the annual rainfall with varying time lag and averaging window width. We were able to show that such events are linked to elevated levels of average annual rainfall over a period of several years.

This study enables groundwater recharge estimates to be generated by recently developed solvers for the coupled water flow, heat flow, and vapor diffusion equations by providing the necessary infrastructure: soil hydraulic parameterizations capable of handling the full range of soil water contents, a simple temperature model in combination with a state-of-the-art numerical rainfall generator, and a methodological analysis of the correlation between the rainfall record and soil water flux rates at various depths in the soil profile.

Currently, this approach can only be carried out for 1-dimensional soil columns. We still need a methodology to aggregate a set of one-dimensional studies to estimate the groundwater recharge of extensive aquifers, which often support indigenous populations. Other research groups are researching coupled flow of water, heat and vapor in cropped soils. This work needs to be extended to sparse (and possibly grazed) vegetation, which then can be coupled to the deep-soil simulations carried out here to create more realistic simulation scenarios, in order to improve the accuracy of the groundwater recharge estimates.

A prominent problem is the lack of weather data and information on the soil hydraulic properties of the unsaturated zone. Our work shows that many decades, if not centuries, of weather data will be required. It is therefore unavoidable to work with synthetic weather data. Nevertheless, there is a pressing need to attempt to establish weather stations in politically stable semi-arid areas in order to ensure that future generations can at least have data records that allows them to estimate the parameters of the weather generators. This will also allow scientists and authorities to monitor the effect of climate change, which will impact the temporal trends of the weather parameters.

Soil hydraulic properties at large depths cannot realistically be obtained. This limitation notwithstanding, it is worthwhile to develop experimental tests of the various suitable soil hydraulic parameterizations presented in this thesis for a wide variety of soils in order to determine if there is a superior one among them. At this stage we can only point to the very different results produced by different parameterizations without being able to state which is closest to the truth. For scenario studies on which to base decisions regarding land use and water withdrawal from aquifers this is undesirable.



## Bibliography

- Alexander, L. and Skaggs, R. W.: Predicting unsaturated hydraulic conductivity from the soil water characteristic, *Trans. Am. Soc. Agric. Eng.*, 29, 176-184, 1986.
- Barnes, C. J. and Turner, J. V.: Isotopic exchange in soil water. In: Kendall, C. and McDonnell, J. J. (eds.) *Isotope tracers in catchment hydrology*, pp.137-163. Elsevier, Amsterdam, 839 p, 1998.
- Barr, J., Grego, S., Hassan, E., Niasse, M., Rast, W., and Talafre, J.: Regional challenges, global impacts. In: WWAP (World Water Assessment Programme). 2012. *The United Nations World Water Development Report 4: Managing water under uncertainty and risk*. Paris, UNESCO, 2012.
- Behrangi, A., Khakbaz, B., Vrugt, J. A., Duan, Q., and Sorooshian, S.: Comment on "Dynamically dimensioned search algorithm for computationally efficient watershed model calibration" by Tolson, B.A., and Shoemaker, C. A., *Water Resour. Res.*, 44, doi: 10.1029/2007WR006429, 2008.
- Brooks, R. H. and Corey, A. T.: Hydraulic properties of porous media, Colorado State Univ., Hydrology Paper No. 3, 27 pp, 1964.
- Bradley, R. S.: Polymolecular adsorbed films. Part I. The adsorption of argon on salt crystals at low temperatures, and the determination of surface fields, *J. Chem. Soc. (Resumed)*, 1467-1474, doi: 10.1039/JR9360001467, 1936.
- Burdine, N. T.: Relative permeability calculations from pore size distribution data, *Trans. Am. Inst. Min. Metall. Pet. Eng.*, 198, 71-81, 1953.
- Campbell, G. S.: A simple method for determining unsaturated hydraulic conductivity from moisture retention data, *Soil Sci.*, 117, 311-314, 1974.
- Campbell, G. S., and Shiozawa, S.: Prediction of hydraulic properties of soils using particle-size distribution and bulk density data. p. 317-328. In: van Genuchten, M. Th., Leij, F. J., and Lund, L. J. (eds.), *indirect methods for estimating the hydraulic properties of unsaturated soils*. Univ. of California, Riverside, 1992.
- Cass, A., Campbell, G. S., and Jones, T.L.: Enhancement of thermal water vapor diffusion in soil. *Soil Sci. Soc. Am. J.*, 48, 25-32, 1984.
- Chenini, I., and Ben Mammou, A.: Groundwater recharge study in arid region: An approach using GIS techniques and numerical modeling, *Computers & Geosciences*, 36, 801-817, doi: 140.1016/j.cageo.2009.06.014, 2010.
- Chung, S.-O., and Horton, R.: Soil heat and water flow with a partial surface mulch, *Water Resour. Res.*, 23(12), 2175-2186, 1987.

- Coppola, A.: Unimodal and bimodal descriptions of hydraulic properties for aggregated soils, *Soil Sci. Soc. Am. J.*, 64, 1252-1262, 2000.
- Coppola, A., Basile, A., Comegna, A., and Lamaddalena, N.: Monte Carlo analysis of field water flow comparing uni- and bimodal effective hydraulic parameters for structured soil. *J. Contam. Hydrol.* 104:153-165, doi: 10.1016/j.jconhyd.2008.09.007, 2009.
- Cornelis, W. M., Khlosi, M., Hartmann, R., Van Meirvenne, M., and De Vos, B.: Comparison of unimodal analytical expressions for the soil-water retention curve, *Soil Sci. Soc. Am. J.*, 69, 1902-1911, doi: 10.2136/sssaj2004.0238, 2005.
- Cosgrove, C., Cosgrove, W. J., Hassan, E., and Talafre, J.: Understanding uncertainty and risks associated with key drivers. In: WWAP (World Water Assessment Programme). 2012. The United Nations World Water Development Report 4: Managing water under uncertainty and risk. Paris, UNESCO, 2012.
- de Vries, J. J. and Simmers, I.: Groundwater recharge: an overview of processes and challenges, *Hydrogeology Journal*, 10, 5-17, doi: 10.1007/s10040-001-0171-7, 2002.
- Dirksen, C.: *Soil Physics Measurements*, Catena Verlag GmbH, Reiskirchen, Germany, 1999.
- Dregne, H. E.: Global status of desertification, *Annals of Arid Zone*, 30, 179–185, 1991.
- Döll, P., and Flörke, M.: Global-scale estimation of diffuse groundwater recharge. Model tuning to local data for semi-arid and arid regions and assessment of climate impact, Frankfurt Hydrology Paper 03, Institute of Physical Geography, Frankfurt University, Frankfurt am Main, Germany, 2005.
- Duan, Q., Sorooshian, S. and Gupta, V.: Effective and efficient global optimization for conceptual rainfall-runoff models, *Water Resour. Res.*, 28, 1015-1031, 1992.
- Durbin, T.: Interactive comment on ‘Water-balance and groundwater-flow estimation for an arid environment: San Diego region, California’, by L. E. Flint et al. *Hydr. Earth Syst. Sci. Discuss.*, 9, C1144-C1166, [www.hydrol-earth-syst.sci-discuss.net/9/C1144/2012/](http://www.hydrol-earth-syst.sci-discuss.net/9/C1144/2012/), 2012.
- Durner, W.: Hydraulic conductivity estimation for soils with heterogeneous pore structure, *Water Resour. Res.* 30, 211-223, 1994.
- Durner, W. and Flühler, H.: Soil hydraulic properties. *Encyclopedia of Hydrological Sciences*, John Wiley & Sons, Ltd, doi: 10.1002/0470848944.hsa077c, 2005.
- Faust, A.E., Ferré, T.P.A., Schaap, M.G., and Hinnell, A.C.: Can basin-scale recharge be estimated reasonably with water-balance models? *Vadose Zone J.*, 5, 850-855, doi:10.2136/vzj2005.0109, 2006.
- Fayer, M. J. and Simmons, C. S.: Modified soil water retention functions for all matric suctions, *Water Resour. Res.*, 31, 1233-1238, 1995.

- Food and Agriculture Organization of the United Nations (FAO): Coping with Water Scarcity. Challenge of the Twenty First Century. World Water Day, 22<sup>nd</sup> March 2007, <http://www.fao.org/nr/water/docs/escarcity.pdf>, 2007.
- Food and Agriculture Organization (FAO): Aquaculture in desert and arid lands. Development constraints and opportunities. Hermosillo, Mexico, 202 pp, 2010.
- Food and Agriculture Organization (FAO): AQUASTAT Main Database, <http://www.fao.org/nr/water/aquastat/data/query/index.html>, 2016 Website accessed on June 15, 2017.
- Flint, L.E., Flint, A.L., Stolp, B.J., and Danskin, W.R.: A basin-scale approach for assessing water resources in a semiarid environment: San Diego region, California and Mexico, *Hydr. Earth Syst. Sci.*, 16, 3817–3833, [www.hydrol-earth-syst-sci.net/16/3817/2012/](http://www.hydrol-earth-syst-sci.net/16/3817/2012/)doi:10.5194/hess-16-3817-2012, 2012.
- Fuentes, C., Haverkamp, R., Parlange, J. –Y., Brutsaert, W., Zayani, K. and Vachaud, G.: Constrains on parameters in three soil water capillary retention equations, *Transport in Porous Media*, 6, 445-449, 1991.
- Gee, G. W., and Hillel, D.: Groundwater recharge in arid regions: review and critique of estimation methods, *Hydrological Processes*, 2, 255-266, 1988.
- Gleick, P.: Water and conflict freshwater resources and international security. *International Security*, 18, 79-112, 1993.
- Goss, K. -U., and Madliger, M.: Estimation of water transport based on in situ measurements of relative humidity and temperature in a dry Tanzanian soil, *Water Resour. Res.*, 43, W05433, doi: 10.1029/2006WR005197, 2007.
- Gowing, J. W., Konukcuve, F., and Rose, D. A.: Evaporative flux from a shallow watertable: the influence of a vapour-liquid phase transition, *J. Hydrol.*, 321, 77-89, doi:10.1016/j.jhydrol.2005.07.035, 2006.
- Green, R., Bertetti, F. B., and Hernandez, M.: Recharge variability in semi-arid climates, *Nature Education Knowledge* 3(10), 34, 2012.
- Groenevelt, P. H. and Grant, C. D.: A new model for the soil-water retention curve that solves the problem of residual water contents, *European J. of Soil Science*, 55, 479-485, doi: 10.1111/j.1365- 2389.2004.00617.x, 2004.
- Hollenbeck, K. J., and Jensen, K. H.: Maximum-likelihood estimation of unsaturated hydraulic parameters. *J. Hydrol.*, 210, 192-205, 1998.
- Hollenbeck, K. J., Šimunek, J. and van Genuchten, M. Th. RETMCL: Incorporating maximum-likelihood estimation principles in the RETC soil hydraulic parameter estimation code, *Computers and Geosciences*, 26, 319-327, 2000.

- Hutson, J. L. and Cass, A.: A retentively functions for use in soil-water simulation models, *J. of Soil Sci.*, 38, 105-113, 1987.
- Hoffmann-Riem, H., van Genuchten, M. Th., and Flühler, H.: General model for the hydraulic conductivity of unsaturated soils. In: van Genuchten, M. Th., Leij, F.J. and Wu, L. (eds.), *Proceedings of the international workshop on characterization and measurement of the hydraulic properties of unsaturated porous media*, Riverside, California, October 22-24, 1997. Part1. U.S. Salinity Laboratory, ARS, U.S. Dept. of Agriculture and Dept. of Environ. Sci., Univ. California, Riverside, California, pp. 31-42, 1999.
- Iden, S. C., and Durner, W.: Free-form estimation of soil hydraulic properties using Wind's method. *European J. of Soil Sci.*, 59, 1365-2389, doi: 10.1111/j.1365-2389.2008.01068.x, 2008.
- Iden, S. C., and Durner, W.: Comment on 'Simple consistent models for water retention and hydraulic conductivity in the complete moisture range' by Peters, A. *Water Resour. Res.*, 50, 7530-7534, doi: 10.1002/2014WR015937, 2014.
- Iden, S. C., Peters, A., and Durner, W.: Improving prediction of hydraulic conductivity by constraining capillary bundle models to a maximum pore size, *Adv. Water Resources*, 85, 86-92, doi:10.1016/j.advwatres.2015.09.005, 2015.
- Ippisch, O., Vogel, H. -J., and Bastian, P.: Validity limits for the van Genuchten-Mualem model and implications for parameter estimation and numerical simulation, *Adv. Water Resources*, 29, 1780-1789, doi:10.1016/j.advwatres.2005.12.011, 2006.
- Jackson. R. D.: Water vapor diffusion in relatively dry soil: I. Theoretical considerations and sorption experiments, *Soil Sci. Soc. Am. Proc.*, 28, 172-176, 1964.
- Jarvis, N. J., Zavattaro, L., Rajkai, K., Reynolds, W. D., Olsen, P. -A., McGechan, M., Mecke, M., Mohanty, B., Leeds-Harrison, P. B., and Jacques, D.: Indirect estimation of near-saturated hydraulic conductivity from readily available soil information, *Geoderma*, 108, 1-17, 2002.
- Kamphorst, A., and Bolt, G. H.: Saline and Sodic Soils, in *Soil Chemistry: A. Basic Elements*, edited by G. H. Bolt and M. G. M. Bruggenwert, pp. 171 - 191, Elsevier, Amsterdam, Netherlands, 1978.
- Khlosi, M., Cornelis, W. M., Douaik, A., van Genuchten, M. Th. and Gabriels, D.: Performance evaluation of models that describe the soil water retention curve between saturation and oven dryness, *Vadose Zone J.*, 7, 87-96. doi:10.2136/vzj2007.0099, 2008.
- Khlosi, M., Cornelis, W. M., Gabriels, D. and Sin, G.: Simple modification to describe the soil water retention curve between saturation and oven dryness, *Water Resour. Res.*, 42, W11501, doi: 10.1029/2005WR004699, 2006.
- Kim, D., Olivera, F., Cho, H., Socolofsky, S.A.: Regionalization of the modified Bartlett-Lewis rectangular pulse stochastic rainfall model, *Terr. Atmos. Ocean. Sci.*, 24, 421-436, doi:10.3319/TAO.2012.11.12.01(Hy), 2013.

- Kirkpatrick, S., Gelatt, C. D. and Vecchi, M. P.: Optimization by simulated annealing, *Science*, 220, 671-680, doi: 10.1126/science.220.4598.671,1983.
- Klute, A.: Water retention: Laboratory methods. In: Klute, A. (ed.) *Methods of soil analysis. Part 1. Physical and mineralogical methods. Second edition.* P. 635-662. American Society of Agronomy, Inc, Soil Science Society of America, Inc. Madison, Wisconsin, U.S.A. 1188 pp, 1986.
- Konukcu F., Istanbuluoglu, A., and Kocaman, I.: Determination of water content in drying soils: incorporating transition from liquid phase to vapour phase, *Aust. J. Soil Res.*, 42(1), 1–8, 2004.
- Kosugi, K.: Lognormal distribution model for unsaturated soil hydraulic properties. *Water Resour. Res.*, 32, 2697-2703, 1996.
- Kosugi, K.: General model for unsaturated hydraulic conductivity for soils with lognormal pore-size distribution, *Soil Sci. Soc. Am. J.*, 63, 270-277, 1999.
- Kosugi, K, Hopmans, J. W., and Dane, J. H.: Water retention and Storage. Parametric models. In: Dane, J. H. and G. C. Topp (eds.) *Methods of soil analysis. Part 4. Physical methods.* P. 739-757. American Society of Agronomy, Inc, Soil Science Society of America, Inc. Madison, Wisconsin, U.S.A. 1692 pp, 2002.
- Lebeau, M. and Konrad, J. -M.: A new capillary and thin film flow model for predicting the hydraulic conductivity of unsaturated porous media, *Water Resour. Res.*, 46, W12554, doi:10.1029/2010WR009092, 2010.
- Leij, F. J., and van Genuchten, M. Th.: Solute transport, in *Soil Physics Companion*, edited by Warrick, A. W. pp. 189-248, CRC Press, Boca Raton, Florida, 2002.
- Leij, F. J., Russell, W. B., and Lesch, S. M.: Closed-form expressions for water retention and conductivity data, *Ground Water*, 35, 848-858, 1997.
- Liu, H. H., and Dane, J. H.: Improved computational procedure for retention relations of immiscible fluids using pressure cells, *Soil Sci. Soc. Am. J.*, 59, 1520-1524, 1995.
- Milly, P. C. D.: A simulation analysis of thermal effects on evaporation, *Water Resour. Res.*, 20, 1087–1098, 1984.
- Morel-Seytoux, H. J., and Nimmo, J. R.: Soil water retention and maximum capillary drive from saturation to oven dryness, *Water Resour. Res.*, 35, 2031–2041, 1999.
- Mualem, Y.: A new model for predicting the hydraulic conductivity of unsaturated porous media, *Water Resour. Res.*, 12, 513-521, 1976.
- Mualem, Y.: Modeling the hydraulic conductivity of unsaturated porous media, p. 15–36. In: van Genuchten, M. Th., Leij, F. J., and Lund, L. J. (eds.), *Indirect methods for estimating the hydraulic properties of unsaturated soils.* Univ. of California, Riverside, 1992.

- Mualem, Y., and Dagan, G.: Hydraulic conductivity of soils: unified approach to statistical models, *Soil Sci. Soc. Am. J.*, 42, 392-395, 1978.
- National centers for environmental information: <http://www.ncdc.noaa.gov/cdo-web/>, last Access: 1 March 2016.
- Ng, G-H.C., McLaughlin, D., Entekhabi, D., and Scanlon, B.R.: Probabilistic analysis of the effects of climate change on groundwater recharge, *Water Resour. Res.* 46:W07502, doi: 10.1029/2009WR007904, 2010.
- Olver, F. W. J., Lozier, D. W., Boisvert, R. F., and Clark, C. W. (Editors): *NIST Handbook of mathematical functions*. National Institute of Standards and Technology (U.S. Dept. of Commerce), and Cambridge University Press, Cambridge, UK, 2010.
- Or, D., Lehmann, P., Shahraeeni, E., and Shokri, N.: Advances in soil evaporation physics – a review, *Vadose Zone J.*, 12, doi:10.2136/vzj2012.0163, 2013.
- Or, D., and Wraith, M.: Soil water content and water potential relationship, in *Handbook of Soil Science*, edited by Summer, M. E., pp. 53–85, CRC Press, Boca Raton, Florida, 2000.
- Osterkamp, W.R., and Lane, L.J.: Ground-water recharge estimates in arid areas using channel morphology and a simulation model. In: Alsharhan, A.S. and Wood, W.W., (eds.) *Water resources perspectives: Evaluation, management and policy*. Elsevier, the Netherlands, 2003.
- Pollacco, J. A., and Mohanty, B. P.: Uncertainties of Water Fluxes in Soil-Vegetation-Atmosphere Transfer Models: Inverting Surface Soil Moisture and Evapotranspiration Retrieved from Remote Sensing, *Vadose Zone J.*, 11(3), doi:10.2136/vzj2011.0167, 2012.
- Peters, A.: Simple consistent models for water retention and hydraulic conductivity in the complete moisture range, *Water Resour. Res.*, 49, 6765-6780, doi:10.1002/wrcr.20548, 2013.
- Peters, A.: Reply to comment by Iden, D. and Durner, W. on ‘Simple consistent models for water retention and hydraulic conductivity in the complete moisture range.’ *Water Resour. Res.*, 50, 7535-7539, doi: 10.1002/2014WR016107, 2014.
- Peters, A., and Durner, W.: Simplified evaporation method for determining soil hydraulic properties, *J. Hydrol.*, 356, 147–162, 2008.
- Pham, M.T., Vanhaute, W.J., Vanderberghe, S., De Baets, B., and Verhoest, N.E.C.: An assessment of the ability of Bartlett-Lewis type of rainfall models to reproduce drought statistics, *Hydrol. Earth Syst. Sci.* 17, 5167-5183. [www.hydrol-earth-syst-sci.net/17/5167/2013/](http://www.hydrol-earth-syst-sci.net/17/5167/2013/), doi: 10.5194/hess-17-5167-2013, 2013
- Philip J. R., and de Vries, V. D.: Moisture movement in porous materials under temperature gradient, *Trans Am. Geophys. Union*, 38(2), 222–232, 1957.
- Postel, S., and Wolf, A.: Dehydrating conflict. *Foreign Policy*, 1 September, 2001.

- Press, W. H., Teukolsky, S. A., Vetterling, W. T., and Flannery, B. P.: Numerical recipes in Fortran. The art of scientific computing, 2<sup>nd</sup> ed., Cambridge University Press, Cambridge, UK, 1992.
- Raats, P. A. C.: A superclass of soils. p. 45–51. In: van Genuchten, M. Th., Leij, F. J., and Lund, L. J. (eds.), Indirect methods for estimating the hydraulic properties of unsaturated soils. Univ. of California, Riverside, 1992.
- Ritchie, J. T.: Dryland evaporative flux in a sub humid climate: I. Micrometeorological influences, *Agronomy Journal*, 63, 51-55, 1971.
- Rodriguez-Iturbe, I., Cox, D. R., Isham, V.: A point process model for rainfall: further developments, *Proc. R. Soc. Lond. A* 417, 283-298. Xi, B., Tan, K.M., Liu, C., 2013. Logarithmic transformation-based gamma random number generators, *J. Statistical Software*, 55(4), 1-17, 1988.
- Rosenbaum, U., Bogaen, H. R., Herbst, M., Huisman, J. A., Peterson, T. J., Weuthen, A., Western, A. W., and Vereecken, H.: Seasonal and event dynamics of spatial soil moisture patterns at the small catchment scale. *Water Resour. Res.*, 48, W10544, doi: 10.1029/2011WR011518, 2012, 2012.
- Rose, D. A.: Water movement in porous materials: Part 1. Isothermal vapour transfer, *Br. J. Appl. Phys.*, 14(5), 256–262, 1963a.
- Rose, D. A.: Water movement in porous materials: Part 2. The separation of the components of water movement, *Br. J. Appl. Phys.*, 14(8), 491–496, 1963b.
- Rose, D. A.: Water movement in dry soils: 1. Physical factors affecting sorption of water by dry soil, *J. of Soil Sci.*, 19(1), 81–93, 1968a.
- Rose, D. A.: Water movement in porous materials III. Evaporation of water from soil, *Br. J. Appl. Phys.*, (J. Phys. D), Series 2(1), 1779–1791, 1968b.
- Rossi, C., and Nimmo, J. R.: Modeling of soil water retention from saturation to oven dryness, *Water Resour. Res.*, 30, 701-708, 1994.
- Saito, H., Šimůnek, J., and Mohanty, B. P.: Numerical analysis of coupled water, vapor, and heat transport in the vadose zone, *Vadose Zone J.*, 5(2), 784–800, doi:10.2136/vzj2006.0007, 2006.
- Sakai, M., Toride, N., and Šimůnek, J.: Water and vapor movement with condensation and evaporation in a sandy column, *Soil Sci. Soc. Am. J.*, 73(3), 707–717, 2009.
- Scanlon, B. R.: Evaluation of liquid and vapor flow in desert soils based on chlorine-36 and tritium tracers and non-isothermal flow simulations, *Water Resour. Res.*, 28, 285-29, 1992.
- Scanlon B. R., Keese, K. E., Reedy, R. C., Šimůnek, J., and Andraski, B. J.: Variations in flow and transport in thick desert vadose zones in response to paleoclimatic forcing (0–90 kyr): field measurements, modeling, and uncertainties, *Water Resour. Res.*, 39, 1179, doi: 1110D1029/2002WR001604, 2003.

- Scanlon, B. R., Keese, K. E., Flint, A. L., Flint, L. E., Gaye, C. B., Edmunds, W. M. and Simmers, I.: Global synthesis of groundwater recharges in semiarid and arid regions, *Hydrological Processes*, 20, 3335-3370, doi: 10.1002/hyp.6335, 2006.
- Scanlon, B. R., Mukherjee, A., Gates, J. B., Reedy, R. C., and Sinha, A. K.: Groundwater recharge in natural dune systems and agricultural ecosystems in the Thar Desert region, Rajasthan, India, *Hydrogeology Journal*, 18, 959-972, doi: 10.1007/s10040-009-0555-7, 2010.
- Schaap, M. G., and Leij, F. J.: Improved prediction of unsaturated hydraulic conductivity with the Mualem-van Genuchten model, *Soil Sci. Soc. Am. J.*, 64, 843-851, 2000.
- Schaap, M. G., and van Genuchten, M. Th.: A modified Mualem-van Genuchten formulation for improved description of the hydraulic conductivity near saturation, *Vadose Zone J.*, 5, 27-34, doi:10.2136/vzj2005.0005, 2006.
- Schelle, H., Heise, L., Jänicke, K., and Durner, W.: Water retention characteristics of soils over the whole moisture range: a comparison of laboratory methods, *European J. of Soil Sci.*, 64, 814 – 821, 2013.
- Schneider, M., and Goss, K. U.: Prediction of water retention curves for dry soils from an established pedotransfer function: Evaluation of the Webb model, *Water Resour. Res.*, 48, W06603, doi: 10.1029/2011WR011049, 2012.
- Schindler, U., von Unold, G., Durner, W., and Müller, L.: Evaporation method for measuring unsaturated hydraulic properties of soils: extending the range, *Soil Sci. Soc. Am. J.*, 74, 1071–1083, doi: 10.2136/sssaj2008.0358, 2010.
- Schindler, U., von Unold, G., Durner, W., and Mueller, L.: Recent progress in measuring soil hydraulic properties, In: *Proceedings of the International Conference on Environment and Civil Engineering*, April 24-25, 2015, Pattaya, Thailand, p. 47-52, doi:10.15242/IAE.IAE0415401, 2015.
- Schulz, S., de Rooij, G. H., Michelsen, N., Rausch, R., Siebert, C., Schüth, C., Al-Saud, M., and Merz, R.: Estimating groundwater recharge for an arid karst system using a combined approach of time-lapse camera monitoring and water balance modelling, *Hydrological Processes*, 30(5), 771-782, doi:10.1002/hyp.10647, 2016.
- Shokri, N., and Or, D.: What determines drying rates at the onset of diffusion controlled stage-2 evaporation from porous media?, *Water Resour. Res.*, 47, W09513, doi: 10.1029/2010WR010284, 2011.
- Šimůnek, J., Šejna, M., Saito, H., Sakai, M., and van Genuchten, M. Th.: The HYDRUS-1D software package for simulating the one-dimensional movement of water, heat, and multiple solutes in variably-saturated media, Version 4.17, *HYDRUS Software Series 3*, Department of Environmental Sciences, University of California Riverside, Riverside, California, USA, pp. 342, 2013.



- Šimůnek, J., van Genuchten, M. Th., Šejna, M.: Recent developments and applications of the HYDRUS computer software packages, *Vadose Zone J.*, 15(7), 1- 25, doi: 10.2136/vzj2016.04.0033, 2016.
- Smakhtin, V., Revenga, C., and Döll. P.: Taking into account environmental water requirements in global-scale water resources assessments. Comprehensive assessment research report 2, Comprehensive Assessment Secretariat, Colombo, Sri Lanka, 2004.
- Toews, M. W., and Allen, D. M.: Simulated response of groundwater to predicted recharge in a semi-arid region using a scenario of modelled climate change, *Environ. Res. Let.* 4, 035003 (19 pp), doi: 10.1088/1748-9326/4/3/035003, 2009.
- Tolson, B. A. and Shoemaker, C. A.: Dynamically dimensioned search algorithm for computationally efficient watershed model calibration, *Water Resour. Res.*, 43, W01413, doi: 10.1029/2005WR004723, 2007.
- Tuller, M. and Or, D.: Hydraulic conductivity of variably saturated porous media: Film and corner flow in angular pore space, *Water Resour. Res.*, 37, 1257-1276, doi: 10.1029/2000WR900328, 2001.
- Turkeltaub, T., Kurtzman, D., Bel, G., Dahan, O.: Examination of groundwater recharge with a calibrated/validated flow model of the deep vadose zone, *J. Hydrol.* 522, 618-627, 2015.
- Tyler, S. W. and Wheatcraft, S. W.: Fractal processes in soil water retention, *Water Resour. Res.*, 26, 1047-1054, 1990.
- UMS: HYPROP-Fit User Manual. UMS GmbH, Munich, Germany, [http://www.ums.muc.de/static/Manual\\_HYPROP-FIT.pdf](http://www.ums.muc.de/static/Manual_HYPROP-FIT.pdf), 2015, last access August 31, 2016
- United Nations Development Programme (UNDP): Human Development Report 2006. Beyond Scarcity: Power, Poverty and the Global Water Crisis, New York, 422 pp, 2006.
- United Nations: Coping with water scarcity. A strategic issue and priority for system-wide action, 2016.
- van Genuchten, M. Th.: A closed-form equation for predicting the hydraulic conductivity for unsaturated soils, *Soil Sci. Soc. Am. J.*, 44, 892-898, 1980.
- Vogel, T., van Genuchten, M. Th. and Cislérova, M.: Effect of the shape of the soil hydraulic functions near saturation on variably-saturated flow predictions, *Adv. Water Resources*, 24, 133-144, 2001.
- Walvoord, M. A., and Scanlon, B. R.: Hydrologic Processes in Deep Vadose Zones in Interdrainage Arid Environments, in *Groundwater Recharge in a Desert Environment: The Southwestern United States*, edited by Hogan, J. F., Phillips, F. M. and Scanlon, B. R., pp. 15-28, American Geophysical Union Water Science and Applications Series, 9, 15-28, Wiley, University of Michigan, New York, 2004.
- Wang, H., Kgotlhang, L., and Kinzelbach, W.: Using remote sensing data to model groundwater recharge potential in Kanye region, Botswana, *The International Archives of the Photogrammetry, Remote Sensing and Spatial Information Sciences*, vol. XXXVII, Part B8, 751-756, 2008.

- Webb, S. W.: A simple extension of two-phase characteristic curves to include the dry region, *Water Resour. Res.*, 36, 1425–1430, 2000.
- Western, A. W., Grayson, R. B., and Blöschl, G.: Scaling of soil moisture. A hydrologic perspective, *Annu. Rev. Earth Planet. Sci.*, 30, 149–80, doi: 10.1146/annurev.earth.30.091201.140434, 2002.
- Wu, J., Zhang, R., Yang, J.: Analysis of rainfall-recharge relationships, *J. Hydrol.*, 177, 143-160, 1996.
- WWAP (World Water Assessment Programme): The United Nations World Water Development Report 4: Managing water under uncertainty and risk. Paris, UNESCO, 2012.
- Zeng, Y., Wan, L., Su, Z., Saito, H., Huang, K., and Wang, X.: Diurnal soil water dynamics in the shallow vadose zone (field site of China University of Geosciences, China), *Environ. Geol.*, 58(1), 11–23, 2009.

## Appendix A. The variables used in Chapter 2

Table A.1: List of variables of Chapter 2.

Variables	Dimensions	Properties, and equation to which the variable pertains (where applicable)
$A_1$	$L^{-2}$	Constant, Eq. (2.7)
$A_2$	-	Constant of, Eq. (2.12a)
$B(h)$	$L^n$	Function simplifying notation, Eq. (2.11c)
$b$	-	Shape parameter, Eq. (2.25)
$C$	-	Constant simplifying notation, Eq. (2.11c)
$c_1$	-	Constant, Eq. (2.14a)
$c_2$	-	Constant, Eq. (2.15a)
$\mathbf{d}_\theta$	Varies	Vector of length $q_\theta$ of squared differences between observations and fits, Eq. (2.27)
$E(h)$	$L^{-k}$	Function simplifying notation, Eq. (2.13e)
$F$	$L^\lambda$	Constant simplifying notation, Eq. (2.13e)
$F_R(\mathbf{x}_{p,R})$	-	Objective function
$G$	-	Constant simplifying notation, Eq. (2.16c)
$g_0, g_1$	-	Fitting parameter, Eq. (2.19a)
$H$	L	Sample height
$h$	L	Matric potential
$h_a$	L	Matric potential at which the soil reaches the maximum adsorbed water content
$h_{ae}$	L	Air entry value of the soil
$h_c$	L	Fitting parameter
$h_d$	L	Pressure head at oven dryness
$h_i$	L	Matric potential at the inflection point
$h_j$	L	Pressure head at junction point
$h_m$	-	Fitting parameter representing the matric potential at median pore size
$h_s$	L	Minimum capillary height
$I$	-	Constant simplifying notation, Eq. (2.16c)
$J$	$L^{-\lambda-k}$	Function simplifying notation, Eq. (2.16c)
$j$	-	Counter
$K$	$L T^{-1}$	Unsaturated hydraulic conductivity
$K_s$	$L T^{-1}$	Saturated hydraulic conductivity
$L$	-	Constant simplifying notation, Eq. (2.18c)
$M_1$	-	Constant simplifying notation, Eq. (2.18c)
$M_2$	-	Constant simplifying notation, Eq. (2.18g)
$m$	-	Shape parameter of $\theta(h)$
$n$	-	Shape parameter of $\theta(h)$
$P(h)$	-	Function simplifying notation, Eq. (2.18c)
$R$	-	Iteration step
$R_{MAX}$	-	Maximum number of iteration
$S$	-	Variable running from 0 to $S_e$
$S^{ad}$	-	Adsorbed water, Eq. (2.20)

---

$S^{cap}$	-	Capillary water, Eq. (2.20)
$S_e$	-	Degree of saturation
$T$	-	Indicates that the vector is transposed
$w$	-	Weighting factor ranging between 0 and 1, Eq. (2.20)
$w_{\theta,R}$	-	Weight factor vector
$w_{R,i}$	-	Individual weighting factor in $w_{\theta,R}$
$x$	Varies	Integration variable
$\mathbf{x}$	Varies	Parameter vector
$\mathbf{x}_f$	Varies	Vector of non- fitted parameters
$\mathbf{x}_{p,R}$	Varies	Vector of fitted parameters
$Y$	-	Number of complexes
$\alpha$	$L^{-1}$	Shape parameter of $\theta(h)$
$\beta$	-	Constant
$\gamma$	-	Shape parameter of $K(h)$
$\zeta_1$	-	Constant, Eq. (2.14a)
$\zeta_2$	-	Constant, Eq. (2.15a)
$\eta$	-	Fitting parameter
$\theta$	-	Volumetric water content
$\theta_a$	-	Curve fitting parameter representing the volumetric water content when $h = -1\text{cm}$
$\theta_i$	-	$i^{\text{th}}$ observation of the volumetric water content
$\theta_j$	-	Volumetric water content at junction point
$\theta_m$	-	Water content at $h_m$
$\theta_r$	-	Residual water content
$\theta_s$	-	Saturated water content
$\kappa$	-	Shape parameter of $K(h)$
$\lambda$	-	Fitting parameter of $\theta(h)$
$\sigma$	-	Fitting parameter that characterizes the width of the pore size distribution
$\sigma_{h,i}$ $\sigma_{\theta,i}$	-	Error standard deviations respectively for the $i^{\text{th}}$ matric potential and the $i^{\text{th}}$ water content
$\sigma_{h,i}^*$ $\sigma_{\theta,i}^*$	-	Scaled values of $\sigma_{h,i}$ $\sigma_{\theta,i}$
$\sigma_{i,R}^*$	-	Scaled standard deviation of $(h_i, \theta_i)$ during iteration $R$
$\tau$	-	Shape parameter of $K(h)$

---

## Appendix B. Simulations of coupled water and vapor flow in sand columns: fitted parameters and selected flux density profiles in Chapter 3

Table B.1: The fitted parameters with their units and physical range for FSB, RNA, VGA, VGN and BCO (see Table 3.1 for an explanation of the acronyms). The parameters are given in Table A.1 and their equations' numbers are mentioned in Chapter 3 section 3.3.2.

Parameterization	Fitted parameter	Unit	Range	Fitted values
FSB	$\theta_s$	-	$\theta_a - 1$	0.383
	$\theta_a$	-	$0 - \theta_s$	0.028
	$h_{ae}$	cm	$h_d - 0$	-5.075
	$\lambda$	-	$0 - \infty$	1.408
RNA	$\theta_s$	-	$0 - 1$	0.382
	$h_{ae}$	cm	$h_j - 0$	-1.564
	$h_j$	cm	$h_d - h_{ae}$	-1.063E+06
VGA	$\theta_r$	-	$0 - \theta_s$	0.0139
	$\theta_s$	-	$\theta_r - 1$	0.380
	$\alpha$	cm <sup>-1</sup>	$0 - \infty$	0.179
	$n$	-	$1 - \infty$	2.181
	$h_{ae}$	cm	$-\infty - 0$	-0.864
VGN	$\theta_r$	-	$0 - \theta_s$	0.0139
	$\theta_s$	-	$\theta_r - 1$	0.382
	$\alpha$	cm <sup>-1</sup>	$0 - \infty$	0.176
	$n$	-	$1 - \infty$	2.189
BCO	$\theta_r$	-	$0 - \theta_s$	0.0131
	$\theta_s$	-	$\theta_r - 1$	0.383
	$h_{ae}$	cm	$-\infty - 0$	-3.160
	$\lambda$	-	$0 - \infty$	0.967

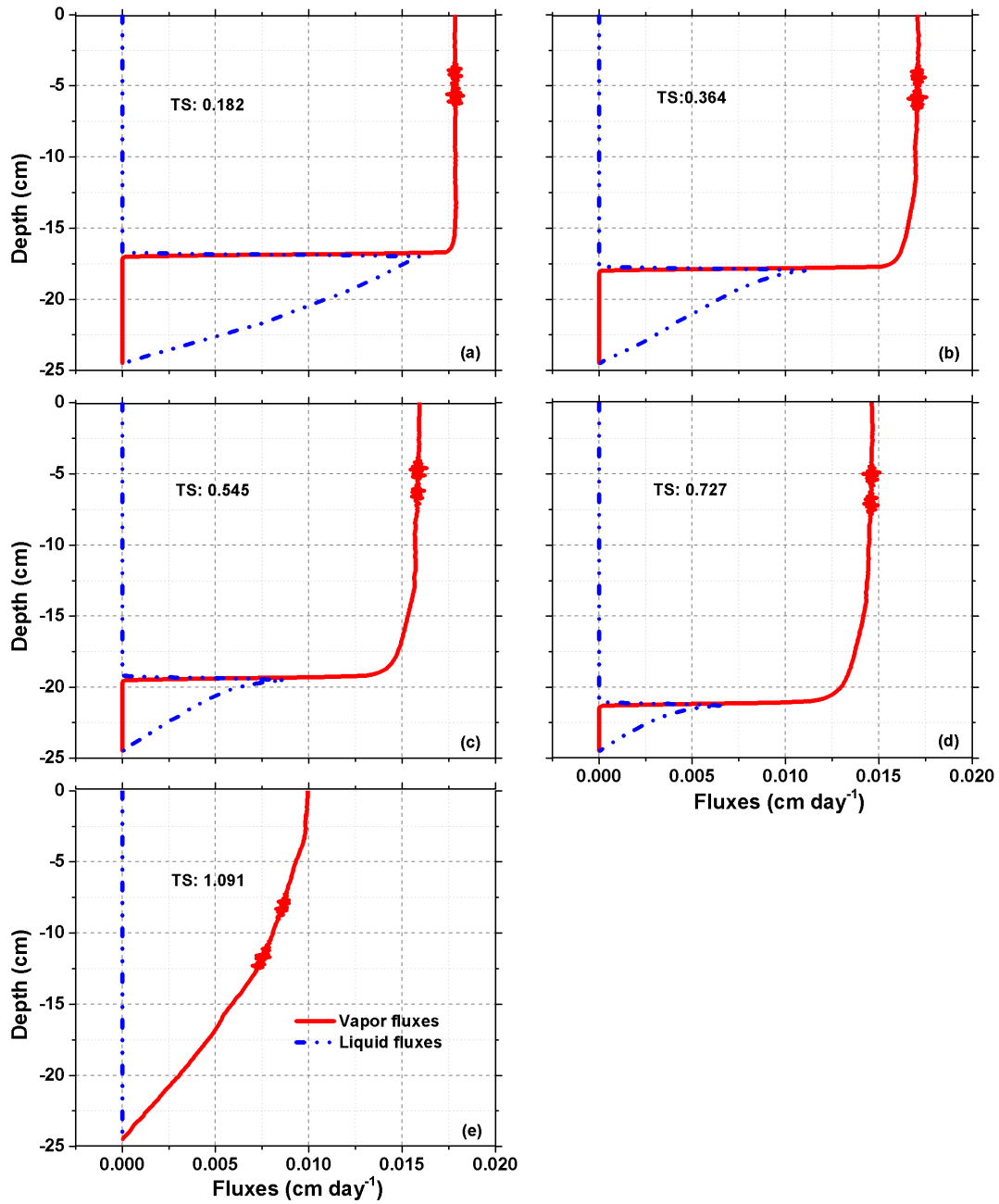


Figure B.1: Water vapor and liquid water fluxes along the column depth for an initial water content of 0.00 using the FSB parameterization at the indicated dimensionless times (TS) scaled by the time the liquid water flux became zero throughout the column.

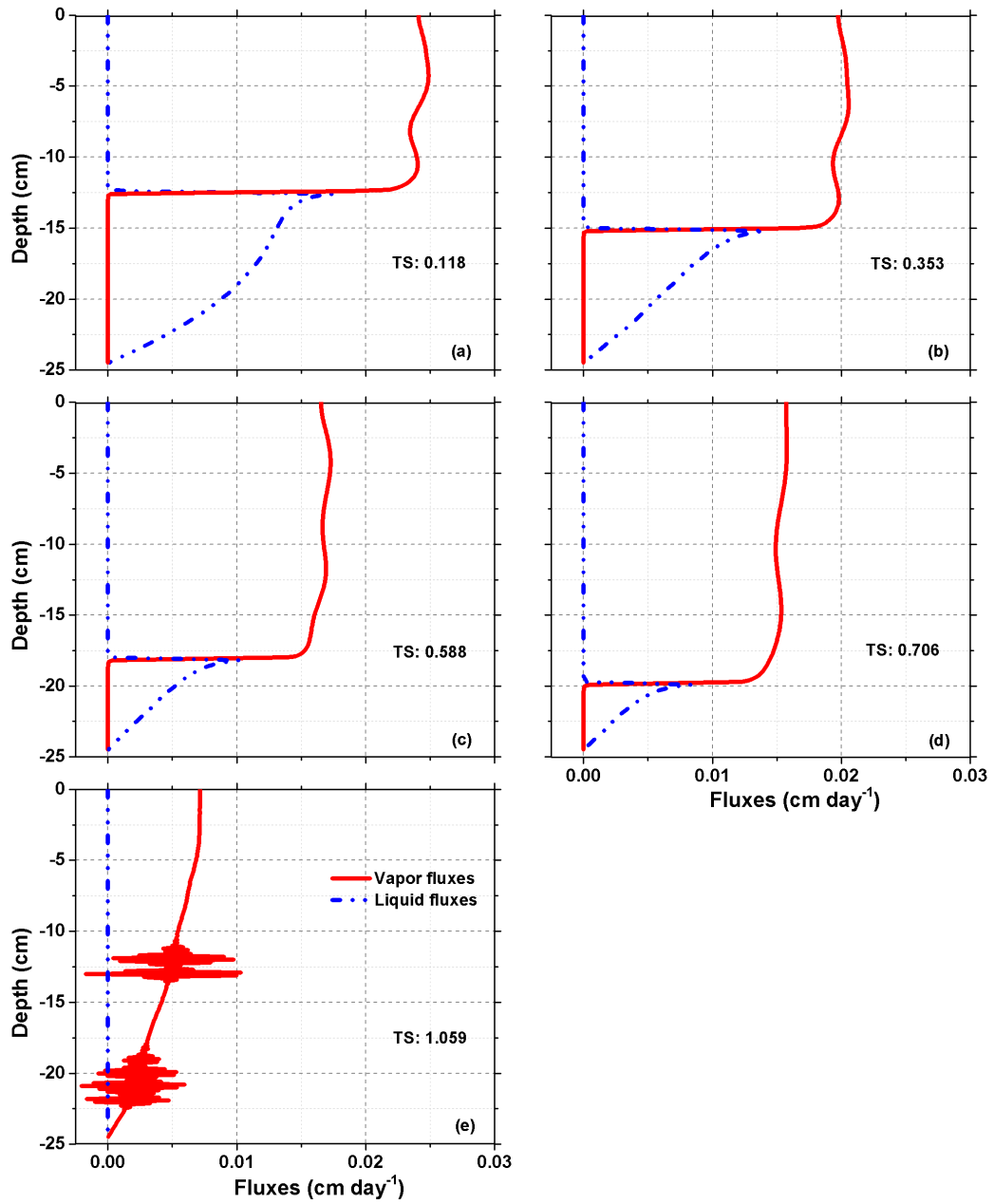


Figure B.2: As Figure B.1, for an initial water content of 0.02.

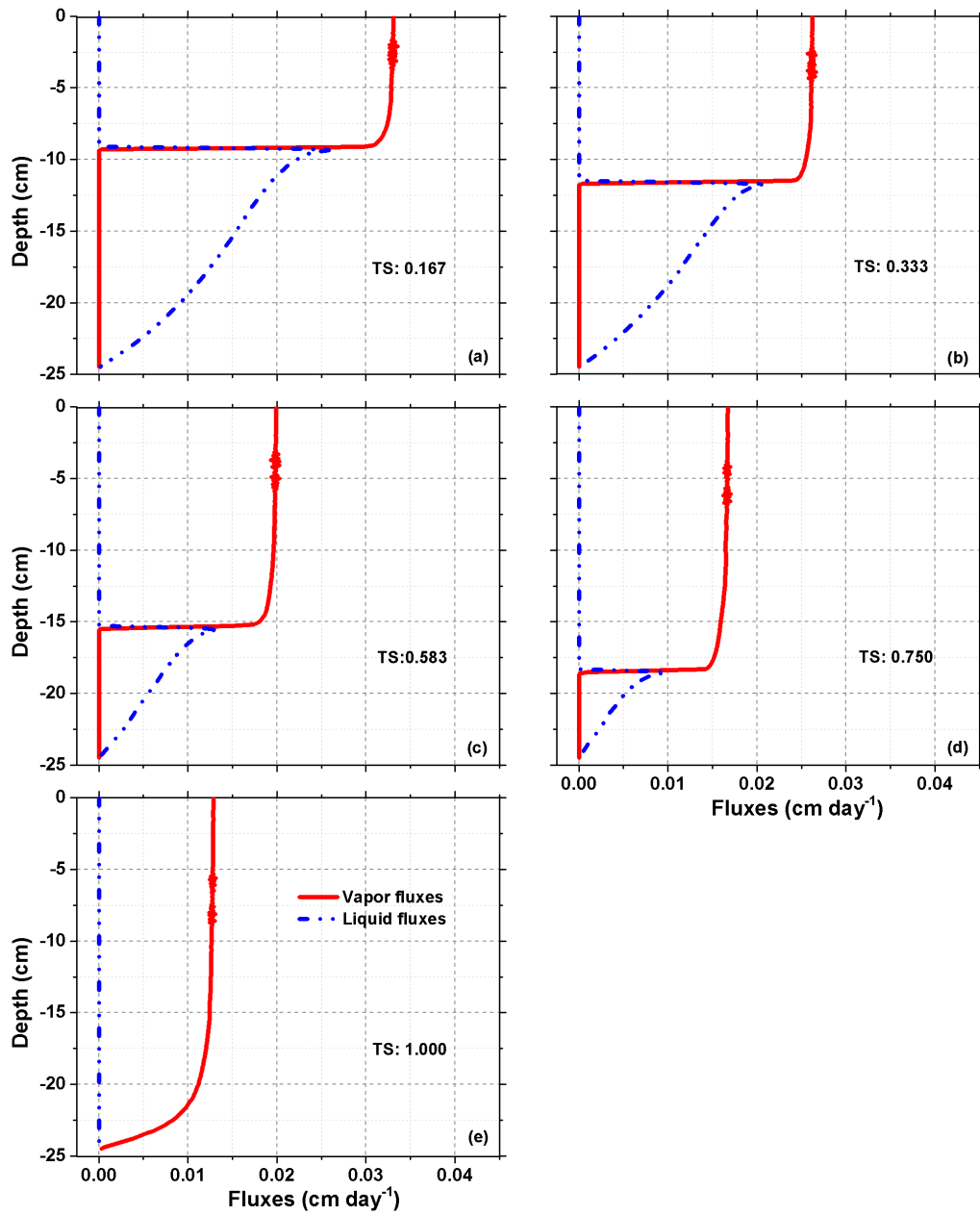


Figure B.3: As Figure B.1, for an initial water content of 0.05.



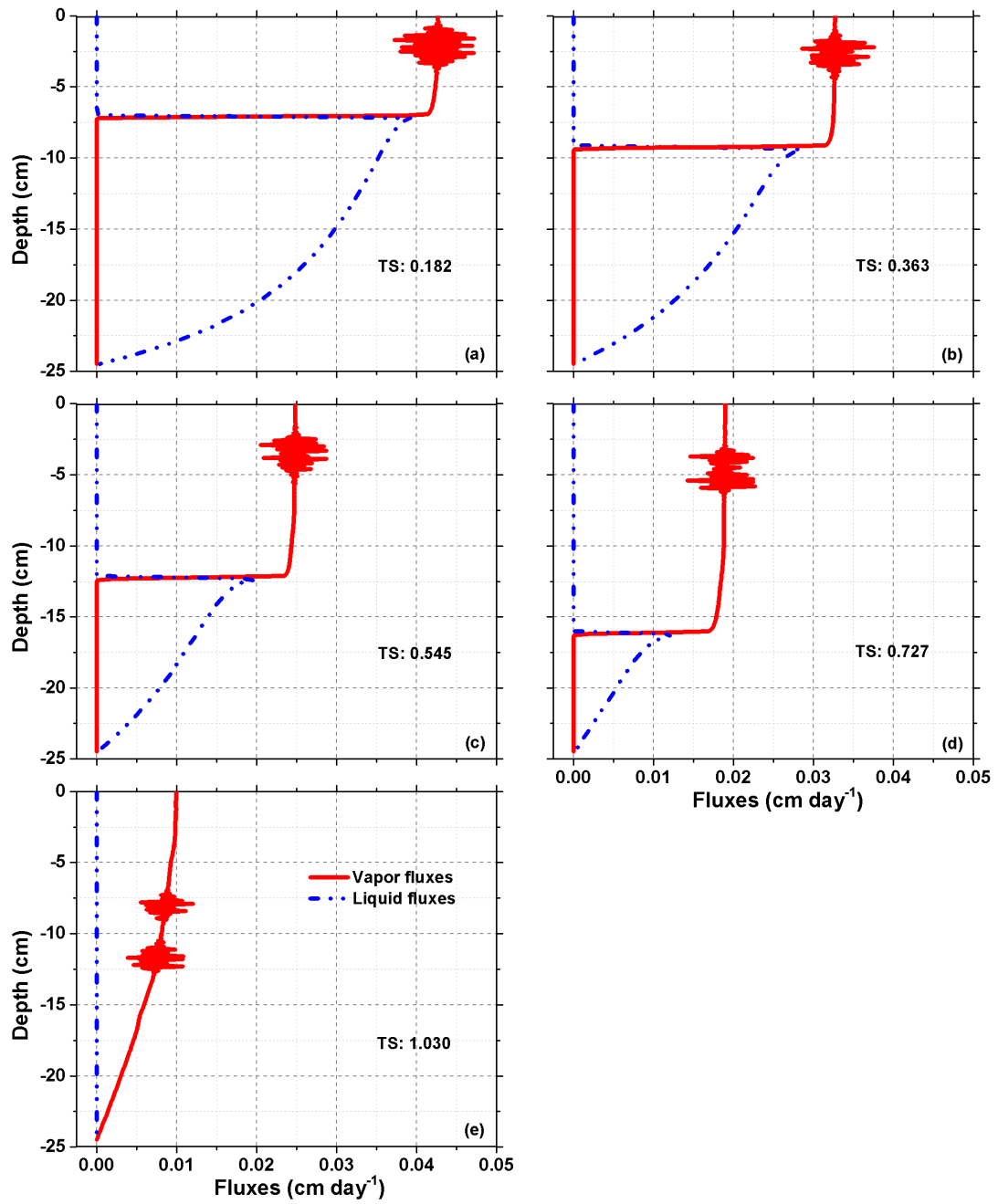


Figure B.4: As Figure B.1, for an initial water content of 0.08.

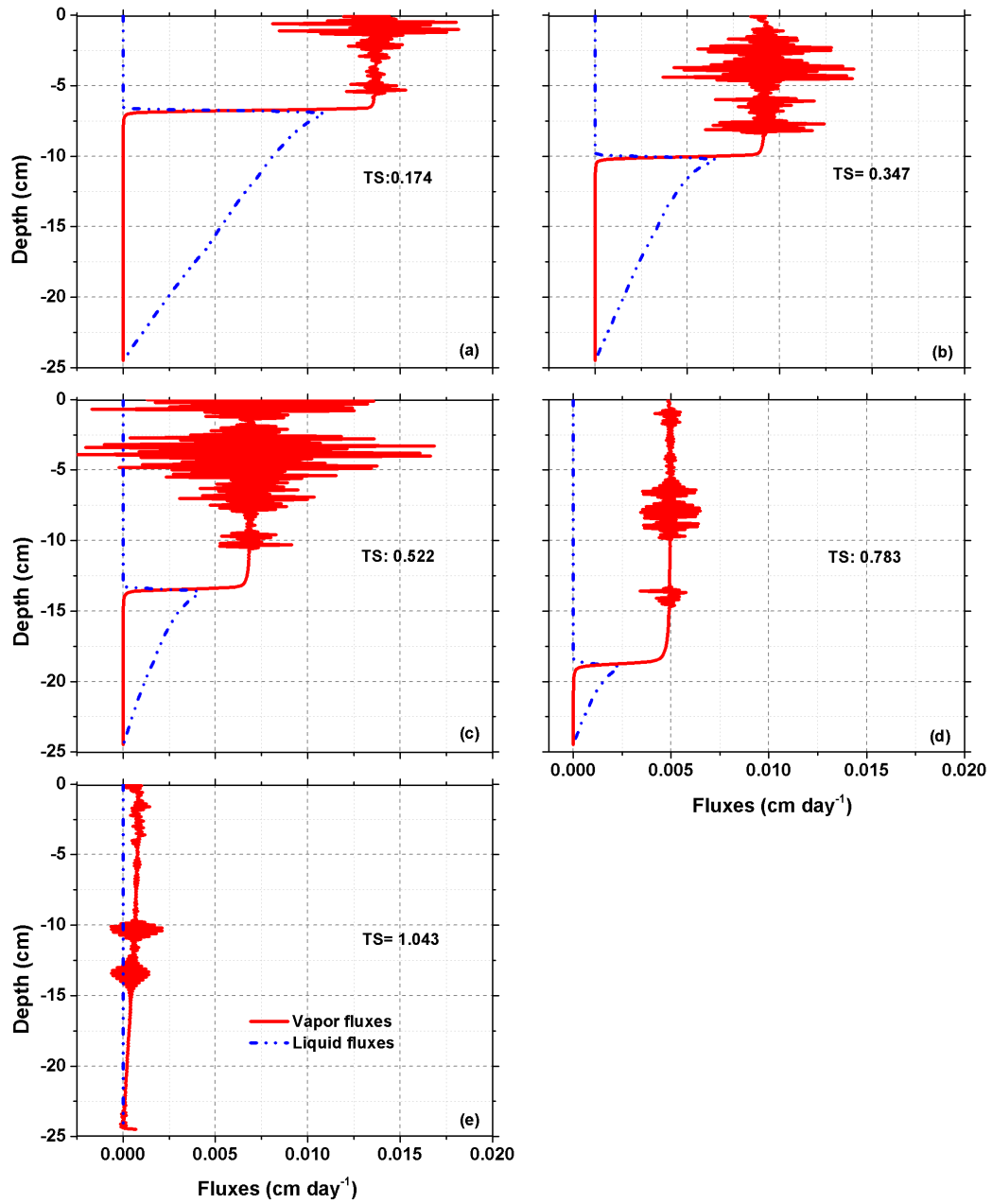


Figure B.5: Water vapor and liquid water fluxes along the column depth for an initial water content of 0.00 using the RNA parameterization at the indicated dimensionless times (TS) scaled by the time the liquid water flux became zero throughout the column.

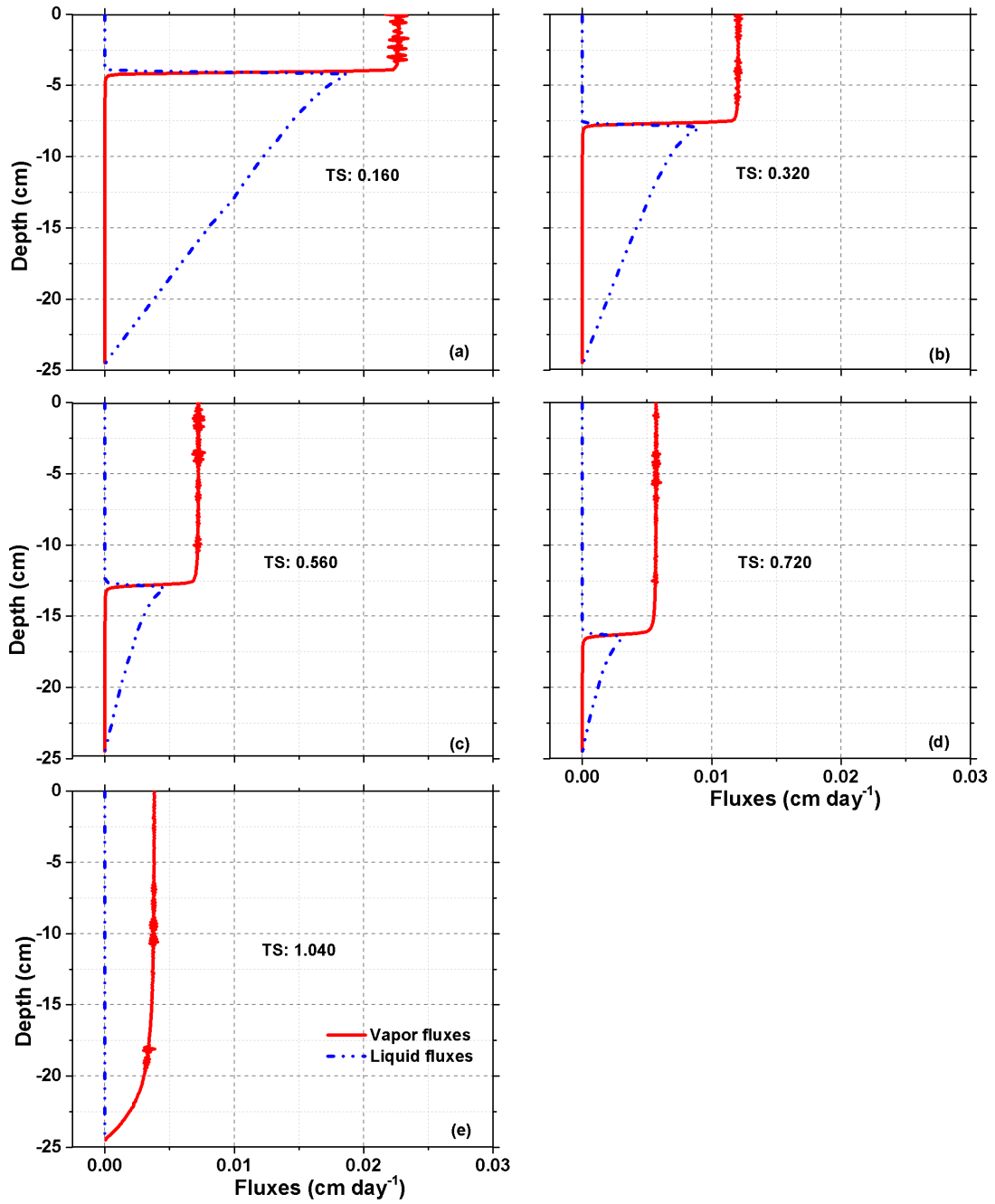


Figure B.6: As Figure B.5 for an initial water content of 0.02.

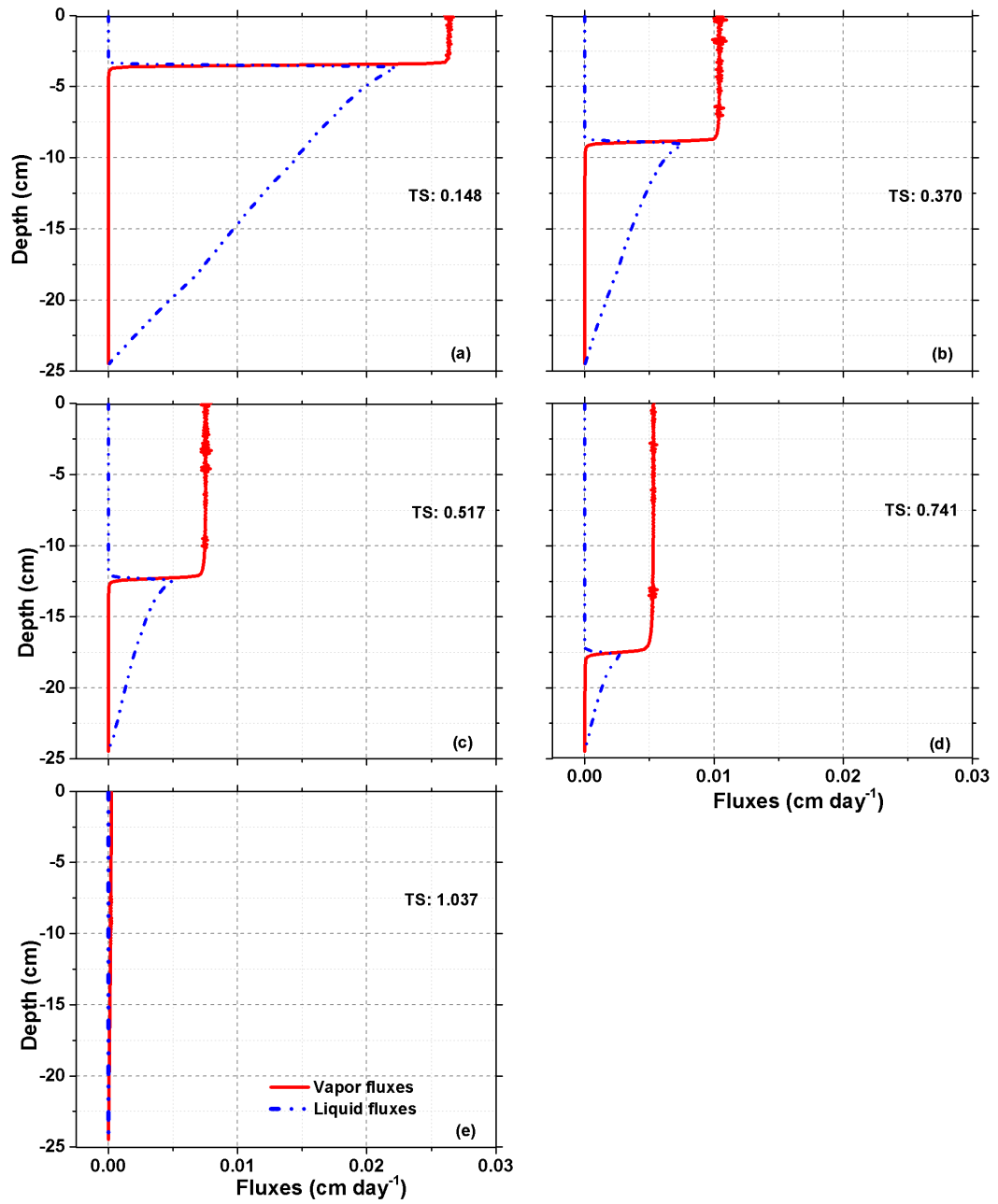


Figure B.7: As Figure B.5 for an initial water content of 0.05.

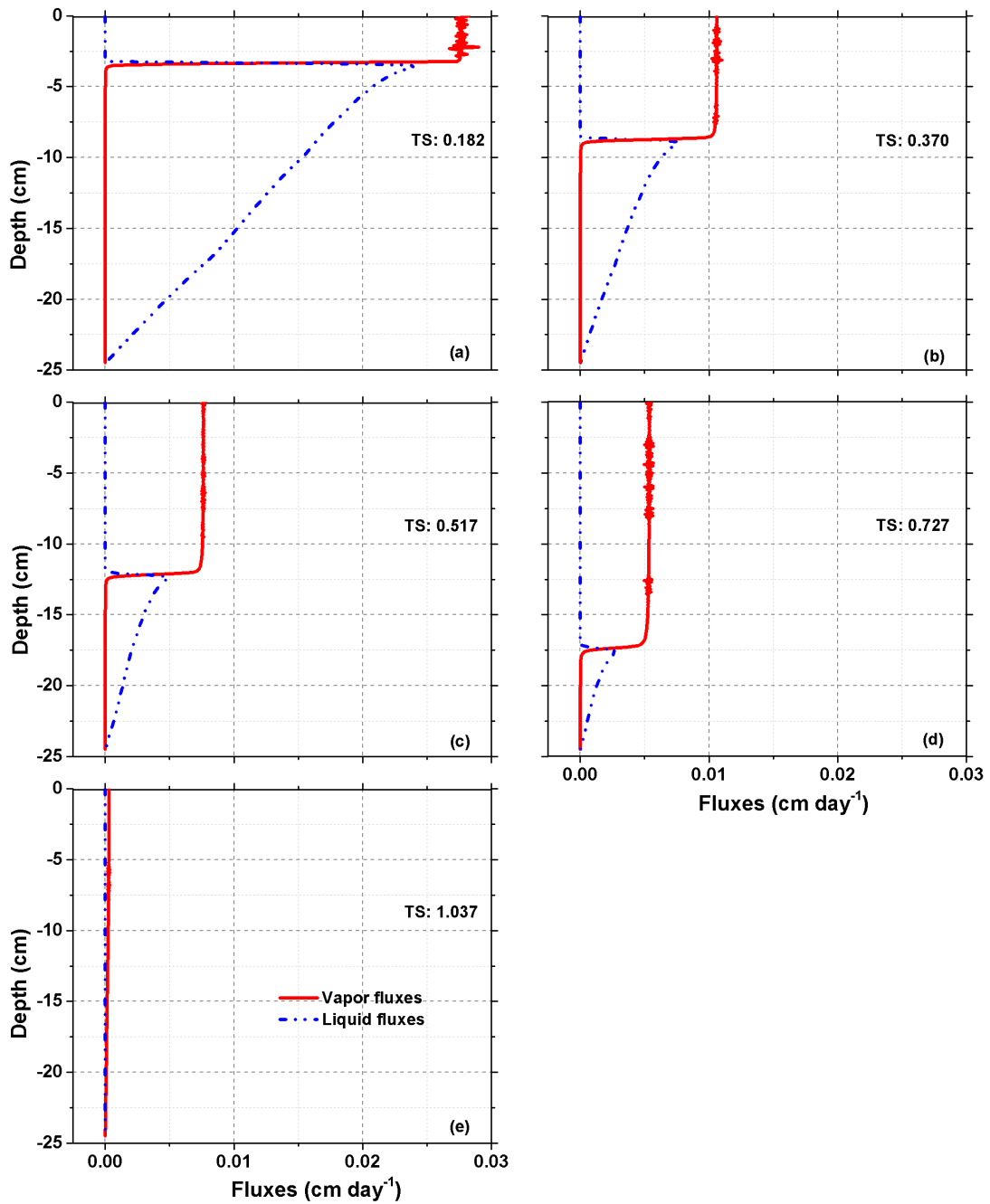


Figure B.8. As Figure B.5 for an initial water content of 0.08.

## Appendix C. Profiles at selected times of various variables generated during long-term simulations Chapter 4.

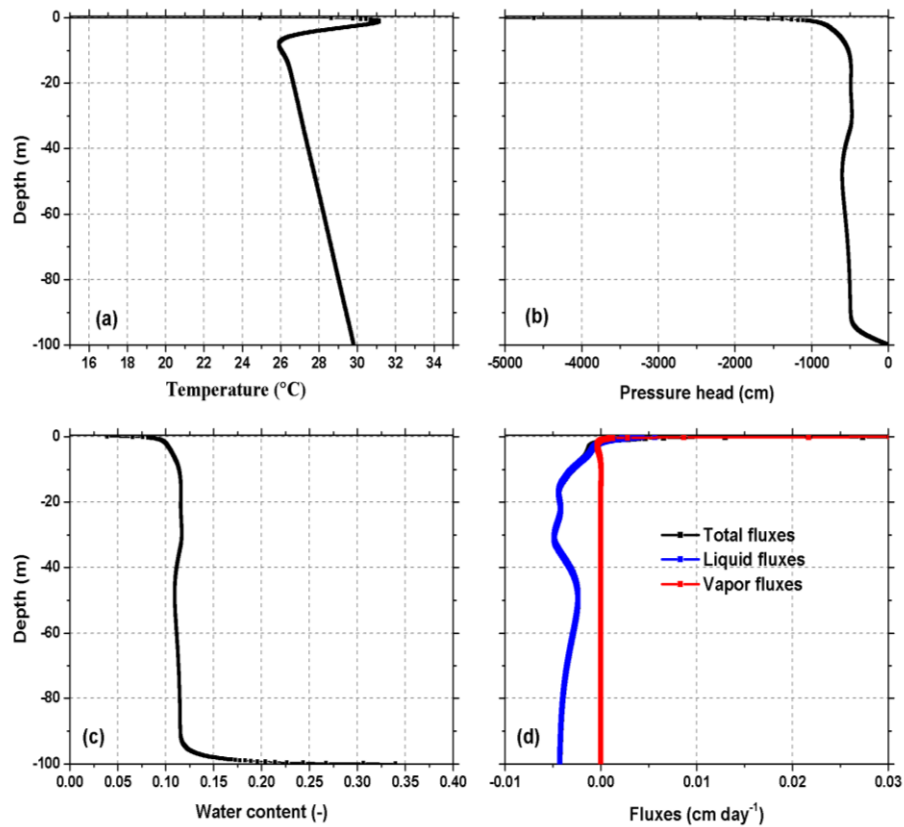


Figure C.1: Profiles of key variables at midnight at the end of the 50<sup>th</sup> hydrological year for FSB under the wetter scenario (Figure 4.3).

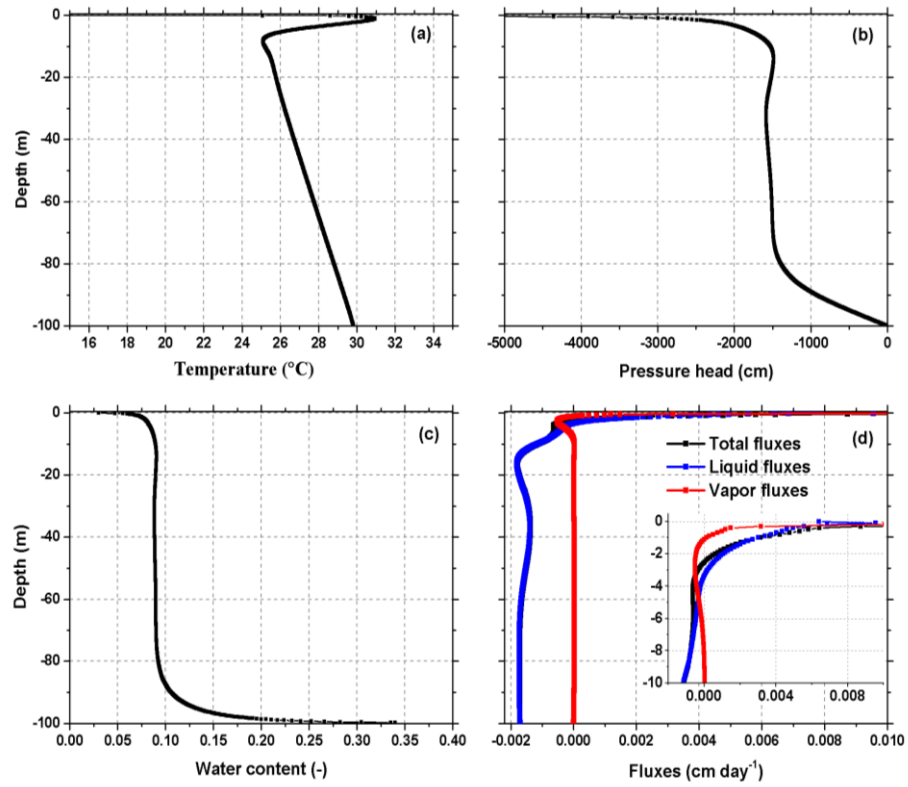


Figure C.2: As Figure C.1, for RIA under the wetter scenario (Figure 4.4).

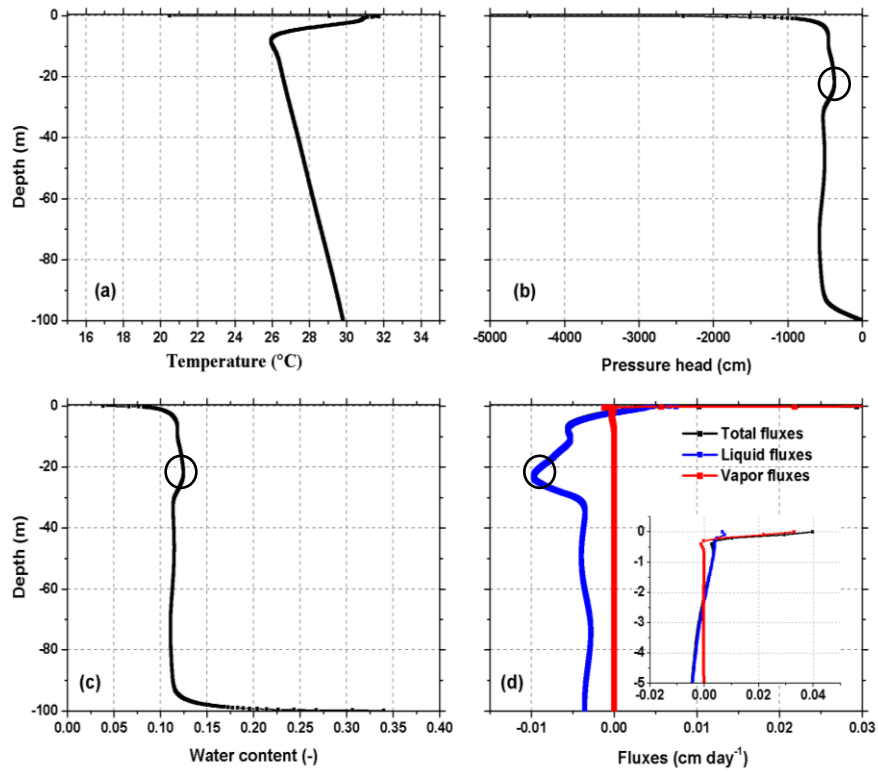


Figure C.3: Profiles of key variables at midnight at the end of the 70<sup>th</sup> hydrological year for FSB under the wetter scenario (Figure 4.3). The black circles point to the dynamics of fluxes and the related soil properties at about 20 m depth, which are discussed in the main text



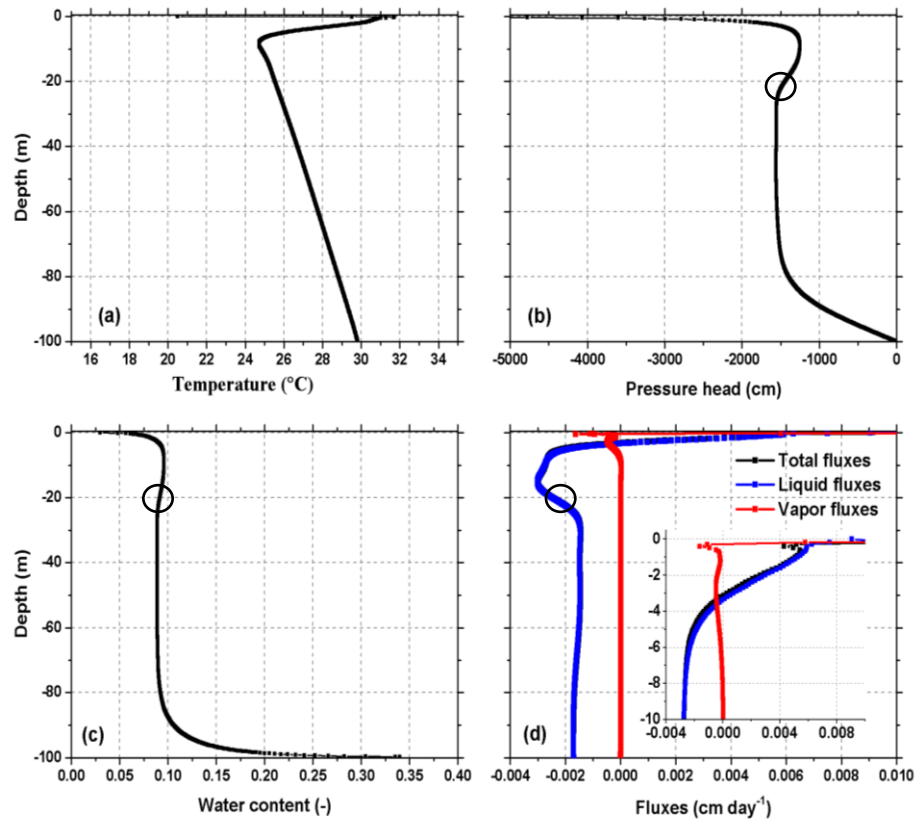


Figure C.4: As Figure C.3, for RIA under the wetter scenario (Figure 4.4)

# Curriculum Vitae

## ▪ Personal Information

**Date and place of birth:** 09.11.1985 / Latakia, Syria  
**Marital status:** married, 2 children  
**Nationality:** Syrian  
**Address:** Gerberstr. 18/821 04105 Leipzig  
**Mobile phone:** 004917683386910  
**Email:** madiraneem@yahoo.com

## ▪ Work Experience

- 02/2017 – 09/2017      **Scientific Assistant (Guest)**  
*Helmholtz center for environmental research (UFZ) Halle, Institute of Soil System Science*
- Project water scarcity: Groundwater recharge in semiarid regions
- 04/2013 – 01/2017      **Scientific Assistant**  
*Helmholtz center for environmental research (UFZ) Halle, Institute of Soil System Science*
- Project water scarcity: Groundwater recharge in semiarid regions
  - supervisor Dr. Gerrit de Rooij
- 08/2009 – 03/2010      **Scientific Assistant**  
*Tischrin University-Latakia, Syria*
- Faculty of civil engineering
  - Teaching: Hydrology and Mechanics of fluids
- 10/2008 – 07/2009      **Teaching Assistant**  
*Tischrin University-Latakia, Syria*
- Faculty of Civil Engineering
  - Hydrogeology, Hydrology and Mechanics of fluids

## ▪ Education

- 06/2013 –      **PHD**  
*Martin-Luther-University Halle-Wittenberg, Institute of Geosciences*
- Topic:  
Engineering studies of the water movement in the unsaturated zones
  - Supervisors: Prof. Dr. Ralf Merz, Martin-Luther-University- Halle (Saale),  
Dr. Gerrit de Rooij, UFZ Halle

- 10/2010 – 02/2013      Master study: Hydro Science & Engineering  
*Technical University of Dresden*
- Master thesis:  
 Scenario based simulation of infiltration at a test site in Ad-Dahna-desert in Saudi-Arabia (grade:1,7)
  - Advanced knowledge:
  - **Degree: Master of Science Hydro Science & Engineering** (grade 1,7)

- 10/2003 – 08/2008      Study: Civil Engineering „Irrigation and Drainage“  
*Tischrin University Latakia, Syria*
- Bachelor thesis:  
 Design of buried drainage system (lab and field work were included)
  - Grade: 83.70%; The best student from 2004 to 2008
  - Degree: Bachelor of Civil Engineering

▪ **School study**

- 09/2000 – 08/2003      Secondary school Latakia, Syria; grade: 94% (226/240)

▪ **Scholarships**

- 04/2010 – 02/2013      National scholarship from Tischrin University Latakia, Syria for the Master study at the Technical University of Dresden

- 05/2017-10/2017      Graduation scholarship for foreign young female scientists at the Martin-Luther-University Halle-Wittenberg

▪ **Languages**

English    Fluent  
 German    Very good, C1  
 Arabic    Native speaker

▪ **Computer skills**

Microsoft Office and very good general knowledge  
 AutoCAD, SWAT (Soil Water Assessment Tool), HYDRUS, GIS, ORIGIN

## ■ Conferences

- European Geosciences Union (EGU) Conference in Vienna/Austria
  - 2015:** Participation with poster, topic “Numerical and Experimental Quantification of coupled water and water vapor fluxes in very dry soils”
  - 2016:** Participation with poster, topic “A critical evaluation of soil water retention parameterization with respect to their behavior near saturation and in the dry range”
  - 2017:** Participation with poster, topic “Water, heat and vapor flow in a deep vadose zone under arid and hyper-arid conditions: a numerical study”
- HIGRADE conference **2015** at UFZ, Leipzig: Participation with poster, topic “Simulation study of coupled water, water vapor and heat fluxes in very dry sandy soil”
- American Geophysical Union (AGU) conference **2016** in Austin/USA: Participation with poster, topic “A critical evaluation of soil water retention parameterization with respect to their behavior near saturation and in the dry range”

## ■ Courses & Workshops

03/2016	Concept, Design and Presentation of Scientific Posters - UFZ Leipzig
12/2015	Good scientific practice - UFZ Leipzig
09/2015	Hydrological and Hydrogeological Field Methods in TERENO - Harz (Meisdorf) and UFZ Leipzig
08/2015	Introduction to GIS - UFZ Halle
07/2015	Summer School on Flow and Transport in Terrestrial Systems - UFZ Halle
07/2015	Academic presenting in English - UFZ Leipzig
05/2015 – 06/2015	Scientific writing - UFZ Halle
03/2015	HYDRUS Workshop: Advanced modeling of water flow and contaminant transport in porous media using the HYDRUS and HPI software packages - Prague (Czech Republic)
03/2015	Image Processing - UFZ Halle
02/2015	Fluid flow and reactive transport in natural porous media - Jena

## **Eidesstattliche Erklärung / Declaration under Oath**

Ich erkläre an Eides statt, dass ich die Arbeit selbstständig und ohne fremde Hilfe verfasst, keine anderen als die von mir angegebenen Quellen und Hilfsmittel und die den benutzten Werken wörtlich oder inhaltlich entnommen Stellen als solche kenntlich gemacht habe.

I declare under penalty of perjury that this thesis is my own work entirely and has been written without any help from other people. I used only the sources mentioned and included all the citations correctly both in word or content.

.....  
Datum / Date

.....  
Unterschrift / Signature